Mathematical Modeling of Lithium-ion Intercalation Particles and Their Electrochemical Dynamics

by

Yi Zeng

B.S., University of Illinois at Urbana-Champaign (2011)

Submitted to the Department of Mathematics
in partial fulfillment of the requirements for the degree of

Doctor of Philosophy in Applied Mathematics

at the

MASSACHUSETTS INSTITUTE OF TECHNOLOGY

June 2015

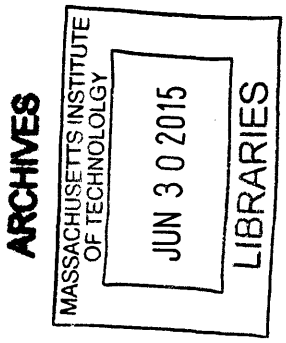

Author ..... Signature redacted .....
Department of Mathematics
April 28, 2015

Certified by... Signature redacted .....
Martin Z. Bazant
Professor of Chemical Engineering and Mathematics
Thesis Supervisor

Accepted by ..... Signature redacted ....
Michel Goemans
Chairman, Department Committee on Graduate Theses

Mathematical Modeling of Lithium-ion Intercalation Particles and Their Electrochemical Dynamics

by

Yi Zeng

Submitted to the Department of Mathematics
on April 28, 2015, in partial fulfillment of the
requirements for the degree of
Doctor of Philosophy in Applied Mathematics

Abstract

Lithium-ion battery is a family of rechargeable batteries with increasing importance that is closely related to everyone's daily life. However, despite its enormously wide applications in numerous areas, the mechanism of lithium-ion transport within the battery is still unclear, especially for phase separable battery materials, such as lithium iron phosphate and graphite. Mathematical modeling of the battery dynamics during charging/discharging will be helpful to better understand its mechanism, and may lead to future improvement in the battery technology.

In this thesis, a new theoretical framework, the Cahn-Hilliard reaction (CHR) model, is applied to model the bulk phase separation dynamics of the single intercalated particle in the lithium-ion battery. After a study of the efficient numerical algorithm for solving nonlinear diffusion equations, we numerically investigate the thermodynamics and electrokinetics of the 1D spherical CHR model with different possible material properties in detail. We also extend the CHR model to 2D and briefly study the effects of the surface electron-conducting coating layer.

We also work on the Marcus theory, which is demonstrated to be a better theoretical framework for heterogeneous electron transfer at the surface of intercalated particles in the batteries. We provide simple closed-form approximations to both the symmetric Marcus-Hush-Chidsey (MHC) and the asymmetric-Marcus-Hush (AMH) models by asymptotic technique. By avoiding the numerical evaluations of the improper integral in the old formulae, computing the surface reaction rate with the new approximation is now more than 1000 times faster than before.

Thesis Supervisor: Martin Z. Bazant
Title: Professor of Chemical Engineering and Mathematics

Acknowledgments

First of all, I would like to express the most sincere appreciation to my thesis advisor, Prof. Martin Z. Bazant, for all of his guidance, patience, inspiration and encouragement throughout my PhD years. He provided me a great opportunity to freely pursue any research project I am interested in, and his continued support and advise led me to the right way. His enthusiasm and dedication to research also made a tremendous impact on me.

I am also very grateful to Dr. Peng Bai, for his helps in understanding the electrochemical systems and studying the literature, as well as our countless discussions and many collaborations on projects. The same thanks will go to Raymond Smith for all discussions, collaborations and helps in writing, and Elisha Rejovitzky for discussions on the elastic strain and 2D simulations of intercalated particles. I would also like to acknowledge the support of my colleagues and friends in the Bazant groups.

I would like to extend my deepest appreciation to Prof. Lee DeVille, my undergraduate thesis advisor. Our collaboration on the neural network paper starting from 2009 guided me into the magical world of mathematical research for the first time. It is always an enjoyable time to work on this project. I would also like to acknowledge Dr. Paul Albertus and Dr. Jake Christensen for the collaboration on the numerical PDE algorithm project, which serves as the starting point and the foundation of my thesis; Dr. Penghao Xiao and Prof. Graeme Henkelman for the collaboration on the minimum mode optimization project. These results will not be possible without their kindly helps.

I would like to thank all my friends in MIT, especially to Wenzhe Wei, Hongkai Zhang, Ruixun Zhang, Xuwen Zhu and Zeyuan Allen-Zhu. We grumbled and laughed together through the past four years, they made my experience in MIT really a pleasant and unforgettable one.

Special thanks to National Science Foundation for financial supports. The NSF Graduate Research Fellowship enables me to focus on my research during my four-year scientific journey towards PhD.

Finally, my deepest gratitude goes to my parents, Xiaoyun and Zhi, for their endless supports, understandings and loves. They are always my source of courage and happiness. I am sure they will enjoy my work in this thesis, although they may never really understand it. So I would like to dedicate this work to my loving parents, without whom this work would not have been possible.

This doctoral thesis has been examined by a Committee of the Department of Mathematics as follows:

Professor Martin Z. Bazant .....
Thesis Supervisor
Chairman, Thesis Committee
Professor of Chemical Engineering and Mathematics

Professor Hung Cheng .....
Member, Thesis Committeer
Professor of Mathematics

Professor Steven G. Johnson .....
Member, Thesis Committee
Professor of Mathematics

Contents

List of Figures

List of Tables

Chapter 1

Introduction

1.1 Background of Lithium-ion Batteries

The revolutionary development of lithium-ion battery technology in recent decades has already made a great impact on everyone's life [7]. As a light and compact rechargeable energy storage device converting electrical energy and electrochemical energy cyclically, the lithium-ion battery now supplies convenient power to numerous cellphones, laptops, wearable electronics, electrical vehicles and many other devices [181]. This "best battery technology anyone has ever seen" is now feeding the power-hungry mobile world [213]. With sales numbers hitting about five billion in 2013, the commercial lithium-ion battery now has doubled the power density (by weight) but also is more than 10 times cheaper than its ancestor in 1991, first introduced to the market by Sony.

With atomic number only 3, lithium is the lightest member (relative atomic mass of 6.94) among all alkali metals, the group with smallest electronegativity on the periodic table. Lithium has a standard electrode potential of about -3.04 V [204]. The relatively high reservation of lithium carbonate also leads to a more-than-sufficient availability and good affordability of this element [182]. All these features distinguish lithium as a potential high-energy-density, high-voltage battery material.

In the 1970s, several researchers discovered that the alkali metals can be inserted into some inorganic compounds reversibly [224]; this made the invention of a new

family of rechargeable batteries possible. With two different intercalation materials sitting in both electrodes separately, the lithium initially is intercalated into one of them. During the charging or the discharging process, lithium is removed from that electrode, A. The lithium-ion with one positive charge can transport internally through the battery to the other electrode, B, while the electron needs to migrate through the outer circuit, which creates the current. Once they reach the electrode B, the lithium-ion and the electron can be seen as recombined to a neutral atom that then inserts into the intercalation material in electrode B. If the intercalation processes at both electrodes are reversible, the total reaction direction can be controlled by adjusting the circuit voltage; thus the battery is rechargeable.

Following the first lithium-ion battery developed by Exxon with TiS_2 as the cathode material [223], many intercalation materials have been discovered. Among them, the olivine-type lithium iron phosphate (Li_xFePO_4, LFP), nowadays a popular cathode material for lithium-ion batteries, is a good example. Due to its outstanding electrochemical properties, this material is already attracting much attention. In spite of some disadvantages in its conductivity and high-current capability initially reported [165], later advances in surface coatings and particle-size controlling processes have improved it to a long-cycle-life, high-rate material, with a relatively low cost and good environmental friendliness [231].

Although the lithium-ion battery is now considered "the most impressive success story in modern electrochemistry in the past two decades," many big challenges have yet to be faced [72]. For example, the cutting-edge commercial lithium-ion battery, which supplies an energy density of about 250 $Whkg^{-1}$, is now the bottleneck for electric vehicle and mobile electronic device developments. More than twice the current lithium-ion battery energy density is required for an electric vehicle to match the 800-kilometer range of a petrol tank [206]. To fulfill the requirement, we need to develop a strategy that can significantly increase the battery energy density, while still maintaining its current affordability, cycle life, and safety. Indeed, how to achieve this goal is also seen as the most essential challenge in electrochemistry and electrochemical engineering [82].

Despite rapid development in battery technology, the growth of knowledge in science underlying battery technology is not keeping pace [204]. Extensive efforts have been put into searching for battery materials [142, 231]. However, the detailed physics in the lithium-ion battery and its associated limiting processes have remained largely unknown.

In many cases, microscopic battery material properties at the atomistic level are available thanks to the *ab initio* calculations, as well as macroscopic experimental measurements such as the current-voltage (IV) plots. Sadly the link between these two scales is mostly missed. Therefore, it is crucial to develop a new model at the continuum length-scale to bridge the information from the microscopic and the macroscopic scales to advance our knowledge about the lithium-ion battery system. Better understanding of this system may help us to systematically optimize the battery design, moving away from the current trial-and-error approach, which could lead to an improvement in battery performance.

Modeling this sophisticated electrochemical system mathematically involves a large, coupled, highly nonlinear partial differential equation system to describe the physics of all components and their interactions. The study of this model raises many challenges and interesting questions for applied mathematicians.

1.2 Previous Work on Battery Modeling

Since 1962, John Newman and his coworkers have been developing a famous theoretical framework named "Porous-Electrode Theory" [157, 156, 155]. Making only a few simple assumptions, including the phenomenological Butler-Volmer charge-transfer reaction at the electrodes, and simple spherical isotropic linear diffusions in active electrode material particles, this elegant theory has achieved great success in modeling battery systems, including the first model of a full lithium-ion battery by Doyle, Fuller and Newman in 1993 [67]. This framework has since been extensively applied to many different battery systems and it has demonstrated good agreement with experimental data.

Unfortunately, in 1997 came the discovery of the lithium iron phosphate by John Goodenough's group [165], raising suspicion about one basic assumption in the porous-electrode theory. In this work, Goodenough's group observed a stable voltage plateau in the current-voltage plot at room temperature [165, 204], which strongly implies the existence of lithium phase separation in lithium iron phosphate particles. This evidence was later supported by other direct experimental observations [58, 232, 59, 5, 164, 46]. These obviously contradict the assumption of linear Fickian lithium diffusion in cathodic particles in Newman's theory.

The "shrinking core" model was later proposed by Srinivasan and Newman to resolve this conflict [191]. To enforce a core-shell structure in the LFP particle, which was originally suggested by Goodenough's group, Srinivasan and Newman set the concentrations of the lithium-rich region and the lithium-poor region to two fixed constants. Then, by mass conservation, the sharp phase boundary location could be easily calculated over time. By replacing the original linear Fickian diffusion with this new shrinking core assumption, the adjusted porous-electrode theory provides the only reasonable fit to the experimental data up to now [191, 52].

However, this solution is still far from the end of the story. In fact, several fundamental concerns are raised by this fitting result. The fitted diffusivity of LFP from the adjusted porous-electrode model is significantly off from the *ab initio* calculation by several orders of magnitude [133]. While the shrinking core model may be a good approximation in micro-sized LFP particles with high defect rates, experimental results indicate that the phase separation dynamics are more complicated than the simple core-shell structure enforced in the shrinking-core model [121, 38, 5, 59, 46, 158].

A more accurate and consistent approach to modeling electrochemical kinetics with phase separation is based on non-equilibrium thermodynamics [15]. For reaction-limited anisotropic ion-intercalated nanoparticles, the general theory can be reduced to the Allen-Cahn reaction (ACR) equation for the depth-averaged ion concentration [188, 8], which has been applied successfully to predict experimental data, using generalized Butler-Volmer kinetics and accounting for the coherency strain [48, 47, 15] together with the surface wetting condition [47]. An important prediction of the ACR

model is the dynamical suppression of phase separation [8, 48]. For large micron-sized particles, solid diffusion limitation leads to a different limit of the general theory, the Cahn-Hilliard reaction (CHR) model for bulk phase separation with heterogenous surface reactions [188, 31, 15, 99].

In addition to the linear Fickian diffusion assumption, the validity of the phenomenological Butler-Volmer(BV) kinetics on electrode surfaces in Newman's porous-electrode theory is also in question. Recent experiments report that the physics-based Marcus-Hush-Chidsey kinetics can perfectly explain the Tafel plots for any rate, whereas Butler-Volmer prediction is valid only for low rates [9]. This indicates the potential benefit of a paradigm shift in the porous-electrode type modeling of kinetics in electrochemical systems away from the currently popular Butler-Volmer scheme. A more detailed introduction to the Marcus charge transfer theory is provided in the following section.

1.3 Marcus Theory

Marcus theory is now a well-established transition state model of electron transfer, named to honor Rudolph A. Marcus, who first developed this new theoretical framework. His novel paper, first published in 1956 [136], explained the reaction rates of electron transfer reactions in a homogeneous solution with "very little spatial overlap of the electronic orbitals of the two reacting molecules in the activated complex" and negligible structure change; this type of reactions is now also called the outer sphere electron transfer reactions.

As electron transfer is the key component of any breaking or formation of chemical bonds, after some successful fittings to experimental data [139, 140], the Marcus theory has attracted great attention in chemical research. The original version of this electron transfer theory (in homogeneous solutions), was soon generalized to heterogeneous electron transfer reactions at electrodes [135, 137, 95]. Later, it was also discovered that, after some modifications, the Marcus framework could accurately predict Faradaic reaction kinetics for liquid electrolytes [42, 147, 95].

Very recently, the Marcus theory has also been found to be applicable to model the Faradaic reaction kinetics for solid electrolytes as well [15, 9]. This is the first and only physics-based model for electron transfer kinetics at the electrode in battery systems. Although the Marcus theory is rarely used and remains largely unknown in electrochemical engineering, it is now a potential practical alternative to the ubiquitous Butler-Volmer equation, a phenomenological model, for improving the understanding and engineering of electrochemical systems.

Several reviews and books have been published to summarize in detail the development history [137], theoretical foundations [134, 12, 23, 117, 13], and chemical and biological applications [195, 138, 83, 12] of the Marcus theory. The Marcus theory is now the standard theoretical framework for studying electron transfer reactions. Due to the great success of this theory, Rudolph A. Marcus was honored with the1992 Nobel Prize in chemistry "for his contributions to the theory of electron transfer reactions in chemical systems" [137].

1.4 Thesis Outline

In this thesis, the main focus is to address some essential mathematical problems related to modeling the ion-intercalation dynamics, especially the lithium-ion charging/discharging systems. In addition, a study in the minimum mode optimization for the transition states finding in the energy landscape is conducted, and a project in modeling a multi-population stochastic neural network dynamics is presented (both in the appendix).

Chapter 1 initiates a general background overview of lithium-ion batteries and introduces the state-of-the-art of lithium-ion battery modeling. This chapter also presents an outline of the major theme in each chapter.

Chapter 2 introduces a new numerical method that efficiently solves the one-dimensional nonlinear spherical diffusion equations, which are the most computationally intensive part within the traditional pseudo-2D framework for battery modeling. This chapter focuses on a comparison of the formulation, accuracy, and order of

the accuracy for two numerical methods of solving the spherical diffusion problem with a constant or non-constant diffusion coefficient: the finite volume method and the control volume method. Both methods provide perfect mass conservation and second-order accuracy in mesh spacing, but the control volume method provides the surface concentration directly, has a higher accuracy for a given number of mesh points, and can also be easily extended to variable mesh spacing. Variable mesh spacing can significantly reduce the number of points that are required to achieve a given degree of accuracy in the surface concentration (which is typically coupled to the other battery equations) by locating more points where the concentration gradients are highest [239].

Chapter 3 studies the single-particle charging dynamics under the Cahn-Hilliard reaction theory framework, which predicts transitions from solid-solution radial diffusion to two-phase shrinking-core dynamics. This general approach extends previous lithium-ion battery models, which either neglect phase separation or postulate a spherical shrinking-core phase boundary, by predicting phase separation only under appropriate circumstances. The effect of the applied current is captured by generalized Butler-Volmer kinetics, formulated in terms of diffusional chemical potentials, and the model consistently links the evolving concentration profile to the battery voltage. We examine sources of charge/discharge asymmetry, such as asymmetric charge transfer and surface "wetting" by ions within the solid, which can lead to three distinct phase regions. In order to solve the fourth-order nonlinear CHR initial-boundary-value problem, a control-volume discretization is developed in spherical coordinates based on the results in Chapter 2. The basic physics are illustrated by simulating many representative cases, including a simple model of the popular cathode material, lithium iron phosphate (neglecting crystal anisotropy and coherency strain). Analytical approximations are also derived for the voltage plateau as a function of the applied current [237].

Chapter 4 works on a two-dimensional Cahn-Hilliard reaction ion-intercalation particle model coupled with a surface electron-conducting coating layer. Although surface coating has been demonstrated to be a critical technique for performance

improvement, of both the single charge cycle performance and the long-term life capacity, the previous modeling of ion-intercalated batteries has not quantified this effect. This chapter introduces a new possible source of transport limitation in the high-rate battery operation, by linking the coating charge conductivity to other bulk properties. This may help to explain the capacity lost in the battery system in high-rate operation and large disagreement among fitting material properties in the battery materials. A previous common assumption of the "depth-average approximation" in the CHR battery particle modeling is also examined in this chapter.

Chapter 5 looks at a more general electron transfer theory, the Marcus-Hush-Chidsey (MHC) model, at metal electrodes. This model is well known in electroanalytical chemistry as a successful microscopic theory of outer-sphere electron transfer at metal electrodes, but it is unfamiliar and rarely used in electrochemical engineering. One reason may be the difficulty of evaluating the MHC reaction rate, which is defined as an improper integral of the Marcus rate over the Fermi distribution of electron energies. This chapter reports a simple analytical approximation of the MHC integral that interpolates between exact asymptotic limits for large overpotentials, as well as for large or small reorganization energies, and exhibits less than 5% relative error for all reasonable parameter values. This result enables the MHC model to be considered as a practical alternative to the ubiquitous Butler-Volmer equation for improved understanding and engineering of electrochemical systems [241].

Chapter 6 extends the previous results in the Marcus-Hush-Chidsey (MHC) model to a more complicated asymmetric Marcus-Hush (AMH) model. Recently, experiments have shown that, for a number of electrode reactions, the "symmetric" MHC theory requires two different reorganization energies to fit data. An asymmetric form (asymmetric-Marcus-Hush, AMH) has recently been introduced that is able to capture full data sets with a single reorganization energy. However, the formula involves an improper integral, which must be calculated numerically, potentially limiting practical use. By defining a region over which the formula applies and approximating a minimally varying term as a constant over this region, we take advantage of similarities with the symmetric electrode reaction form (Marcus-Hush-Chidsey, MHC), for

which there are a number of efficient calculation techniques. This enables the AMH reaction model to approach the same ease of usability as the symmetric variant [240].

Chapter 7 summarizes all the progress made within this thesis in the electrochemical system modeling area, and suggests some possible directions for future research based on the current results.

Appendix A addresses theoretically the computational efficiency comparison problem for the minimum curvature mode calculation. Minimum mode following algorithms are widely used for saddle point searching in chemical and material systems. Common to these algorithms is a component to find the minimum curvature mode of the second derivative, or Hessian matrix. Several methods, including Lanczos, dimer, Rayleigh-Ritz minimization, shifted power iteration, and locally optimal block preconditioned conjugate gradient, have been proposed for this purpose. Each of these methods finds the lowest curvature mode iteratively without calculating the Hessian matrix, since the full matrix calculation is prohibitively expensive in the high-dimensional spaces of interest. Here we unify these iterative methods in the same theoretical framework using the concept of the Krylov subspace. The Lanczos method finds the lowest eigenvalue in a Krylov subspace of increasing size, while the other methods search in a smaller subspace spanned by previous search directions. We show that these smaller subspaces are contained within the Krylov space for which the Lanczos method explicitly finds the lowest mode, and hence the theoretical efficiency of the minimum mode finding methods is bounded by the Lanczos method. Numerical tests demonstrate that the dimer method combined with second-order optimizers approaches but does not exceed the efficiency of the Lanczos method for minimum mode optimization [242].

Appendix B works on a cascading model of excitable neural dynamics and shows that over a wide variety of parameter regimes, these systems admit unique attractors. For large coupling strengths, this attractor is a limit cycle, and for small coupling strengths, it is a fixed point. This chapter also shows that the cascading model considered here is a mean-field limit of an existing stochastic model [61].

Chapter 2

Efficient Conservative Numerical Schemes for 1D Nonlinear Spherical Diffusion Equations with Applications in Battery Modeling

2.1 Introduction

The modeling of battery systems in which an atom intercalates into solid particles has received significant attention [15], especially with regard to the Li-ion and Ni/MH chemistries [4, 67, 78, 207, 74, 75]. A popular way to treat diffusion of an insertion atom into a solid phase while avoiding the solution of a full two-dimensional (2D) problem is to construct a pseudo-2D model, in which one dimension extends between the two current collectors and a second dimension extends into the solid particles, with a coupling between the two dimensions at the surface of the intercalation particles. A schematic of the process of spherical diffusion and coupling at the particle surface is shown in Fig. 2-1, where we assume that diffusion occurs in the radial direction in an isotropic medium. Although more complex processes for solid intercalation have been proposed for phase-separating active materials, such as $LiFePO_4$ [191, 52, 188,

8, 48, 47, 15], here we focus only on the most common approximation of 1D spherical diffusion. This approximation is also invoked to model the diffusion impedance of insertion batteries [190].

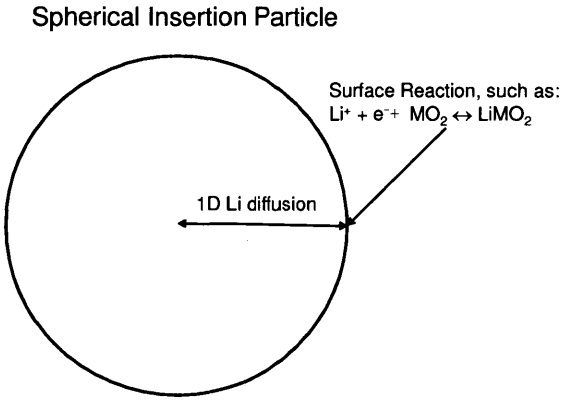

Figure 2-1: Schematic of the physical model addressed in this paper. An electrochemical surface reaction (e.g., involving the insertion and removal of Li from a metal oxide (M=Co, Ni, Mn, or others)) supplies a specified flux of Li at the surface of a spherical particle in which radial, one-dimensional, Fickian diffusion takes place.

The concentration at the surface of the particle should be obtained accurately because it is used in the exchange current density for the interfacial reaction, where its contribution is typically non-linear (a 1/2 power is typical) as well as in the calculation of the equilibrium potential for the interfacial reaction, which is also typically nonlinear [207]. The surface concentration affects the charge-transfer reaction rate and the interfacial potential because it contributes to the activity of the intercalated ions. In a general theory of electrochemical kinetics based on non-equilibrium thermodynamics [15], the surface activity is also affected by concentration gradients [188, 8], elastic coherency strain [48], surface "wetting" [47] and other non-idealities in solids. For an isotropic spherical particle, it can be shown that the general Cahn-Hilliard reaction model [15, 31], which allows for complex thermodynamics with phase separation, reduces to the simple model considered here – spherical diffusion with concentration-dependent kinetics – in the case of a solid-solution material, whose equilibrium state is homogeneous [238].

Several different methods have been employed for the solution of the 1D spherical

diffusion problem, including Duhamel's superposition integral [67], diffusion length method [219], polynomial approximation [194], PSS method [129, 243], penetration depth method [189], finite element method [189], finite difference method [174], and finite volume method. Some methods are only valid under certain circumstance, for instance, Duhamel's superposition integral can only handle the linear problem, requiring the use of a constant diffusion coefficient. In practice solid-phase diffusion coefficients often depend on both composition (i.e., local Li concentration) and temperature, so the ability to solve the case in which the diffusion coefficient can vary is very important. A review of existing methods for solving solid diffusion methods in terms of their numerical performance and restrictions is given by Subramanian [174].

Because each node point within the electrode is coupled to the 1D spherical diffusion problem, the total number of spatially distributed variables to be solved at each timestep (i.e., states) in the model can be increased dramatically by the inclusion of a finely meshed radial spatial dimension. For example, with 50 node points in each electrode (and 20 in the separator), and six equations in the cell sandwich dimension, adding a spherical diffusion dimension with 50 nodes points would increase the number of states in the model from 720 to 5720. This was the original reason for the use of Duhamel's superposition integral (no additional states are added in the particle dimension) [67], and is the reason that significant work has been invested to find efficient computational solutions to the non-linear 1D spherical diffusion problem.

Among the numerical methods that are suitable for solving the solid diffusion problem with a variable diffusion coefficient, the finite volume method is well known for its perfect mass conservation. This property is a great advantage in long term simulations in which a gain or loss of mass can significantly influence simulation results. However, the finite volume method may not be as computationally efficient as other methods such as the finite difference or finite element method. In this paper, we will present another conservative numerical scheme, the control volume method, which is both computationally efficient and simple to implement. To the best of our knowledge, this method and its extension to non-uniform mesh spacing has not been previously published for the spherical diffusion problem, and this work is therefore

an important advance in the ability to solve the spherical diffusion problem with a diffusion coefficient that depends on composition, temperature, or other factors, in a conservative and efficient manner.

We can formulate the process of intercalation of a species into a spherical solid particle with the 1D spherical diffusion equation and the Neumann condition at the particle surface,

$$r^2\frac{\partial c}{\partial t} = \frac{\partial}{\partial r}(Dr^2\frac{\partial c}{\partial r}), \tag{2.1}$$

while the boundary condition is,

$$\frac{\partial c}{\partial r}\Big|_{(r=0)} = 0, \tag{2.2}$$

$$D\frac{\partial c}{\partial r}\Big|_{(r=R_s)} = -j(t). \tag{2.3}$$

The diffusion coefficient may be a function of concentration and spatial position, as well as a function of temperature T and other quantities. All parameters in the partial differential equations system in Eqn. 2.1 are with SI units.

In this work we set the diffusion coefficient to be a function of concentration alone, and use a fit to measurements done on $Li(Ni_{1/3}Mn_{1/3}Co_{1/3})O_2$ [228],

$$\begin{aligned} D(c) &= D^{ref}(1 + 100(SOC)^{\frac{3}{2}}), \\ SOC &= \frac{c^{max} - c}{c^{max}}\frac{\hat{C}_{theory}}{\hat{C}_{practical}}. \end{aligned} \tag{2.4}$$

The values of the parameters used in Eqn. 2.4 are given in Table 2.1.

Table 2.1: Parameter settings for the diffusion coefficient function in Eqn. 2.4.

Parameter Name	Notation	Value	Unit
Reference Diffusivity	D^{ref}	2.00×10^{-16}	m^2/s
Maximum Concentration	C^{max}	4.665×10^4	mol/ m^3
Theoretical Capacity	$\hat{C}_{theory}$	277.84	mAh/g
Practical Capacity	$\hat{C}_{practical}$	160	mAh/g

A plot of the function given by Eqn. 2.4 as well as the original measured data

obtained by Wu et al. [228] are given in Fig. 2-2.

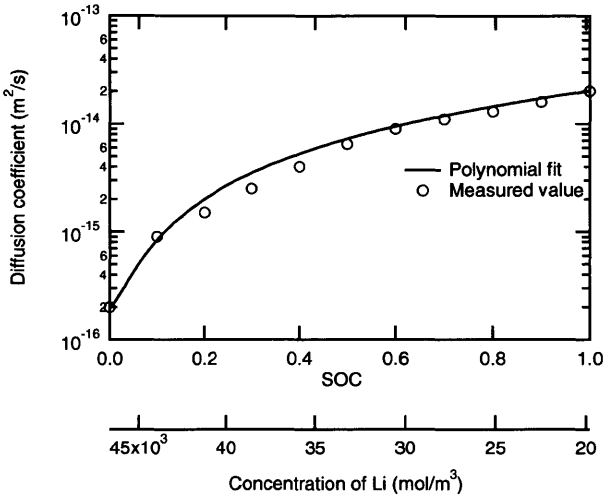

Figure 2-2: Measured values of the lithium diffusion coefficient in $Li(Ni_{1/3}Mn_{1/3}Co_{1/3})O_2$ (circles) and the fitting polynomial function in Eqn. 2.4 (curve) we use for the numerical simulation.

2.2 The Finite Volume and Control Volume Formulations

Before turning to the control volume method, for the sake of comparison we first consider the finite volume method, which is a well-developed numerical discretization method for partial differential equations, especially in the transport problem. The finite volume method is well known for its robustness and efficiency in computations, and most importantly, for its perfect mass conservation. In this section, we first introduce the spatial discretization by the finite volume method, and next analyze the error order of this method.

2.2.1 The Finite Volume Method

Formulation of the Finite Volume Method

The basic idea for the finite volume method is to solve for the integral form of the original PDE. We assume the diffusion coefficient function $D(c)$ is globally Lipschitz [183], then integrate both sides of Eqn. 2.1 over the interval $[r_i, r_{i+1}]$, to get,

$$\frac{\partial \bar{c}_i}{\partial t} V_i = D(\frac{\bar{c}_{i+1} + \bar{c}_i}{2}) r_{i+1}^2 \frac{\bar{c}_{i+1} - \bar{c}_i}{\Delta r} - D(\frac{\bar{c}_i + \bar{c}_{i-1}}{2}) r_i^2 \frac{\bar{c}_i - \bar{c}_{i-1}}{\Delta r} + O(\Delta r^2), \tag{2.5}$$

where $V_i = \frac{1}{3}(r_{i+1}^3 - r_i^3)$ is the scaled volume of the shell between $[r_i, r_{i+1}]$, and $\bar{c}_i$ is the average concentration within this small volume. Since the volume $\frac{4}{3}\pi(r_{i+1}^3 - r_i^3)$ is always canceled with the surface area $4\pi r_i^2$ by the same factor 4π, we will by default use this scaled volume $V_i = \frac{1}{3}(r_{i+1}^3 - r_i^3)$ and scaled surface area r_i^2 without further notation. Eqn. 2.5 holds for each shell, and in fact it gives the spatial discretization of our original PDE system given by Eqn. 2.1.

We may also write each of the above discretized equations in the following matrix form,

$$\mathbf{M}_f \frac{\partial \bar{\mathbf{c}}}{\partial t} = \mathbf{f}(\bar{\mathbf{c}}), \tag{2.6}$$

where $\mathbf{M}_f$ is a mass matrix with the volume of each shell on its diagonal and zero elsewhere, $\mathbf{f}$ is the vector function with each item given by the left hand side of Eqn. 2.5, and $\bar{\mathbf{c}}$ is the vector of average concentration in each shell.

A disadvantage of this method for use in intercalation battery models is that it computes volume-averaged concentrations rather than concentrations spatially located at the node points. Thus, in order to obtain the surface concentration, which determines the equilibrium potential that goes into the exponential of the kinetic expression and is typically part of the exchange-current density, it is necessary to extrapolate the concentration at the particle surface by,

$$c_{\text{surface}} = \frac{3\bar{c}_N - \bar{c}_{N-1}}{2}. \tag{2.7}$$

Error Order Analysis in Spatial Coordinates for the Finite Volume Method

In our system, we will demonstrate that this discretization method in fact achieves second order accuracy in the spatial coordinate. We also show that the surface concentration converges in second order in mesh spacing. To demonstrate this point, instead of proving directly that this finite volume discretization method is in second order, we will derive another second order accurate method and show these two methods are equivalent.

Let c_i be the midpoint concentration of the interval $[r_i, r_{i+1}]$ instead of the average concentration within this shell. Then by Taylor expansion, we can easily get,

$$\begin{aligned} &\frac{\partial}{\partial t}(V_i c_i + O(\Delta r^3)) = \int_{r_i}^{r_{i+1}} r^2 \frac{\partial c}{\partial t} dr = \int_{r_i}^{r_{i+1}} \frac{\partial}{\partial r}(Dr^2 \frac{\partial c}{\partial r}) dr \\ &= D(\frac{c_{i+1}+c_i}{2}) r_{i+1}^2 \frac{c_{i+1}-c_i}{\Delta r} - D(\frac{c_i+c_{i-1}}{2}) r_i^2 \frac{c_i - c_{i-1}}{\Delta r} + O(\Delta r^2). \end{aligned} \tag{2.8}$$

Since this derivation is valid on each interval, the overall error of the above discretization method is of second order, $O(\Delta r^2)$, for both sides of Eqn. 2.1. Thus, this method is of second order accurate in space as desired.

Given that c_{N-1} and c_N are second order accurate, the extrapolation of $c_{\text{surface}} = \frac{2\bar{c}_N - \bar{c}_{N-1}}{2}$ is then obviously second order accurate by Taylor's expansion.

Not surprisingly, Eqn. 2.8 is in exactly the same form as Eqn. 2.5, if we neglect the error term. Therefore, these two discretization methods are equivalent. This finishes our proof that the error of finite volume discretization in Eqn. 2.6 should converge in second order in the spatial coordinate.

Instead of only using the average concentrations of the last two intervals to approach the surface concentration as proposed by Eqn. 2.7, we may use the average concentration from all N intervals to achieve a more accurate surface concentration. Let c_{left} be the nodal concentration on the left boundary of an interval $[r_i, r_{i+1}]$, and c_{right} be the concentration on the right node of the corresponding interval, then by Taylor's expansion we have,

$$\bar{c}_i = \frac{c_{\text{left}} + c_{\text{right}}}{2} + \frac{c_{\text{left}} - c_{\text{right}}}{6} \frac{\Delta r}{r_{i+1}} + O(\Delta r^2). \tag{2.9}$$

Since we have N intervals in total, it gives us N constraints. Yet we have $N+1$ unknown variables of nodal concentration, we may also use two Neumann boundary conditions. Then by solving the least squares problem we can obtain the concentration on each node, including the surface concentration. This may help us to gain a more accurate surface concentration, but still in second order convergence. The effect of this method will be shown in the numerical experiment section.

2.2.2 The Control Volume Method

We have discussed several advantages for using the finite volume method to discretize our PDE system in the previous section, yet this method may not be ideal for our specific spherical diffusion problem in a model of an intercalation battery. We are essentially interested in the concentration at the surface of the particle, which is the quantity that is coupled into the full set of battery model equations, but as mentioned above, the finite volume method does not immediately provide this information. The extrapolation step described above may take additional computation effort and introduce new numerical error. Therefore, here we show the development of a new numerical algorithm that keeps the advantages of the finite volume method while avoiding the extrapolation step.

With this motivation, in this section we derive a new numerical discretization method for our spherical diffusion equation, which we call the control volume method. We will first introduce a basic version of this method, and provide the theoretical proof of the error convergence order. Then a modified version is shown for better mass conservation purpose, together with discussion of its accuracy order. We also show the generalization to a non-uniform grid mesh of this modified control volume method. While the finite-volume method can be used with variable mesh spacing, the extension of the control-volume method to variable mesh spacing is more straightforward.

Derivation of the Control Volume Method

The control volume method is also a numerical scheme that discretizes the PDE according to the integral form of Eqn. 2.1. We now mesh the spatial domain $[0, R_p]$ uniformly with N points, denoted as $r_1, r_2, \cdots, r_N$, while $r_1 = 0$ and $r_N = R_p$. For our convenience, we define Δr to be the distance between two nearby mesh points. We denote $r_i + \frac{1}{2}\Delta r$ as $r_{i+\frac{1}{2}}$ and $r_i - \frac{1}{2}\Delta r$ as $r_{i-\frac{1}{2}}$.

If we integrate the left hand side of the equation over an interval centered at r_i ($i \neq 1, 2$ or N) with width Δr, $[r_{i-\frac{1}{2}}, r_{i+\frac{1}{2}}]$, then we get,

$$\int_{r_i-\frac{1}{2}\Delta r}^{r_i+\frac{1}{2}\Delta r} r^2 \frac{\partial c}{\partial t} dr = \frac{\partial}{\partial t}\left(\int_{r_i-\frac{1}{2}\Delta r}^{r_i} r^2 c dr + \int_{r_i}^{r_i+\frac{1}{2}\Delta r} r^2 c dr\right). \tag{2.10}$$

The function $f(r) = r^2 c(r)$ takes values $r_{i-1}^2 c_{i-1}$ at the mesh point r_{i-1} and $r_i^2 c_i$ at the point r_i. Then for any r in the sub-interval $[r_{i-\frac{1}{2}}, r_i]$, by Taylor's expansion, we can approximate the value of function $f(x)$ by the following equation,

$$f(r) = r_i^2 c_i + (r - r_i)\frac{r_i^2 c_i - r_{i-1}^2 c_{i-1}}{\Delta r} + O(\Delta r^2). \tag{2.11}$$

Similarly, in the sub-interval $[r_i, r_{i+\frac{1}{2}}]$, we apply the same technique and get,

$$f(r) = r_i^2 c_i + (r - r_i)\frac{r_{i+1}^2 c_{i+1} - r_i^2 c_i}{\Delta r} + O(\Delta r^2). \tag{2.12}$$

Putting these two formulae back into Eqn. 2.10, we get,

$$\int_{r_i-\frac{1}{2}\Delta r}^{r_i+\frac{1}{2}\Delta r} r^2 \frac{\partial c}{\partial t} dr = \Delta r \frac{\partial}{\partial t}\left(\frac{1}{8} r_{i+1}^2 c_{i+1} + \frac{6}{8} r_i^2 c_i + \frac{1}{8} r_{i-1}^2 c_{i-1} + O(\Delta r^2)\right). \tag{2.13}$$

If we also integrate the right hand side of Eqn. 2.1 as we did for the finite volume method, and equate the two sides, we obtain,

$$\begin{aligned} &\Delta r \frac{\partial}{\partial t}\left(\frac{1}{8} r_{i-1}^2 c_{i-1} + \frac{6}{8} r_i^2 c_i + \frac{1}{8} r_{i+1}^2 c_{i+1} + O(\Delta r^2)\right) \\ &= \left(D\left(\frac{c_{i+1} + c_i}{2}\right) r_{i+\frac{1}{2}}^2 \frac{c_{i+1} - c_i}{\Delta r} - D\left(\frac{c_i + c_{i-1}}{2}\right) r_{i-\frac{1}{2}}^2 \frac{c_i - c_{i-1}}{\Delta r} + O(\Delta r^2)\right). \end{aligned} \tag{2.14}$$

Since the boundary condition is the Neumann condition, it can be easily handled in this control volume method in the same way as the finite volume method.

From the error terms above, we see that this method is also second order accurate in the spatial discretization. However, this method has two main problems. First since we have no information about c_1 due to $x_1 = 0$, then we have $N-1$ unknown variables but N equations, which shows the system is over-determined. Second, if we sum up Eqn. 2.14 of each interval, we get,

$$\frac{\partial}{\partial t}(\sum_{i=1}^{N-1} r_i^2 c_i + \frac{1}{2} r_N^2 c_N) + j\frac{r_N^2}{\Delta r} = 0. \tag{2.15}$$

If we apply the constant flux for some time period Δt then relax the system to make the concentration flat in the entire domain, the concentration increment should be the same in the whole spatial coordinate. However, let $V_{\text{total}} = \lim_{N\to\infty}(\sum_{i=1}^{N-1} r_i^2 + \frac{1}{2}r_N^2)\Delta r = \frac{1}{3}r_N^3$ be the total particle volume, we have,

$$V_{\text{total}}\Delta c \neq (\sum_{i=1}^{N-1} r_i^2 + \frac{1}{2}r_N^2)\Delta c = -j\frac{r_N^2}{\Delta r}\Delta t. \tag{2.16}$$

The concentration increment is always off from the true value for a certain percentage, which violates the mass conservation law of our system.

Modification for Mass Conservation

In order to fix the problems described above, we replace $r_i^2\Delta r$ by the volume V_i of the corresponding shell $[r_{i-\frac{1}{2}}, r_{r+\frac{1}{2}}]$. For example,

$$V_i = \frac{(r_i + \frac{\Delta r}{2})^3 - (r_i - \frac{\Delta r}{2})^3}{3} = r_i^2\Delta r + \frac{1}{12}\Delta r^3. \tag{2.17}$$

Keeping the right hand side of Eqn. 2.14 unchanged, we then obtain,

$$\begin{aligned} &\frac{\partial}{\partial t}(\frac{1}{8}V_{i-1}c_{i-1} + \frac{6}{8}V_i c_i + \frac{1}{8}V_{i+1}c_{i+1} + O(\Delta r^3)) \\ &= (D(\frac{c_{i+1}+c_i}{2})r_{i+\frac{1}{2}}^2\frac{c_{i+1}-c_i}{\Delta r} - D(\frac{c_i+c_{i-1}}{2})r_{i-\frac{1}{2}}^2\frac{c_i-c_{i-1}}{\Delta r} + O(\Delta r^2)). \end{aligned} \tag{2.18}$$

Like Eqn. 2.14, this discretization scheme is also order Δr^2.

We can further write the new Eqn. 2.18 into a matrix form, which is similar to the equation system Eqn. 2.6,

$$\mathbf{M}_c \frac{\partial \mathbf{c}}{\partial t} = \mathbf{f}(\mathbf{c}), \tag{2.19}$$

where $\mathbf{c}$ is the vector of concentration on each node point, and $\mathbf{M}_c$ is a tri-diagonal mass matrix as following,

$$\mathbf{M}_c = \begin{pmatrix} \frac{3}{4}V_1 & \frac{1}{8}V_2 & 0 & 0 & \cdots & 0 & 0 & 0 \\ \frac{1}{4}V_1 & \frac{6}{8}V_2 & \frac{1}{8}V_3 & 0 & \cdots & 0 & 0 & 0 \\ 0 & \frac{1}{8}V_2 & \frac{6}{8}V_3 & \frac{1}{8}V_4 & \cdots & 0 & 0 & 0 \\ \vdots & \vdots & \vdots & \vdots & \ddots & \vdots & \vdots & \vdots \\ 0 & 0 & 0 & 0 & \cdots & \frac{1}{8}V_{N-2} & \frac{6}{8}V_{N-1} & \frac{1}{4}V_N \\ 0 & 0 & 0 & 0 & \cdots & 0 & \frac{1}{8}V_{N-1} & \frac{3}{4}V_N \end{pmatrix}, \tag{2.20}$$

With this modification, we keep the second order spatial accuracy as the original control volume method as shown by Eqn. 2.18, while we now have access to c_1 since $V_1 \neq 0$. Furthermore, if we sum all the equations of each shell, we get,

$$\sum_{i=1}^{N} V_i \frac{\partial c_i}{\partial t} + j r_N^2 = 0. \tag{2.21}$$

This satisfies the mass conservation condition exactly.

Non-uniform Grid Spacing

Since the boundary of each control volume is either at the center of the particle, surface of the particle, or the midpoint of two nodes, we can still approximate the variable c and its derivative at such a boundary in second order with only two nearby points. This largely reduces the computation complexity and the implementation difficulty of moving the above method from uniform mesh to non-uniform mesh compared to other numerical methods such as finite volume or finite difference.

The control volume discretized formula for non-uniform mesh grids can be written

as the following,

$$\begin{aligned}&\frac{\partial}{\partial t}(\frac{1}{8}V_{i-1}c_{i-1}+\frac{6}{8}V_ic_i+\frac{1}{8}V_{i+1}c_{i+1})\\&=D(\frac{c_{i+1}+c_i}{2})(\frac{r_{i+1}+r_i}{2})^2\frac{c_{i+1}-c_i}{r_{i+1}-r_i}-D(\frac{c_i+c_{i-1}}{2})(\frac{r_i+r_{i-1}}{2})^2\frac{c_i-c_{i-1}}{r_i-r_{i-1}}.\end{aligned}\tag{2.22}$$

where V_i here is the volume of a small control volume $[\frac{r_{i-1}+r_i}{2}, \frac{r_i+r_{i+1}}{2}]$ around the grid point r_i.

2.2.3 Time Domain Discretization

We have now introduced two different methods to discretize the spatial coordinate of the PDE system in Eqn. 2.1. With the differential Eqn. 2.6 and Eqn. 2.19, now we also need to seek for a time domain numerical discretization method to solve this problem. In this section, we first prove the systems Eqn. 2.6 and Eqn. 2.19 are both ordinary differential equations, instead of differential algebraic equations, as the former can be solved much more easily. Then we derive the formula for the implicit time solver we used in solving both ordinary differential equation systems, the Crank-Nicolson method.

Proof of ODE Systems

In order to prove the differential Eqn. 2.6 and Eqn. 2.19 are both ordinary differential equations, it is sufficient to prove the mass matrices $\mathbf{M}_f$ and $\mathbf{M}_c$ are both nonsingular. The only assumption we make here is that the volume V_i is not zero for each i. The mass matrix $\mathbf{M}_f$ is a diagonal matrix, with $V_i \neq 0$ on each diagonal entry by our assumption. Then the statement that $\mathbf{M}_f$ is nonsingular follows immediately.

To prove that the mass matrix $\mathbf{M}_c$ is nonsingular, we can write $\mathbf{M}_c$ as a product

of two matrices $\mathbf{M}_1$ and $\mathbf{M}_2$,

$$\mathbf{M}_c = \begin{pmatrix} \frac{3}{4} & \frac{1}{8} & 0 & 0 & \cdots & 0 & 0 & 0 \\ \frac{1}{4} & \frac{6}{8} & \frac{1}{8} & 0 & \cdots & 0 & 0 & 0 \\ 0 & \frac{1}{8} & \frac{6}{8} & \frac{1}{8} & \cdots & 0 & 0 & 0 \\ \vdots & \vdots & \vdots & \vdots & \ddots & \vdots & \vdots & \vdots \\ 0 & 0 & 0 & 0 & \cdots & \frac{1}{8} & \frac{6}{8} & \frac{1}{4} \\ 0 & 0 & 0 & 0 & \cdots & 0 & \frac{1}{8} & \frac{3}{4} \end{pmatrix} \begin{pmatrix} V_1 & 0 & \cdots & 0 & 0 \\ 0 & V_2 & \cdots & 0 & 0 \\ \vdots & \vdots & \ddots & \vdots & \vdots \\ 0 & 0 & \cdots & V_{N-1} & 0 \\ 0 & 0 & \cdots & 0 & V_N \end{pmatrix} = \mathbf{M}_1\mathbf{M}_2. \tag{2.23}$$

$\mathbf{M}_2$ is nonsingular by the same proof as that $\mathbf{M}_f$ is nonsingular. By Gershgorin's circle theorem [79], all eigenvalues of the matrix $\mathbf{M}_1$ are located within the circle centered at $\frac{6}{8}$ with radius $\frac{3}{8}$ on the complex plane. Therefore, 0 is not an eigenvalue to the matrix $\mathbf{M}_1$ and $\mathbf{M}_1$ is also a nonsingular matrix. It follows that the product of $\mathbf{M}_1$ and $\mathbf{M}_2$, $\mathbf{M}_c$, is also nonsingular. This finishes the proof that the discretized system Eqn. 2.19 is an ODE system.

The Crank-Nicolson Method

The Crank-Nicolson method is a combination of the forward and backward Euler's methods that is used for solving ordinary differential equations with second order accuracy in the time discretization. It is widely used to time-integrate the diffusion equation in stable finite difference schemes [192]. The basic idea involves centered differencing, similar to the control volume method developed above for the spatial integration. Given an initial concentration profile $\mathbf{c}^t$ and the time step size Δt, the prediction of concentration profile $\mathbf{c}^{t+\Delta t}$ at time $t + \Delta t$ satisfies,

$$\mathbf{M}\frac{\mathbf{c}^{t+\Delta t} - \mathbf{c}^t}{\Delta t} = \frac{1}{2}(\mathbf{f}(\mathbf{c}^{t+\Delta t}) + \mathbf{f}(\mathbf{c}^t)), \tag{2.24}$$

where $\mathbf{M}$ is the corresponding mass matrix.

It is equivalent to rewrite our problem in the following way. For each time step,

we need to solve for $\mathbf{c}^{t+\Delta t}$ such that,

$$\mathbf{g}(\mathbf{c}^{t+\Delta t}) = \mathbf{M}\frac{\mathbf{c}^{t+\Delta t} - \mathbf{c}^{t}}{\Delta t} - \frac{1}{2}(\mathbf{f}(\mathbf{c}^{t+\Delta t}) + \mathbf{f}(\mathbf{c}^{t})) = 0. \tag{2.25}$$

To solve such a nonlinear algebraic system we employ Newton's method with an initial guess $\mathbf{c}^{t+\Delta t} = \mathbf{c}^{t}$. We can reduce the computation cost by taking advantage of the fact that the Jacobian matrix of function $\mathbf{g}$ with respect to $\mathbf{c}^{t+\Delta t}$ can be obtained analytically [45], thereby avoiding the need to calculate the Jacobians numerically in each iteration. When the diffusion coefficient D is a constant, the vector function $\mathbf{f}$ is then linear to the variable $\mathbf{c}^{t+\Delta t}$. Therefore, it takes only one step to reach the solution.

2.3 Numerical Results

In this section we will show the results from numerical experiments for both the finite volume and control volume discretization methods coupled to the Crank-Nicolson solver. The numerical convergence order in both space and time coordinates will be demonstrated. We will also discuss the effects of the grid point locations on the numerical error, from which we may see that by optimizing the grid point locations for the diffusion coefficient function and parameter set we use here, we can considerably reduce the number of grid points while maintaining the same or even achieving higher accuracy.

In our numerical simulation, we select a parameter set that is typical for a lithium ion battery cathode active material. We use the diffusion coefficient function shown in Eqn. 2.4, and the choice of particle radius, surface flux and initial concentration shown in Table 4.1. The surface flux value, j, in Table 4.1 corresponds to a C-rate of about 4.3 C (corresponding to a full discharge in about 14 min), a rate that is reasonable for a PHEV vehicle battery.

A typical concentration distribution profile during the intercalation of lithium is shown in Fig. 2-3.

Table 2.2: Parameter settings for numerical experiments.

Parameter Name	Notation	Value	Unit
Particle Radius	R_p	5×10^{-6}	m
Surface Flux	j	-5.35×10^{-5}	mol/ m^2 /s
Initial Concentration	C_0	2×10^4	mol / m^3
Max Concentration	C_m	4.665×10^4	mol / m^3

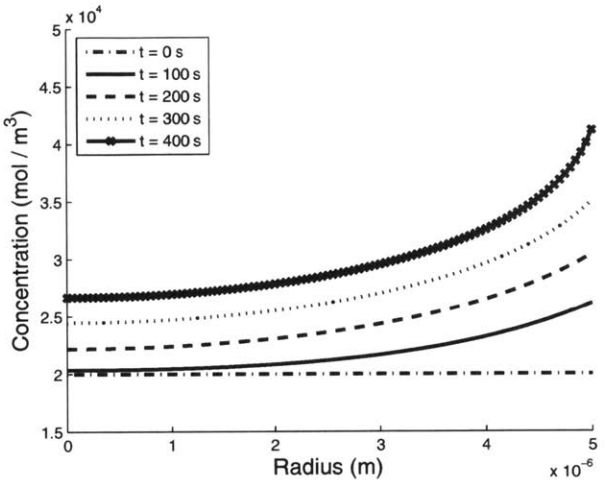

Figure 2-3: Concentration Distribution within the spherical particle. The curves from bottom to top respectively represent the concentration distributions at time $t = 0$, 100 , 200 , 200 and 400 seconds simulation time with a time step size of 5 seconds.

2.3.1 Error Order Analysis

As demonstrated analytically in the previous sections, we expect second order accuracy in space and time for both the finite volume and the control volume discretization coupling to the Crank-Nicolson method.

Since we are mostly interested in the surface concentration in our simulation, we define the error in terms of the accuracy of the surface concentration at the end of our simulation. We use the solution from a very fine grid mesh (50001 points) as our reference solution in the error convergence test.

It is clear from Fig. 2-4 that the finite volume method with two different extrapolations and the control volume method are in the second order as expected. However, for fixed grid numbers, the control volume method is more accurate than the finite volume method by a factor of about 10. This shows one of the advantages of using

the control volume method in the simulation.

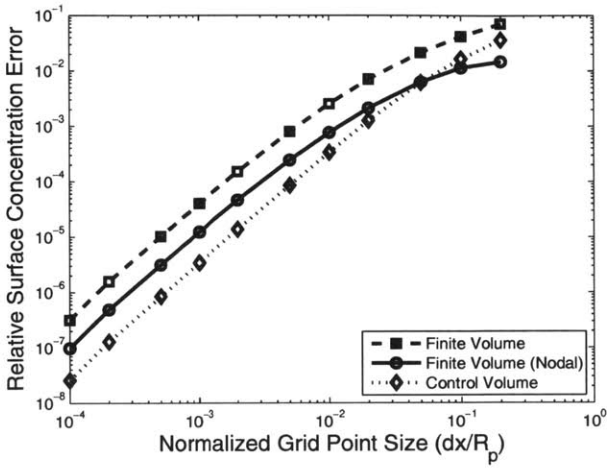

Figure 2-4: Plot showing the relative error convergence order of three numerical schemes in the spatial coordinate. The curve of finite volume method with extrapolation method Eqn. 2.7 is shown by the dash line with square marker, and the solid line with circle marker represents the finite volume method with extrapolation method Eqn. 2.9. The dot curve with diamond marker represents the control volume method. The relative error is defined as the error of surface concentration over the reference surface concentration. The total simulation time is 400 second with a time step of 5 seconds.

For the time dimension, similar to the way we conduct the spatial error convergence test, we fixed the mesh size to be 101 uniform grid points and then varied the time step sizes. In addition, we took the solution with very small time step size (0.002 s per step) and the same mesh (101 grid points) as our reference solution.

From Fig. 2-5, the slope of the log-log plot is 2, which indicates that for the given mesh size, all three numerical methods are second order accurate in time, which is consistent with our previous derivation of the Crank-Nicolson method.

2.3.2 Effects of Grid Point Positions

In the previous discussions of different numerical methods, we worked only with a uniform mesh within the spatial domain. Due to the physics of the problem, a Neumann boundary condition is required, such that the concentration in the region closest to the particle surface should change more rapidly than the region closest to

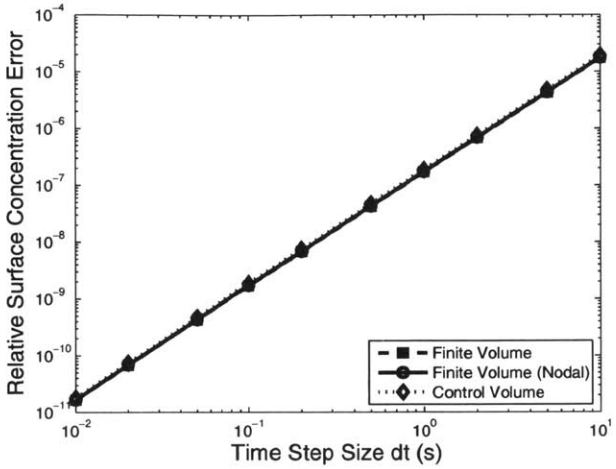

Figure 2-5: Plot of the relative error convergence order of three numerical schemes in the time coordinate. The curve of the finite volume method with extrapolation method Eqn. 2.7 is shown by the dash line with the square marker, and the solid line with the circle marker represents the finite volume method with extrapolation method Eqn. 2.9. The dot curve with diamond marker represents the control volume method. The relative error is defined as the error of surface concentration over the reference surface concentration. The total simulation time is 400 second with a 101-uniform-grid-point mesh.

the center. Furthermore, we are particularly interested in the surface concentration because of its use in other equations in our battery model. Therefore, it may be a good idea to use a non-uniform spatial mesh with more grid points closest to the surface, in order to achieve a better accuracy and/or a shorter simulation time.

Indeed, we find that the locations of the grid points have a significant influence on the numerical accuracy. Instead of using a constant flux, now we apply a varying flux by simulating a driving cycle. The driving cycle is composed of a series of surface fluxes, each applied for a duration of 1 second, and represents a real-world load profile applied in a vehicle application. The drive cycle we use consists of a period of city driving with a relatively low average load, followed by a period of highway driving with a higher average load, followed by a second period of city driving.

From Fig. 2-6, we see that with 21 grid points, if we increase the density near the surface, we can achieve more than 10 times higher accuracy in the surface concentration than with the same number of uniform mesh grids, which means we may

largely reduce the grid point number and keep the original accuracy by just changing the mesh locations. The mesh point locations are given by,

$$\vec{x} = \frac{\text{logspace}(0,a,10)-1}{10^a - 1}, \tag{2.26}$$

where logspace(.) is a function in MATLAB that provides logarithmically equally spaced points (in base 10) and a is some negative number we varied from 0 (uniform grid in this case) to 4. The form of Eqn. 2.26 was chosen merely because it conveniently distributes most of the grid points near the particle surface, and is not the result of an optimization or systematic study of grid point placement.

Fig. 2-6(a) shows the surface concentration as a function of time. The slope of the surface concentration vs. time is a rough indicator of the average load on the particle. The inset in Fig. 2-6(a) shows that 21 non-uniform grid points can provide a surface concentration that is much closer to the converged solution (with 501 uniform grid points) than 21 uniform mesh points. Root-mean-square (RMS) errors for the entire simulation duration are also given in the legend of Fig. 2-6(a). Achieving an accuracy in the equilibrium potential of the $Li(Ni_{1/3}Mn_{1/3}Co_{1/3})O_2$ material in reference [228] of 1.0 mV requires an accuracy in the surface concentration of about 10 mol/m^3 (for all but the tail region below about 3.6V vs. Li). As accurate battery simulations require highly accurate equilibrium potential values, achieving an RMS error in the surface concentration that is below 10 mol/m^3 is desirable. Fig. 2-6(a) shows that 21 non-uniform grid points can reach such a target, while 21 non-uniform grid points give an RMS error in the surface concentration that is far above that bound. 138 uniformly spaced grid points are required to match the RMS error of the 21 non-uniform grid points, demonstrating a 6.57x reduction in the number of grid points is possible for the parameters and drive cycle used here. Fig. 2-6(b) shows that while the RMS error of the surface concentration with 21 non-uniform grid points is below 10 mol/m^3, there are points in the drive cycle when the error is significantly higher, demonstrating the need for a battery modeler to carefully select model parameters (including number of mesh points and mesh point spacing) that give an accuracy

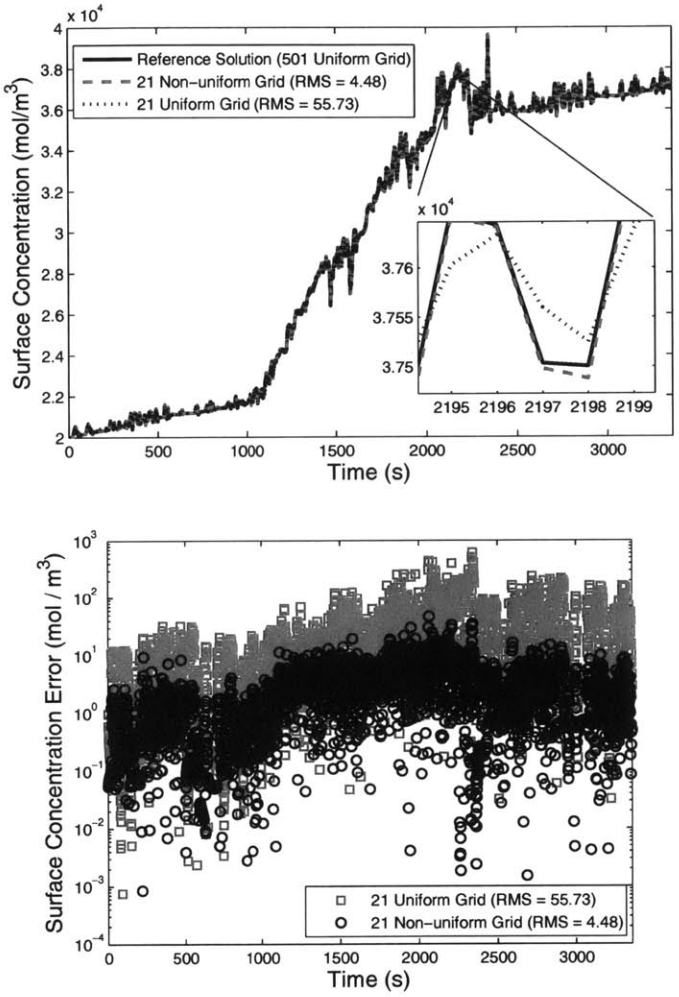

Figure 2-6: The surface concentration over time with 501 uniform grids (the reference solution, black solid curve), 21 non-uniform grids (grey dash curve) and 21 uniform grids (grey dot curve) are shown in the top subfigure (a), while the corresponding relative errors in surface concentrations over time with 21 uniform grids (grey squares) and 21 non-uniform grids (black circles) are shown in the bottom subfigure (b). We may see the performance from 21 non-uniform grid points is significantly better than the outcome from 21 uniform grids. The RMS (short for "root mean square") error for uniform grid is 55.73 while the RMS error for non-uniform grid is only 4.48. We choose the parameter $a = -1.5$ in Eqn. 2.26 for the non-uniform grid.

suitable for the modeling purpose.

The dramatic reduction in the number of required points while maintaining a high accuracy provides inspiration to optimize the grid point location based on the particle sizes, diffusion coefficient (including functional forms that describe the dependence of the diffusion coefficient on concentration), and input flux profile [174]. The goal is to

allocate mesh points within the spatial domain while maintaining the same surface concentration solution from the coarse, nonuniform grid and the very fine, uniform grid. With this coarse mesh, we may significantly reduce the simulation time of this spherical diffusion process.

2.4 Conclusion

By carefully comparing the finite volume and control volume methods as applied to the 1D, non-linear, spherical diffusion problem, we have shown that the advantages of the control volume method include directly obtaining the surface concentration rather than obtaining a volume-averaged concentration, a higher solution accuracy for a given number of node points, and a straightforward extension of the method to non-uniform grid spacing that can significantly reduce computational time by selectively placing grid points where concentrations gradients are highest.

We have quantified the errors in the surface concentration that comes from both uniform and non-uniform meshes and compared the errors with an accurate solution. Our results underscore the importance of understanding the impact of the numerical solution technique for the solid transport process in order to achieve an accuracy appropriate for the modeling purpose, as the surface concentration (or activity) determines both the equilibrium potential and exchange current density typically used in battery models. The control volume method can also be extended to solving accurately more complex battery models [238], such as the fourth-order, nonlinear Cahn-Hilliard reaction model [15], where the surface activity also depends on concentration gradients and elastic stresses. extended to solving accurately more complex battery models [238], such as the fourth-order, nonlinear Cahn-Hilliard reaction model [15], where the surface activity also depends on concentration gradients and elastic stresses.

Chapter 3

Phase Separation Dynamics in Isotropic Ion-Intercalation Particles

3.1 Introduction

The discovery of lithium iron phosphate (Li_xFePO_4, LFP) as a cathode material for lithium-ion batteries has led to unexpected breakthroughs in the mathematical theory of chemical kinetics coupled to phase transformations [15]. Since its discovery in 1997 as a "low power material" with attractive safety and economic attributes [165], LFP has undergone a remarkable reversal of fortune to become the cathode of choice for high-power applications [204, 109, 203], such as power tools and electric vehicles [176, 236], through advances in surface coatings and reduction to nanoparticle form.

A striking feature of LFP is its strong tendency to separate into stable high density and low density phases, indicated by a wide voltage plateau at room temperature [165, 204] and other direct experimental evidence [58, 232, 59, 5, 164, 46]. Similar phase-separation behavior arises in many other intercalation hosts, such as graphite, the typical lithium insertion anode material, which exhibits multiple stable phases. This has inspired new approaches to model the phase separation process coupled to electrochemistry, in order to gain a better understanding of the fundamental lithium-ion battery dynamics.

The first mathematical model on two-phase intercalation dynamics in LFP was

proposed by Srinivasan and Newman [191], based on the concept of a spherical "shrinking core" of one phase being replaced by an outer shell of the other phase, as first suggested by Padhi et al. [165]. By assuming isotropic spherical diffusion, the sharp, radial "core-shell" phase boundary can be moved in proportion to the current. This single-particle model was incorporated into traditional porous electrode theory for Li-ion batteries [67, 155] with Butler-Volmer kinetics and concentration dependent diffusivity and fitted to experiments. The shrinking-core porous-electrode model was recently extended and refitted by Dargaville and Farrell [52].

In recent years, the shrinking-core hypothesis has been called into question because different phase behavior has been observed experimentally [121, 38, 5, 59, 46] and predicted theoretically [15]. It has become clear that a more realistic particle model must account for two-phase thermodynamics [89, 188, 123, 124, 238], crystal anisotropy [188, 8, 202], coherency strain [48, 47] and reaction limitation in nanoparticles [188, 8, 74]. In larger, micron-sized particles, the shrinking-core model may still have some relevance due to solid diffusion limitation and defects (such as dislocations and micro cracks) that can reduce coherency strain [188, 31, 51]. Moreover, diffusion becomes more isotropic in larger particles due to the increased frequency of point defects, such as channel-blocking Fe anti-site defects in LFP [133].

Regardless of the details of the model, fundamental questions remain about the dynamics of phase separation driven by electrochemical reactions, even in the simplest case of an isotropic strain-free spherical particle. When should we expect core-shell phase separation versus pure diffusion in a solid solution? What other transient phase morphologies are possible? How are reaction kinetics affected by phase separation? Traditional battery models, which place artificial spherical phase boundaries and assume classical Butler-Volmer kinetics, are not able to answer these questions.

In this article, we formulate a simple mathematical model that captures the essential features of *bulk* phase separation coupled to Faradaic intercalation reactions in a single solid nanoparticle. The model is based on a recently developed mathematical theory of chemical reaction and charge transfer kinetics based on nonequilibrium thermodynamics [15], which we review in Section 3.2. In the case of an isotropic,

strain-free spherical particle, the resulting Cahn-Hilliard reaction (CHR) equations are formulated for Butler-Volmer (BV) kinetics and regular solution thermodynamics in Section 3.3. The model predicts smooth concentration profiles limited by radial diffusion with smooth voltage profiles versus state of charge in cases of solid-solution thermodynamics (Section 3.4) and radial phase separation with a flat voltage plateau in cases of two stable phases (Section 3.5), which are strongly affected by surface wetting (Section 3.6). After summarizing the results, in Section 3.7 we present the control-volume numerical scheme for the CHR model that allows us to accurately solve this stiff fourth-order nonlinear initial-boundary-value problem.

3.2 Background

A systematic approach to describe chemical kinetics coupled to phase transformations has recently been developed by Bazant [15], based on nonequilibrium thermodynamics. The theory leads to a general reaction-diffusion equation of the form,

$$\frac{\partial c_i}{\partial t} = \nabla \cdot \left(M_i c_i \nabla \frac{\delta G}{\delta c_i} \right) + R_i \left(\left\{ \frac{\delta G}{\delta c_j} \right\} \right) \tag{3.1}$$

where c_i is the concentration, M_i the mobility, and R_i the volumetric reaction rate of species i, assuming homogeneous kinetics. The diffusive flux (second term) and the reaction rate (third term) are both expressed in terms of diffusional chemical potentials,

$$\mu_i = \frac{\delta G}{\delta c_i} \tag{3.2}$$

defined as variational derivatives of the total free energy functional $G[\{c_i\}]$. Physically, $\mu_i(x)$ is free energy required to add a continuum "particle" (delta function) of species i to the system at position x. For the conversion of reactants $\{A_r\}$ to products $\{B_p\}$,

$$\sum_r s_r \mathrm{A}_r \rightarrow \sum_p s_p \mathrm{B}_p, \tag{3.3}$$

assuming thermally activated kinetics, the reaction rate has the general variational form,

$$R = \frac{k_0}{\gamma_\ddagger}\left[\exp\left(\sum_r \frac{s_r}{k_B T}\frac{\delta G}{\delta c_r}\right) - \exp\left(\sum_p \frac{s_p}{k_B T}\frac{\delta G}{\delta c_p}\right)\right] \tag{3.4}$$

where $\gamma_\ddagger$ is the activity coefficient of the transition state and $R_i = \pm s_i R$ (+ for products, − for reactants). A mathematical model of the general form (3.1) was perhaps first proposed by Hildebrand *et al.* to describe nanoscale pattern formation in catalytic surface reactions [102, 101] and corresponds to specific models for the free energy (G) and the transition state ($\gamma_\ddagger$). In the case of electrochemical reactions involving ions and electrons, different assumptions that also account for electrostatic energy lead to generalizations of the classical Butler-Volmer and Marcus theories of charge transfer for concentrated solutions and solids [15].

The variational reaction-diffusion equation (3.1) unifies the Cahn-Hilliard and Allen-Cahn equations from phase-field modeling in a general formulation of non-equilibrium chemical thermodynamics for reacting mixtures. These classical equations, widely used in materials science and applied mathematics [10], are special cases of Eq. (3.1) that correspond to rate limitation by diffusion,

$$\frac{\partial c}{\partial t} = \nabla \cdot \left(Mc\nabla\frac{\delta G}{\delta c}\right) \quad \text{(Cahn-Hilliard)} \tag{3.5}$$

or by linear reaction kinetics for a small thermodynamic driving force,

$$\frac{\partial c}{\partial t} = -k\frac{\delta G}{\delta c} \quad \text{(Allen-Cahn)} \tag{3.6}$$

respectively [188, 15]. The general equation (3.1) can be applied to many problems in chemical or electrochemical dynamics [15]. In the case of ion intercalation in Li-ion battery nanoparticles, it has mainly been studied in two limiting cases.

For reaction-limited anisotropic nanoparticles, the general theory can be reduced to the Allen-Cahn reaction (ACR) equation,

$$\frac{\partial c}{\partial t} = R\left(\left\{\frac{\delta G}{\delta c}\right\}\right) \quad \text{(ACR)} \tag{3.7}$$

for the depth-averaged ion concentration $c(x, y)$ along the active surface where intercalation reactions occur, as shown by Bai et al. [8] and Burch [30], building on the seminal paper of Singh et al. [188]. The ACR model has been applied successfully to predict experimental data for LFP, using generalized Butler-Volmer kinetics and accounting for coherency strain, by Cogswell and Bazant [48, 47, 15]. An important prediction of the ACR model is the dynamical suppression of phase separation at high rates [8, 48], as it becomes favorable to spread reactions uniformly over the particle surface, rather than to focus them on a thin interface between stable phases. The ACR model has also been used to predict a similar transition in electrochemical deposition of Li_2O_2 in Li-air battery cathodes, from discrete particle growth at low currents to uniform films at high currents [104].

For larger particles, the Cahn-Hilliard reaction (CHR) model,

$$\frac{\partial c}{\partial t} + \nabla \cdot \mathbf{F} = 0, \quad \mathbf{F} = -Mc\nabla\frac{\delta G}{\delta c_i}, \quad -\hat{n} \cdot \mathbf{F} = R\left(\left\{\frac{\delta G}{\delta c}\right\}\right) \quad \text{(CHR)} \tag{3.8}$$

describes bulk phase separation driven by heterogenous reactions, which are localized on the surface and described by a flux matching boundary condition [15]. This general model was first posed by Singh, Ceder and Bazant [188] but received less attention until recently. For Butler-Volmer kinetics, Burch and Bazant [31, 30] and Wagemaker et al. [218] solved the CHR model in one dimension to describe size-dependent miscibility in nanoparticles. Dargaville and Farrell [51, 53] first solved CHR in two dimensions (surface and bulk) for a rectangular particle using a least-squares based finite-volume method [54] and examined the transition to ACR behavior with increasing crystal anisotropy and surface reaction limitation. They showed that phase separation tends to persist within large particles, similar to the shrinking core picture, if it is not suppressed by coherency strain and/or fast diffusion perpendicular to the most active surface.

3.3 Cahn-Hilliard Reaction Model

In this work, we solve the CHR model with generalized Butler-Volmer kinetics for a spherical host particle with the intercalated ion concentration varying only in the radial direction. Spherical symmetry is also the most common approximation for solid diffusion in traditional Li-ion battery models [67, 239]. This simple one-dimensional version of the CHR model is valid for large, defective crystals with negligible coherency strain and isotropic diffusion [188, 30, 51, 53]. It may also be directly applicable to low-strain materials such as lithium titanate [160], a promising long-life anode material [234]. We simulate phase separation dynamics at constant current, which sometimes, but not always, leads to shrinking-core behavior. Related phase-field models of isotropic spherical particles, including the possibility of simultaneous crystal-amorphous transitions, have also been developed and applied to LFP by Tang et al. [201, 203], Meethong et al. [145, 144, 146], and Kao et al [110], but without making connections to charge-transfer theories from electrochemistry. Here, we focus on the electrochemical signatures of different modes of intercalation dynamics – voltage transients at constant current – which are uniquely provided by the CHR model with consistent Butler-Volmer reaction kinetics [15]. We also consider the nucleation of phase separation by surface wetting [8], in the absence of coherency strain, which would lead to a size-dependent nucleation barrier [47] and symmetry-breaking striped phase patterns [60, 48].

3.3.1 Model formulation

Consider the CHR model (3.8) for a spherical, isotropic, strain-free, electron-conducting particle of radius R_p with a concentration profile $c(r,t)$ of intercalated ions (number/volume). As first suggested by Han et al. for LFP [89], we assume the chemical potential of the Cahn-Hilliard regular solution model [33, 34, 35],

$$\mu = k_B T \ln\left(\frac{c}{c_m - c}\right) + \Omega\left(\frac{c_m - 2c}{c_m}\right) - \frac{\kappa}{c_m^2}\nabla^2 c, \tag{3.9}$$

where k_B is Boltzmann's constant, T the absolute temperature, Ω the enthalpy of mixing per site, κ the gradient energy penalty coefficient, V_s the volume of each intercalation site, and $c_m = V_s^{-1}$ is the maximum ion density. Although we account for charge transfer at the surface (below), we set the bulk electrostatic energy to zero, based on the assumption each intercalated ion diffuses as a neutral polaron, coupled to an adjacent mobile electron, e.g. reducing a metal ion such as $Fe^{3+} + e^- \rightarrow Fe^{2+}$ in LFP. (For semiconducting electrodes, imbalances in ion and electron densities lead to diffuse charge governed by Poisson's equation in the CHR model [15].)

The mobility M in the flux expression (3.8) is related to the tracer diffusivity D by the Einstein relation, $D = Mk_BT$. For thermodynamic consistency with the regular solution model, the tracer diffusivity must take into account excluded sites

$$D = D_0\left(1 - \frac{c}{c_m}\right) = Mk_BT \tag{3.10}$$

where D_0 is the dilute-solution limit, which leads to the "modified Cahn-Hilliard equation" [153]. This form also follows consistently from our reaction theory, assuming that the transition state for solid diffusion excludes two sites [15].

At the surface of the particle, $R = R_p$, the insertion current density $I(t)$ is related to the voltage $V(t)$ and surface flux density $F(R_p, t)$, where $\mathbf{F} = F\hat{R}$ is the radial flux. By charge conservation, the current is the integral of the surface flux times the charge per ion ne,

$$I = -neF(R_p, t), \tag{3.11}$$

where e is the electron charge. Electrochemistry enters the model through the current-voltage relation, $I(V, c, \mu)$, which depends on c and μ at the surface. Here, we adopt thermodynamically consistent, generalized Butler-Volmer kinetics for the charge-transfer rate [15], given below in dimensionless form.

We also impose the "natural" or "variational" boundary condition for the fourth-order Cahn-Hilliard equation,

$$\frac{\partial c}{\partial r}(R_p, t) = c_m^2 \frac{\partial \gamma_s}{\partial c}, \tag{3.12}$$

where $\gamma_s(c)$ is the surface energy per area, which generally depends on ion concentration. The natural boundary condition expresses continuity of the chemical potential and controls the tendency for a high or low concentration solid phase to preferentially "wet" the surface from the inside [32, 47]. Together with symmetry conditions, $F(0,t) = 0$ and $\frac{\partial c}{\partial R}(0,t) = 0$, we have the required four boundary conditions, plus the current-voltage relation, to close the problem.

3.3.2 Dimensionless equations

To nondimensionalize the system, we will use several basic references to scale the model, which include the particle radius R_p for the length scale, the diffusion time $\frac{R_p^2}{D_0}$ for the time scale, the maximum ion concentration c_m for the concentration scale and the thermal energy k_BT for any energy scale. The dimensionless variables are summarized in Table 3.1.

Table 3.1: Dimensionless variables in the CHR model.

$\tilde{c} = \frac{c}{c_m}$	$\tilde{t} = \frac{D_0}{R_p^2}t$	$\tilde{r} = \frac{r}{R_p}$	$\tilde{\nabla} = R_p\nabla$	$\tilde{F} = \frac{R_p}{c_m D_0}F$
$\tilde{\mu} = \frac{\mu}{k_BT}$	$\tilde{\Omega} = \frac{\Omega}{k_BT}$	$\tilde{\kappa} = \frac{\kappa}{R_p^2 c_m k_BT}$	$\tilde{I} = \frac{R_p}{c_m neD_0}I$	$\tilde{I}_0 = \frac{R_p}{c_m neD_0}I_0$
$\tilde{\eta} = \frac{e}{k_BT}\eta$	$\tilde{V} = \frac{eV}{k_BT}$	$\tilde{V}^\Theta = \frac{eV^\Theta}{k_BT}$	$\tilde{\gamma}_s = \frac{\gamma_s}{R_p c_m k_BT}$	$\beta = \frac{1}{\tilde{\kappa}}\frac{\partial\tilde{\gamma}_s}{\partial\tilde{c}}$

With these definitions, our model takes the dimensionless form,

$$\frac{\partial\tilde{c}}{\partial\tilde{t}} = -\frac{1}{\tilde{r}^2}\frac{\partial}{\partial\tilde{r}}\left(\tilde{r}^2\tilde{F}\right) \tag{3.13}$$

$$\tilde{F} = -(1-\tilde{c})\tilde{c}\frac{\partial\tilde{\mu}}{\partial\tilde{r}} \tag{3.14}$$

$$\tilde{\mu} = \ln\frac{\tilde{c}}{1-\tilde{c}} + \tilde{\Omega}(1-2\tilde{c}) - \tilde{\kappa}\tilde{\nabla}^2\tilde{c} \tag{3.15}$$

$$\frac{\partial\tilde{c}}{\partial\tilde{r}}(0,\tilde{t}) = 0, \quad \frac{\partial\tilde{c}}{\partial\tilde{r}}(1,\tilde{t}) = \beta \tag{3.16}$$

$$\tilde{F}(0,\tilde{t}) = 0, \quad \tilde{F}(1,\tilde{t}) = I. \tag{3.17}$$

In order to relate the current to the battery voltage, we assume generalized Butler-

Volmer kinetics [15],

$$\tilde{I} = \tilde{I}_0 \left(e^{-\alpha\tilde{\eta}} - e^{(1-\alpha)\tilde{\eta}} \right) \tag{3.18}$$

$$\tilde{\eta} = \tilde{\mu} + \tilde{V} - \tilde{V}^{\Theta} \tag{3.19}$$

$$\tilde{I}_0 = \tilde{c}^{\alpha}(1-\tilde{c})^{1-\alpha} e^{\alpha(\tilde{\Omega}(1-2\tilde{c})-\tilde{\kappa}\nabla^2\tilde{c})} = (1-\tilde{c})e^{\alpha\tilde{\mu}} \tag{3.20}$$

where I is the insertion current density (per area), I_0 the exchange current density, α the charge transfer coefficient, η the surface or activation overpotential, V the battery voltage, and V^{Θ} the reference voltage for a given anode (e.g. Li metal) when the particle is homogeneous at $\tilde{c} = \frac{1}{2}$. The derivation of this rate formula assumes that the transition state for charge transfer excludes one surface site, has no enthalpic excess energy, and has an electrostatic energy $(1-\alpha)$ times that of the electron plus the ion in the electrolyte. It is common to assume $\alpha = \frac{1}{2}$, but we will relax this assumption below. In equilibrium, $\eta = 0$, the interfacial voltage, $\Delta V = V - V^{\Theta}$ is determined by the Nernst equation, $\Delta\tilde{V}_{eq} = -\tilde{\mu}$. Out of equilibrium, the overpotential, $\eta(t) = \Delta V(t) - \Delta V_{eq}(t)$, is determined by solving for the transient concentration profile.

3.3.3 Governing parameters

Dimensionless groups are widely used in fluid mechanics to characterize dynamical regimes [14], and recently the same principles have been applied to intercalation dynamics in Li-ion batteries [188, 74]. The CHR model is governed by four dimensionless groups, $\tilde{\Omega}$, $\tilde{\kappa}$, β and $\tilde{I}$ (or $\tilde{V}$) with the following physical interpretations.

The ratio of the regular solution parameter (enthalpy of mixing) to the thermal energy can be positive or negative, but in the former case (attractive forces) it can be interpreted as

$$\tilde{\Omega} = \frac{\Omega}{k_B T} = \frac{2T_c}{T}, \tag{3.21}$$

i.e. twice the ratio of the critical temperature $T_c = \frac{\Omega}{2k_B}$, below which phase separation is favored, to the temperature T. Below the critical point, $T < T_c$ (or $\tilde{\Omega} > 2$), the

thickness and interfacial tension of the diffuse phase boundary scale as $\lambda_b = \sqrt{\kappa/c_m\Omega}$ and $\gamma_b = \sqrt{\kappa\Omega c_m}$, respectively [33], so the dimensionless gradient penalty

$$\tilde{\kappa} = \frac{\kappa}{c_m k_B T R_p^2} = \tilde{\Omega}\left(\frac{\lambda_b}{R_p}\right)^2 \ll 1 \tag{3.22}$$

equals $\tilde{\Omega}$ times the squared ratio of the interfacial width (between high- and low-density stable phases) to the particle radius, which is typically small.

The parameter β is the dimensionless concentration gradient at the particle surface, $\beta = \frac{1}{\tilde{\kappa}}\frac{\partial\tilde{\gamma}_s}{\partial\tilde{c}}$, which we set to a constant, assuming that the surface tension $\gamma_s(c)$ is a linear function of composition. Letting $\Delta\gamma_s = \frac{\partial\gamma_s}{\partial\tilde{c}}$ be the difference in surface tension between high-density ($\tilde{c} \approx 1$) and low-density ($\tilde{c} \approx 1$) phases,

$$\beta = \frac{R_p}{\lambda_b}\frac{\Delta\gamma_s}{\gamma_b} \gg 1 \tag{3.23}$$

we can interpret β as the ratio of particle size to the phase boundary thickness times the surface-to-bulk phase boundary tension ratio, $\frac{\Delta\gamma_s}{\gamma_b}$. In cases of partial "wetting" of the surface by the two solid phases, this ratio is related to the equilibrium contact angle θ by Young's Law,

$$\cos\theta = \frac{\Delta\gamma_s}{\gamma_b}. \tag{3.24}$$

Partial wetting may occur in the absence of elastic strain (as we assume below), but complete wetting by the lower-surface-energy phase is typically favored for coherent phase separation because $\gamma_b \ll |\Delta\gamma_s|$ [47]. In any case, for thin phase boundaries, we typically have $\beta \gg 1$.

Finally, the current density is scaled to the diffusion current,

$$\tilde{I} = \frac{I}{3nec_m V/(\tau_D A)} = \frac{R_p}{nec_m D_0} I, \tag{3.25}$$

where $V = \frac{4}{3}\pi R^3$ is the volume of the sphere, $nec_m V$ represents the maximum charge can be stored in the sphere, $A = 4\pi R_p^2$ is the surface area and $\tau_D = R_p^2/D_0$ is the diffusion time into the particle. $\tilde{I} = 1$ is equivalent to that the particle can be

fully charged from empty in $\frac{1}{3}$ unit of diffusion time τ_D with this current density. The exchange current has the same scaling. Rate limitation by surface reactions or by bulk diffusion corresponds to the limits $\tilde{I}_0 \ll 1$ or $\tilde{I}_0 \gg 1$, respectively, so this parameter behaves like a Damkoller number [188, 74].

3.3.4 Simulation details

For a given dynamical situation, either the current or the voltage is controlled, and the other quantity is predicted by the model. Here we consider the typical situation of "galvanostatic" discharge/charge cycles at constant current, so the model predicts the voltage V, which has the dimensionless form, $\tilde{V} = \frac{neV}{k_B T}$. The electrochemical response is typically plotted as voltage versus state of charge, or mean filling fraction,

$$X = \frac{\int c\, dV}{\frac{4}{3}\pi R_p^3 c_m}. \tag{3.26}$$

The reference scale for all potentials is the thermal voltage, $\frac{k_B T}{e}$, equal to 26 mV at room temperature.

In the following sections, we perform numerical simulations for the parameter settings in Table 3.2, which have been fitted to experimental data for LFP [8, 48], but we vary $\tilde{\Omega}$ to obtain different dynamical behaviors, which may represent other Li-ion battery materials. Owing to its small size, $R_p = 100$ nm, and relatively fast solid diffusion, the particle is strongly reaction limited, since $\tilde{I}_0 = 0.0226$, allowing us to focus on the novel coupling of reaction kinetics with phase separation [15]. In this exercise, we initially neglect surface wetting (by setting $\beta = 0$) and coherency strain, both of which are important for an accurate description of LFP [48, 47]. In later sections, we also consider $\beta > 0$ and $\alpha \neq \frac{1}{2}$ for the more interesting cases of phase separation ($\tilde{\Omega} > 2$). We employ a control volume method (described below) for the spatial discretization of the system and the ode15s solver in MATLAB for the time integration.

Table 3.2: Parameter settings for LFP used in the numerical simulations, except as otherwise noted.

Parameter	Value	Unit	Parameter	Value	Unit
R_p	1×10^{-7}	m	Ω	0.115	eV
κ	3.13×10^{9}	eV/m	D_0	1×10^{-12}	m^2/s
$c(r,0)$	10	mol / m^3	c_m	1.379×10^{28}	m^-3
n	1	-	α	0.5	-
V^{Θ}	3.42	V	I_0	500	A/m^2

3.4 Solid Solution

Our model predicts simple diffusive dynamics with slowly varying concentration and voltage transients under "solid solution" conditions, where configurational entropy promotes strong mixing. The regular solution model predicts that bulk solid solution behavior occurs at all temperature if there are repulsive forces between intercalated ions, $\Omega < 0$, or above the critical temperature $T > T_c$ for attractive ion-ion forces, $\Omega > 0$. Here, we consider finite-sized particles and examine current-voltage transients in both of these cases of solid-solution thermodynamics.

3.4.1 Repulsive forces

A negative enthalpy of mixing, $\Omega < 0$, reflects mean-field attraction between ions and vacancies, or equivalently, repulsion between intercalated ions that promotes homogeneous intercalation. Consider galvanostatic (constant current) charge and discharge cycles with $\Omega = -0.0514$eV or $\tilde{\Omega} = -2$. When the current is small, $\tilde{I} \ll 1$, diffusion is fast, and the ions remain uniformly distributed inside the particle during intercalation dynamics, as shown in Fig. 3-1. At high currents, $\tilde{I} \gg 1$ (not considered here), diffusion becomes rate limiting, and concentration gradients form, as in prior models of spherical nonlinear diffusion [67, 191, 239].

Given the Butler-Volmer symmetry factor, $\alpha = 0.5$, and assuming uniform composition, the total voltage drop between anode and particle surface is given by

$$\tilde{V} = \tilde{V}^{\Theta} - \tilde{\mu}(\tilde{c}) - 2\sinh^{-1}\left(\frac{\tilde{I}}{2\tilde{I}_0(\tilde{c})}\right), \tag{3.27}$$

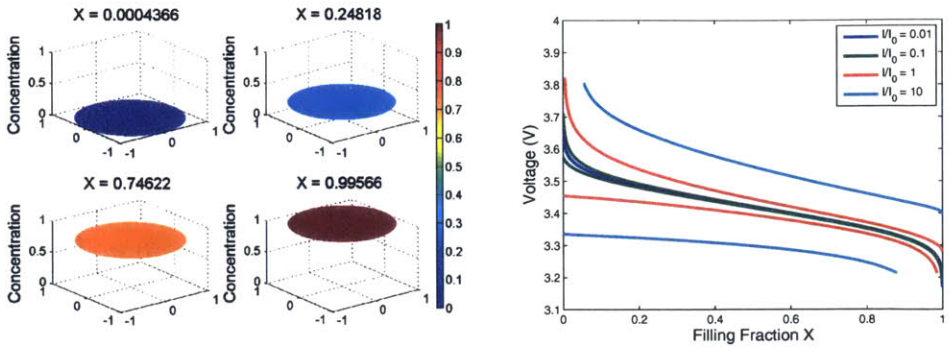

Figure 3-1: Constant current cycling of a spherical intercalation particle, composed of a solid solution of lithium ions with repulsive forces ($\tilde{\Omega} = -2$). Left: profiles of dimensionless concentration $\tilde{c}(\tilde{r})$ (local filling fraction) at different mean compositions (average filling fraction, X) at nondimensional current $i/I_0 = 0.25$. The vertical dimension in the plots shows the concentrations, while the horizontal circle denotes the hyperplane cut at the equator of the sphere. Right: voltage versus state of charge (filling fraction) at different currents. The reference current density $I_0 = 500\ A/m^2$ is the exchange current density when particle is uniformly half filled. The eight voltage curves represent $I/I_0 = \pm 0.01, \pm 0.1, \pm 1, \pm 10$.

where V is the battery voltage, $V^{\ominus}$ is the constant reference voltage for a given anode, and $\tilde{I}_0(\tilde{c})$ the exchange current density at the given concentration profile. The simulated discharge curves in Fig. 3-1 fit this expression well and exhibit no voltage plateau (a signature of phase separation discussed below). The model exhibits a positive internal resistance, since the battery voltage decreases for $I > 0$ (discharging) and increases for $I < 0$ (charging). According to Eq. (3.27), the voltage increment, or overpotential, has two sources: concentration changes at the surface that shift the Nernst equilibrium interfacial voltage (second term, concentration overpotential) and Butler-Volmer charge-transfer resistance (third term, activation overpotential).

3.4.2 Weak attractive forces or high temperature

When the mixing enthalpy per site Ω is positive, there is an effective repulsion between ions and vacancies, or equivalently, an attraction between ions that promotes phase separation into Li-rich and Li-poor phases. This tendency counteracted by configurational entropy, which always promotes the mixing of ions and vacancies and leads to homogeneous solid solution behavior at high temperature T. Below the crit-

ical temperature, $T < T_c = \frac{\Omega}{2k_B}$, attractive forces overcome configurational entropy, leading to stable bulk phase separation.

For $T > T_c$, the numerical results are consistent solid solution behavior. For example, we use the same parameters in Table 3.2, except for the $\Omega = 2.57 \times 10^{-2}$ eV, or $\tilde{\Omega} = 1$, so the absolute temperature is twice the critical value, $T/T_c = 2$. As shown in Fig. 3-2, the voltage varies less strongly with filling fraction, in a way that resembles previous empirical fits of the flat voltage plateau (below) signifying phase separation. There is no phase separation, however, and the concentration profile (not shown) is very similar to the case of repulsive interactions in Fig. 3-1.

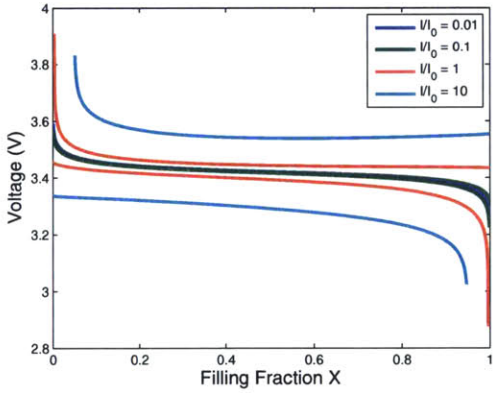

Figure 3-2: Cycling of a high temperature solid solution with attractive forces ($\tilde{\Omega} = 1$) with other parameters from Fig. 3-1.

3.4.3 Capacity

When the particle is charged or discharged at a high rate, the total capacity, defined as the mean filling X reached when the voltage drops below some threshold on discharge, will be significantly reduced. In a simple spherical diffusion model, by the scaling of Sand's time $t_s \sim \frac{1}{I^2}$ [13, 17] and charge conservation, the total capacity C scales as, $C = It_s \sim I^{-1}$. In our CHR model, we observe a different scaling of the capacity from the numerical simulations. In a simple power law expression, $C \sim I^{\gamma}$, the exponent γ depends on different conditions, such as wetting parameter β, gradient penalty constant κ, and regular solution parameter Ω. A sample of the scaling dependence

on current with different κ is shown in Fig. 3-3, where $p \approx 0.5$.

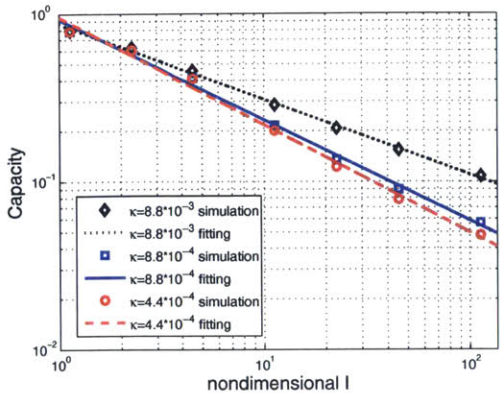

Figure 3-3: Capacity C versus current with different gradient penalty constant κ in a solid solution ($\tilde{\Omega} = \beta = 0$).

3.5 Phase Separation

In some materials, such as LFP, the attractive forces between intercalated ions are strong enough to drive phase separation into Li-rich and Li-poor solid phases at room temperature, for $T < T_c$, or $\tilde{\Omega} > 2$ in the regular solution model. Phase separation occurs because the homogeneous chemical potential is no longer a monotonic function of concentration. This has a profound effect on battery modeling that is predicted from first principles by the CHR model.

3.5.1 Strong attractive forces or low temperature

In order to simulate a representative model, we again use the parameters in Table 3.2 but set the $\Omega = 1.15 \times 10^{-1}$ eV, or $\tilde{\Omega} = 4.48 > 2$, which is a realistic value of the enthalpy per site value in LFP [48]. Very different from the uniformly filling behavior in Fig. 3-1, phase separation occurs suddenly when the composition passes the linearly unstable spinodal points. The concentration profiles develop sharp boundaries between regions of uniform composition corresponding to the two stable phases, as shown in Fig. 3-4. The new phase appears at the surface and propagates inward, as

shown in Fig. 3-5, once the surface concentration enters the unstable region of the phase diagram.

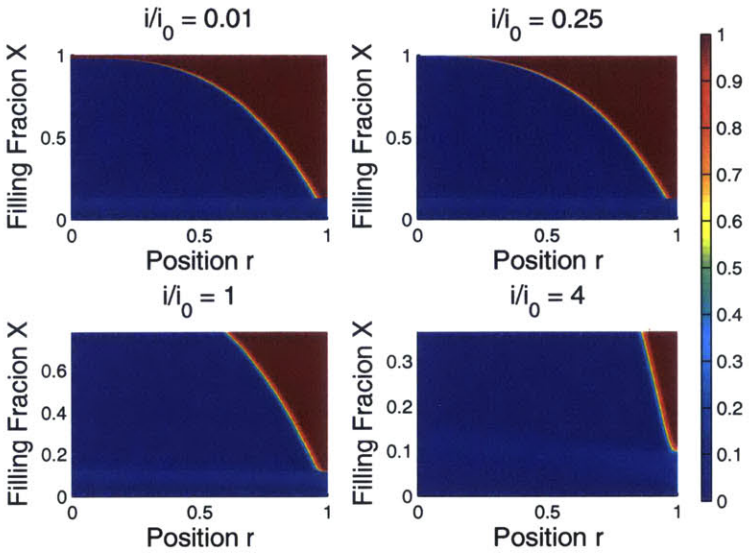

Figure 3-4: Dynamics of phase separation during ion intercalation ($\tilde{\Omega} = 4.48$). Concentration distributions within the spherical particle are shown at different currents $\frac{i}{i_0} = 0.01$ (top left), 0.25 (top right), 1 (bottom left) and 4 (bottom right), where $I_0(\tilde{c} = 0.5) = 500$ A/m^2. The x-axis represents the nondimensional radial position $\tilde{r}$ and the y-axis presents the overall average filling fraction X of the whole particle, which can be also seen as the time dimension. The warmer color in the figure indicates a higher local filling fraction.

After phase separation occurs, the CHR model for an isotropic spherical particle predicts similar must account for t as the shrinking core model, but without empirical placing a sharp phase boundary. Instead, the diffuse phase boundary appears from an initial single-phase solid solution at just the right moment, determined by thermodynamic principles, and there is no need to solve a moving boundary problem for a sharp interface, which is numerically simpler.

The CHR model also predicts the subtle electrochemical signatures of phase separation dynamics [15]. Without any empirical fitting, phase separation naturally leads to a flat voltage plateau, as shown in Fig. 3-6. The constant-voltage plateau reflects from the constant chemical potential of ion intercalation in a moving phase boundary (in the absence of coherency strain, which tilts the plateau [48]). At high currents,

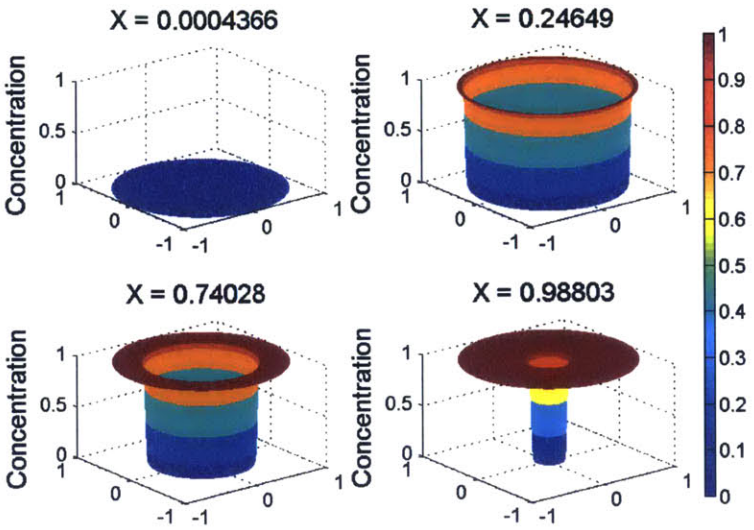

Figure 3-5: Shrinking core dynamics of phase separation in an isotropic spherical particle ($\tilde{\Omega} = 4.48$ and no surface wetting). The vertical dimension in the plots shows the concentrations, while the horizontal circle denotes the hyperplane cut at the equator of the sphere. The nondimensional current is $I/I_0 = 0.25$ with $I_0(\tilde{c} = 0.5) = 500$ A/m^2 and X the overall filling fraction of lithium ions.

the initial charge transfer resistance, or activation overpotential, is larger, as signified by the jump to the plateau voltage (derived below), and over time, solid diffusion limitation, or concentration overpotential, causes the voltage to fall more rapidly during discharging, or increase during charging.

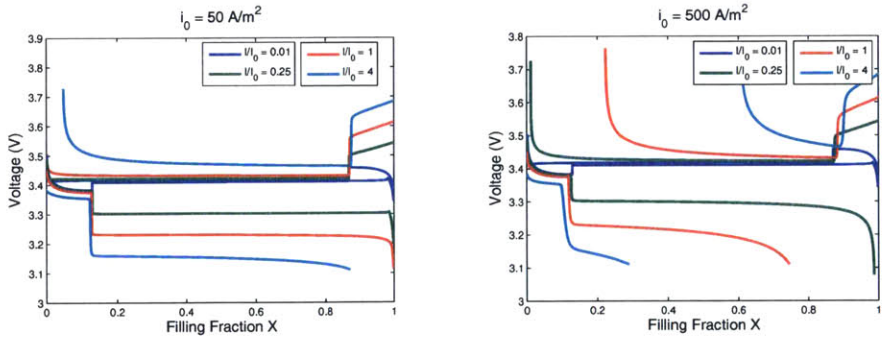

Figure 3-6: Phase separating particle ($\tilde{\Omega} = 4.48$) voltage vs. filling fraction plot with different currents and two different reference exchange currents. Both the charging and discharging curves are shown. The reference current density i_0 is the exchange current density which takes values 50 A/m^2 (left) and 500 A/m^2 (right) when particle is uniformly half filled.

3.5.2 Voltage Plateau Estimation

As we see from Fig. 3-4-3-6, our model system always undergoes phase separation, which leads to a voltage plateau. In the case without surface wetting, i.e. $\beta = 0$, we can derive an accurate approximation of the voltage plateau valued, since the concentration within each phase is relatively uniform, especially when the current is not very large. Therefore, we may ignore the gradient penalty term $\kappa\nabla^2 c$, leaving only the homogeneous chemical potential,

$$\tilde{\mu} \approx \ln \frac{\tilde{c}}{1-\tilde{c}} + \tilde{\Omega}(1-2\tilde{c}). \tag{3.28}$$

The stable composition of each phase is approximately solves $\tilde{\mu} = 0$, where the homogeneous free energy at these two concentrations takes its minimum. During ion insertion, the surface concentration is approximately the larger solution $\tilde{c}_l$ of this equation. In the case $I > 0$, given the nondimensional current - exchange current ratio $\hat{I} = \frac{\tilde{I}}{\tilde{I}_0(\tilde{c}=\frac{1}{2})}$, where $\tilde{I}_0(\tilde{c} = \frac{1}{2})$ is the exchange current when the concentration $\tilde{c} = \frac{1}{2}$ throughout the whole particle. The plateau voltage is then given by

$$V \approx V^{\Theta} - \frac{2k_B T}{e} \sinh^{-1}\left(\frac{\hat{I}}{4(1-\tilde{c}_l)}\right). \tag{3.29}$$

At low currents, the agreement between this analytical approximation and the numerically determined voltage plateau is excellent, as shown in 3-7.

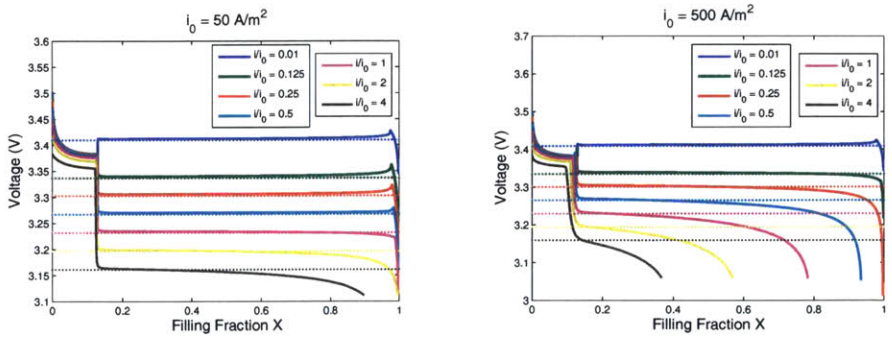

Figure 3-7: Comparison of the simulated voltage plateau from Fig. 3-6 (solid curves) and the analytical approximation of Eq. (3.29) (dashed curves) for $I > 0$.

The voltage plateau formula can be understood physically as follows. As a result of our assumption of spherical symmetry, the intercalation reaction must proceed into the outer "shell phase". In the case of lithiation, the shell has high concentration and thus strong entropic constraints inhibiting further insertion that lower the reaction rate, increase the overpotential, and lower the voltage plateau when phase separation occurs. In contrast, when the phase boundary is allowed to move along the surface as an intercalation wave [188, 8, 48, 47], insertion occurs with higher exchange current at intermediate concentrations, although the active area is reduced, which leads to suppression of surface phase separation at high currents [8, 48].

3.5.3 Butler-Volmer Transfer Coefficient

In the preceding examples, we set the Butler-Volmer the transfer coefficient to $\alpha = 0.5$ as in prior work with both CHR [8, 48] and diffusive [67, 191] models. This choice can be justified by Marcus theory of charge transfer when the reorganization energy is much larger than the thermal voltage [15, 13], but in battery materials this may not always be the case. In our isotropic model, charge-transfer asymmetry ($\alpha \neq 0.5$) mainly manifests itself via strong broken symmetry between charge and discharge in the activation overpotential, as shown in the voltage plots of Fig. 3-8. A smaller value of α leads to a lower voltage plateau while discharging ($I > 0$), but does not much affect the voltage plateau during charging ($I < 0$).

3.6 Phase Separation with Surface Wetting

The wetting of a solid surface by two immiscible fluids, such as water and air, is very familiar, but it is not widely appreciated that analogous phenomena also occur when binary solids "wet" a fluid or solid surface and play a major role in nanoparticle intercalation [47]. The only major difference is that coherent (defect-free) solid-solid interfaces have much lower tension than solid-fluid interfaces due to stretched, rather than broken, bonds. As a result, a stable contact angle cannot form, and one phase tends to fully wet each surface in equilibrium ($\Theta_c = 0, \pi$), regardless of the bulk

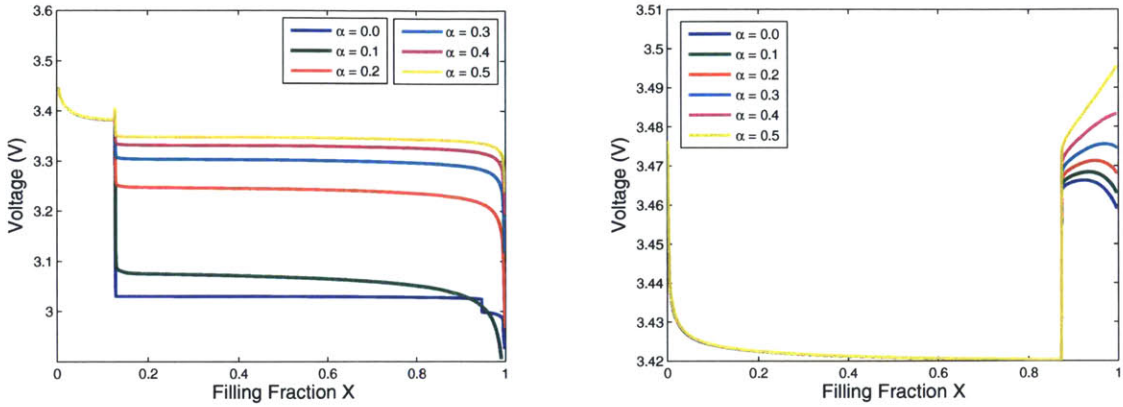

Figure 3-8: Effect of the Butler-Volmer charge transfer symmetry coefficient α on the voltage during battery discharging (left) and charging (right) with $|I/I_0| = 0.1$ and $I_0 = 500$ A/m^2 at half filling.

composition. The competition between different phases to wet a surface can promote the nucleation of a phase transformation via the instability of a surface wetting layer. In particular, the wetting of certain crystal facets of LFP particles by either $LiFePO_4$ and $FePO_4$ ensures the existence of surface layers that can become unstable and propagate into the bulk, as a means of surface-assisted nucleation [47].

3.6.1 Shrinking cores and expanding shells.

In this section, we show that surface wetting characteristics have a significant effect on the concentration profile and voltage during insertion, even in an isotropic spherical particle. Mathematically, we impose the inhomogeneous Neumann boundary condition, $\frac{\partial \tilde{c}}{\partial \tilde{r}}(1, \tilde{t}) = \beta$, where, as described above, $\beta > 0$ promotes the accumulation of ions at the surface, or wetting by the high density phase. In this case, during ion insertion, the surface concentration will be always higher than the remaining bulk region, if we start from a uniform low concentration. As a result, the surface hits the spinodal point earlier than other places inside the particle, which means the Li-rich phase always nucleates at the surface. In an isotropic particle, this leads to the shrinking core phenomenon, as in the cases without surface wetting ($\beta = 0$) described above.

The case of surface de-wetting ($\beta < 0$) is interesting because surface nucleation is suppressed, and more than two phase regions can appear inside the particle. During insertion, the surface concentration is now always lower than in the interior, especially when the current is small. Therefore, an interior point will reach the spinodal concentration earlier than the surface, so the high-density phase effectively nucleates somewhere in the bulk, away from the surface.

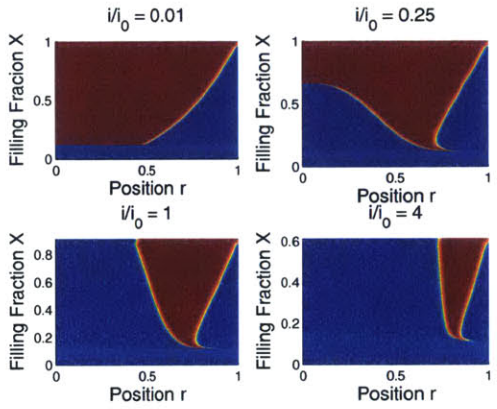

Figure 3-9: Phase boundary motion during ion insertion in a spherical particle with surface de-wetting ($\beta = -17.9$, $\Omega = 4.48$) at different currents $\frac{i}{i_0} = 0.01$ (top left), 0.25 (top right), 1 (bottom left) and 4 (bottom right)a nd $I_0 = 500$ A/m^2 at half filling. The warmer color in the figure indicates a higher local filling fraction.

As a result, there is an "expanding shell" at the same time as a shrinking core of the low density phase. This unusual behavior is shown in Fig. 3-9 for $\beta = -17.9$ at several currents. The surface energy is $\gamma = -90$ mJ/m^2 at maximum filing, if we assume the γ is a linear function of concentration. A detailed demonstration of this concentration dynamics is shown in Fig. 3-10. The middle Li-rich region expands inward and outward simultaneously, it first fills up the Li-poor phase located at the center, and finally it fills the whole particle.

Since the surface is always in the lower stable concentration after the initial phase separation, which does not vary according to the surface derivative β, we should expect the voltage has very weak dependence on the surface de-wetting condition. The voltage - filling fraction plot in Fig. 3-11 confirms this intuition. When $I < 0$, the strong surface de-wetting will make the surface concentration very closed to zero,

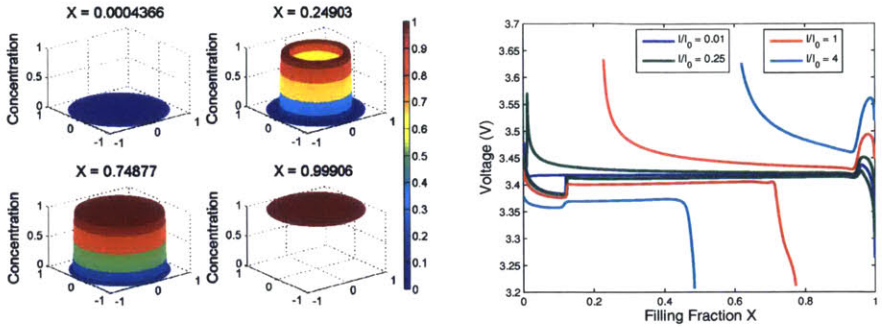

Figure 3-10: Concentration profiles (left) and voltage transients (right) for ion insertion at currents $i/i_0 = \pm 0.01, \pm 0.25, \pm 1$ and ± 4 in a phase separating spherical particle ($\tilde{\Omega} = 4.48$ and surface de-wetting $\beta = -17.9$).

which will make the chemical potential extremely sensitive to small perturbation in concentration, therefore, we only show the results with relatively weak surface de-wetting ($\beta \geq -10$).

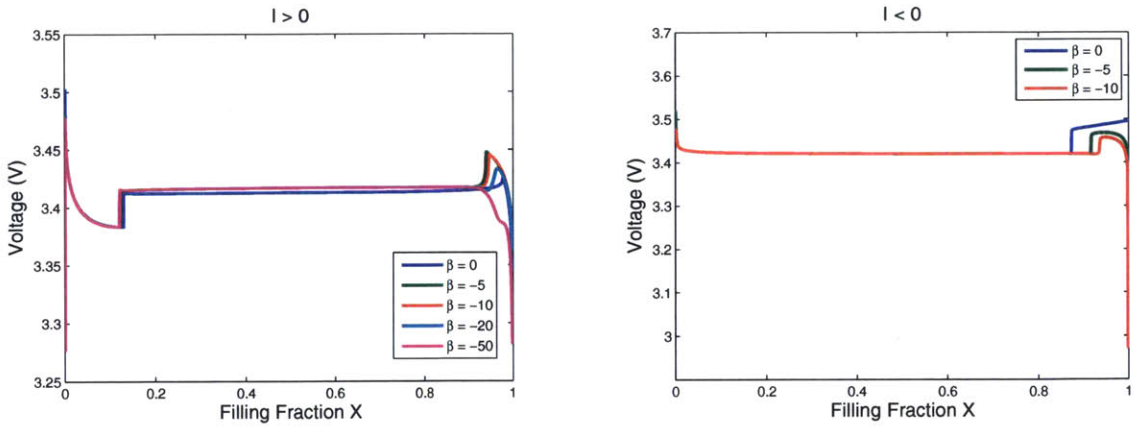

Figure 3-11: Effect of a negative surface wetting parameter ($\beta < 0$) on the voltage during discharging at $I/I_0 = 0.01$ (left) and charging at $I/I_0 = -0.01$.

3.6.2 Voltage efficiency

In the limit of zero current at a given filling, the voltage given by the Nernst equation has a unique value $V(X)$ corresponding to thermodynamic equilibrium. When a current is applied, energy is lost as heat due to various resistances in the cell, and there is a voltage gap ΔV between charge and discharge at the same filling. The voltage

efficiency is $1 - \Delta V/V_0$. To account for transient effects, we define the voltage gap for a given current magnitude $|I|$ as the voltage at half filling ($X = 0.5$) during galvanostatic charging starting from nearly full with $I < 0$, minus that during discharging starting from nearly empty with $I > 0$.

In Fig. 3-12, we show how different parameters, such as the current, mixing enthalpy, and surface wetting condition affect the voltage gap. For our single particle model with surface nucleation, the voltage gap vanishes at zero current, in contrast to experiments [69] and simulations [68, 74] on porous multi-particle electrodes. There is no contradiction, however, because the zero-current voltage gap is an emergent property of a collection of particles with two stable states, resulting from the mosaic instability of discrete transformations (which can also been seen in an array of balloons [68]).

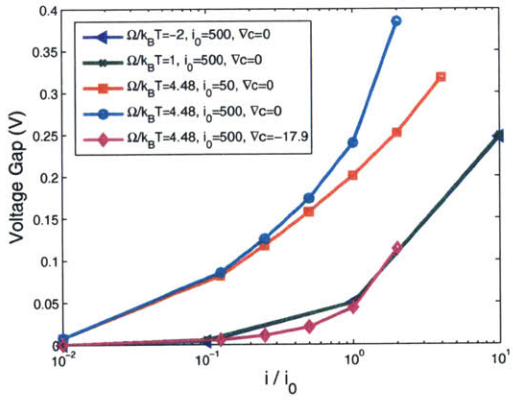

Figure 3-12: The gap of the charging and the discharging voltage when the particle is half filled, $X = 0.5$, under several conditions including current, $\tilde{\Omega}$ and surface wetting. The ∇c shown in the legend is the nondimensional concentration derivative at the particle surface, which denotes the surface wetting condition.

In the case without surface wetting (β), the voltage gap is smaller for solid solutions ($\tilde{\Omega} < 2$) than for phase separating systems ($\tilde{\Omega} > 2$), since it is more difficult to insert ions into the full stable state than into an intermediate concentration. With strong surface de-wetting by the ions ($\beta < 0$) and phase separation ($\tilde{\Omega} > 2$), however, the gap can be even smaller than in the solid solution case without surface wetting, because the persistence of the low density phase promotes easy intercalation. This

is an important observation because it shows the possibility of improving the voltage efficiency by engineering the solid-solid contact angle of the active particles.

3.7 Numerical Methods and Error Convergence

The CHR model is fourth-order in space and highly nonlinear and thus requires care to solve numerically with accuracy and efficiency. Naive finite difference or finite volume methods would be unstable or inaccurate. In order to obtain the solutions above, we developed a new conservative numerical scheme to solve the CHR model with second-order accurate discretization, described in this section.

3.7.1 Numerical Scheme

Great effort has been devoted for solving the Cahn-Hilliard equation numerically with different boundary conditions, and several numerical schemes have been employed, e.g. finite difference [44, 56, 187], finite element [11, 244, 227], spectral method [91], boundary integral [57], level set [84], discontinuous Galerkin [230] and multi-grid methods [113, 226].

As our problem is associated with the flux boundary condition, the finite volume method is a more convenient and suitable choice for discretization [30, 49, 54]. Furthermore, the finite volume method may be superior to other methods by its perfect mass conservation and the capability for capturing the concentration shock during phase separations.

The finite volume method handles the integral form of the Cahn-Hilliard equation. Using the divergence theorem we may update the change of average concentration within a small volume by calculating the difference of the inward flux and the outward over the corresponding volume boundary. In the recent literature, two basic approaches for estimating the concentrations and their derivatives at the boundary have been developed.

Burch [30] uses the finite difference type technique to extrapolate the desired unknown values with the known average concentration in each control volume. This ap-

proximation method is highly efficient in low dimensional cases with a well-structured grid. Cueto-Felgueroso and Peraire [49], Dargaville and Farrell [54] develop a different least squares based technique, which is more suitable for high dimensions cases with a un-structured grid. They use the concentrations and their partial derivatives on the control volume boundaries to predict the centroid concentrations nearby, and find the "most probable" boundary values (concentrations and derivatives) by least square minimizing the prediction errors in centroid concentrations.

However, as in the model we are mostly focusing on the activities exactly on the particle surface, the finite volume method can only provide us information about the average concentration in the shell closed to the surface. It may take additional computation cost to extrapolate the surface condition and this will introduce additional error as well.

In order to avoid such extrapolation, we propose a numerical scheme that can immediately provide information on the particle surface and still keep the benefits of the finite volume method in conservation and shock toleration, which is inspired by our numerical method for solving the 1D nonlinear spherical diffusion problem [239]. Similar to the finite volume method, our numerical scheme indeed handles the integral form of the original PDE system. We work with dimensionless variables, but drop the tilde accents for ease of notation. Since the phase boundary may propagate to any location in the sphere, a non-uniform mesh may not be as helpful as the case in normal nonlinear diffusion problem, so we use uniform grids.

Consider a N-point uniform mesh within the sphere, x_1, x_2, x_3, $\cdots$, x_N, while $x_1 = 0$ is the sphere center and x_N is right on the surface. Here we define that $\Delta x = x_{j+1} - x_j$, for any $j \in \{1, 2, \cdots, N-1\}$ and make c_1, c_2, c_3, $\cdots$, c_N to be the concentration on these grid points.

If we integrate the Eqn. 3.13 over a shell centered at a non-boundary grid point x_i with width Δx, which is equivalent to the volume V_i between $[x_i - \frac{\Delta x}{2}, x_i + \frac{\Delta x}{2}]$, by divergence theorem we have,

$$\int_{V_i} \frac{\partial c}{\partial t} dV = -\int_{V_i} \nabla \cdot F dV = -\int_{\partial V_i} n \cdot F dS. \tag{3.30}$$

We can further write both sides of the above equation in the following form,

$$\int_{x_i-\frac{\Delta x}{2}}^{x_i+\frac{\Delta x}{2}} 4\pi x^2 \frac{\partial c}{\partial t} dx = 4\pi((x_i - \frac{\Delta x}{2})^2 F_{i-\frac{1}{2}} - (x_i + \frac{\Delta x}{2})^2 F_{i+\frac{1}{2}}). \tag{3.31}$$

while $F_{i-\frac{1}{2}} = F\Big|_{x_i-\frac{\Delta x}{2}}$ and $F_{i+\frac{1}{2}} = F\Big|_{x_i+\frac{\Delta x}{2}}$.

The left hand side of the above Eqn. 3.31 can be approximated by,

$$\int_{x_i-\frac{\Delta x}{2}}^{x_i+\frac{\Delta x}{2}} 4\pi x^2 \frac{\partial c}{\partial t} dx = \frac{\partial}{\partial t}(\frac{1}{8}V_{i-1}c_{i-1} + \frac{3}{4}V_i c_i + \frac{1}{8}V_{i+1}c_{i+1} + O(\Delta x^3)). \tag{3.32}$$

This can be also written in a matrix form for each small volume on each row,

$$\begin{pmatrix} \int_{x_1}^{x_1+\frac{\Delta x}{2}} 4\pi x^2 \frac{\partial c}{\partial t} dx \\ \int_{x_2-\frac{\Delta x}{2}}^{x_2+\frac{\Delta x}{2}} 4\pi x^2 \frac{\partial c}{\partial t} dx \\ \int_{x_3-\frac{\Delta x}{2}}^{x_3+\frac{\Delta x}{2}} 4\pi x^2 \frac{\partial c}{\partial t} dx \\ \vdots \\ \int_{x_{N-1}-\frac{\Delta x}{2}}^{x_{N-1}+\frac{\Delta x}{2}} 4\pi x^2 \frac{\partial c}{\partial t} dx \\ \int_{x_N-\frac{\Delta x}{2}}^{x_N} 4\pi x^2 \frac{\partial c}{\partial t} dx \end{pmatrix} \approx \mathbf{M}\frac{\partial}{\partial t}\begin{pmatrix} c_1 \\ c_2 \\ c_3 \\ \vdots \\ c_{N-1} \\ c_N. \end{pmatrix}, \tag{3.33}$$

while $\mathbf{M}$ is the mass matrix,

$$\mathbf{M} = \begin{pmatrix} \frac{3}{4}V_1 & \frac{1}{8}V_2 & 0 & 0 & \cdots & 0 & 0 & 0 \\ \frac{1}{4}V_1 & \frac{3}{4}V_2 & \frac{1}{8}V_3 & 0 & \cdots & 0 & 0 & 0 \\ 0 & \frac{1}{8}V_2 & \frac{3}{4}V_3 & \frac{1}{8}V_4 & \cdots & 0 & 0 & 0 \\ \vdots & \vdots & \vdots & \vdots & \ddots & \vdots & \vdots & \vdots \\ 0 & 0 & 0 & 0 & \cdots & \frac{1}{8}V_{N-2} & \frac{3}{4}V_{N-1} & \frac{1}{4}V_N \\ 0 & 0 & 0 & 0 & \cdots & 0 & \frac{1}{8}V_{N-1} & \frac{3}{4}V_N \end{pmatrix}. \tag{3.34}$$

In fact, this is the major alternation of our method from the classical finite difference method. Instead of having a diagonal mass matrix in the finite volume method, we hereby use a tri-diagonal mass matrix in our new numerical scheme. Since each column of the this matrix sum to the volume of the corresponding shell, this indicates

our method must conserve mass with a correct volume.

Before we approximate the flux F, we will give the approximation formula for the chemical potential μ_i at each grid point x_i. when $i = 2, 3, \cdots, N-1$,

$$\begin{aligned}\mu_i &= \ln\frac{c_i}{1-c_i} + \Omega(1-2c_i) - \kappa\nabla^2 c_i = \ln\frac{c_i}{1-c_i} + \Omega(1-2c_i) - \kappa(\frac{2}{x_i}\frac{\partial c}{\partial x} + \frac{\partial^2 c}{\partial x^2}) \\ &= \ln\frac{c_i}{1-c_i} + \Omega(1-2c_i) - \kappa(\frac{c_{i-1}-2x_i+c_{i+1}}{\Delta x^2} + \frac{2}{x_i}\frac{c_{i+1}-c_{i-1}}{2\Delta x}) + O(\Delta x^2).\end{aligned} \tag{3.35}$$

For $i = 1$, by symmetric condition at the center and the isotropic condition, $\nabla^2 c_1 = 3\frac{\partial^2 c_1}{\partial x^2}$ and $\nabla c_1 = 0$, then,

$$\mu_1 = \ln\frac{c_1}{1-c_1} + \Omega(1-2c_1) - 3\kappa\frac{\partial^2 c_1}{\partial x^2} = \ln\frac{c_1}{1-c_1} + \Omega(1-2c_1) - 3\kappa\frac{2c_2-2c_1}{\Delta x^2} + O(\Delta x^2). \tag{3.36}$$

For $i = N$, since we have the boundary condition $n\cdot\kappa\nabla c_N = \frac{\partial\gamma_s}{\partial c}$, when $\frac{\partial\gamma_s}{\partial c}$ is only a constant or a function of c_N, we can assume a ghost grid point at x_{N+1}, while the concentration at this point satisfies $\nabla c_N = \frac{c_{N+1}-c_{N-1}}{2\Delta x} = \beta$, which is equivalent to $c_{N+1} = 2\Delta x\beta + C_{N-1}$,

$$\mu_N = \ln\frac{c_N}{1-c_N} + \Omega(1-2c_N) - \kappa(\frac{2}{x_N}\beta + \frac{2C_{N-1}-2C_N+2\Delta x\beta}{\Delta x^2} + O(\Delta x^2)). \tag{3.37}$$

With the chemical potential on each grid point, we can estimate the right hand side of the Eqn. 3.31. For each midpoint of two grid points, the flux $F_{i+\frac{1}{2}}$ satisfies,

$$F_{i+\frac{1}{2}} = -(1-\frac{c_i+c_{i+1}}{2})\frac{c_i+c_{i+1}}{2}\frac{\mu_{i+1}-\mu_i}{\Delta x} + O(\Delta x^2). \tag{3.38}$$

For center of the sphere, again by the symmetric condition we have

$$F\Big|_{x=0} = 0. \tag{3.39}$$

And finally for the particle surface the flux is given by the current, which is also our boundary condition.

$$F\Big|_{x=1} = -F_s. \tag{3.40}$$

This finishes the discretization of the original partial differential equations system to a time dependent ordinary differential equations system. We use the implicit $ode15s$ solver for the time integration to get the numerical solution.

3.7.2 Error Convergence Order

As we demonstrated in the derivation of this numerical method, the discretization has no higher error than of the second order. Thus, we may expect the error convergence order in the spatial meshing should be also in the second order. This will be confirmed by the numerical convergence test.

In the error convergence test, we use small current density $i/i_0 = 10^{-4}$, while $i_0 = 500$ A/m^2, this setting is to eliminate the effect that the difference in ending simulation time. We will also assume no surface wetting in this test. As we are mostly interested in the voltage prediction from this single particle ion-intercalation model, we will define the error as the L^2 norm of the difference in voltage comparing to the standard curve, which will use the solution from very fine grid (3001 uniform grid points in our case) as the reference solution.

The plot of error convergence is shown in the left half of Fig. 3-13, which is consistent with our previous expectation. The absolute error in voltage shown in the right hand side in the same figure signifies that we will have trouble with oscillations after the phase separation if the grid is not fine enough.

As we see from Fig. 3-14, with 21 grid points, we may get different oscillation sizes in the solutions, which is sensitive to the parameter $\tilde{\Omega}$. While compares to the concentration distribution on the right, a larger parameter $\tilde{\Omega}$ leads to a smaller interfacial width, we need a fine enough grid which is with the grid size smaller than the interfacial width to capture the propagating shock without creating oscillations.

Therefore, in the choice of grid point number, we need to be careful about all conditions such as the radius, $\tilde{\Omega}$ and κ in order to get the desired accuracy with good stability, but without paying too much for the computation cost.

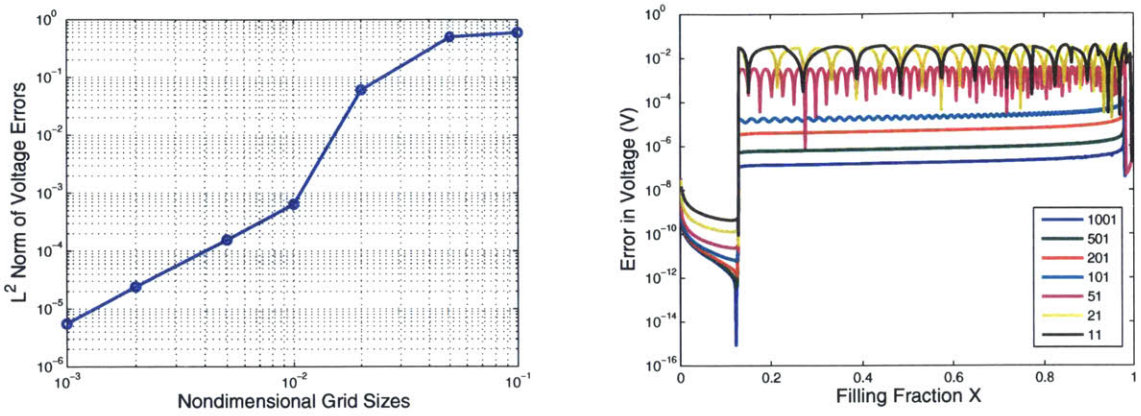

Figure 3-13: Error convergence test with the very small current density $i/i_0 = 10^{-4}$, while $i_0 = 500$ A/m^2 and no surface wetting is assumed. The error is defined as the l^2 norm of the voltage vector difference from the reference solution over the square root of length of this vector. The error converges in second order as suggested by the figure on the left. We also plot the error in voltage during ion intercalation of all these grid point cases (solution from 11 points to 1001 points compare to the reference solution from 3001 grids) in the right figure, where we observe oscillations when the grid is coarse.

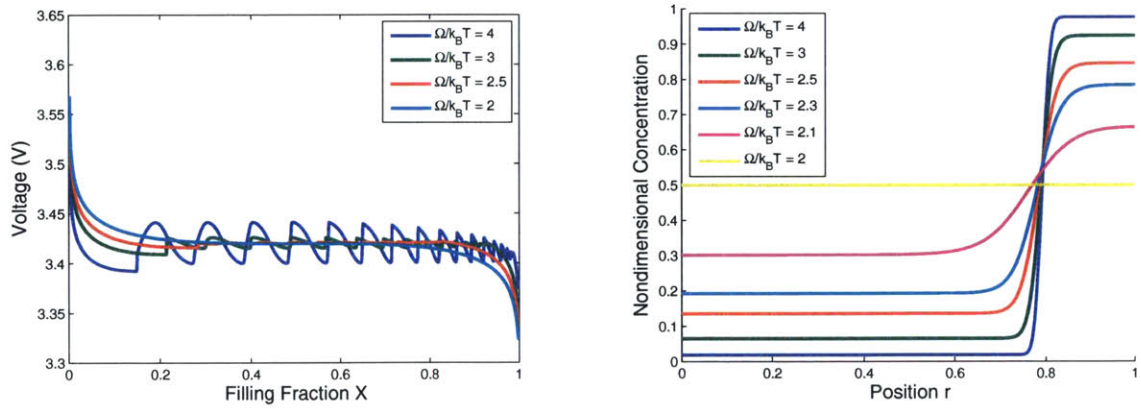

Figure 3-14: Voltage prediction plot with different $\tilde{\Omega}$ using 21 grid points on the left. We see more oscillations in larger $\tilde{\Omega}$. The right hand side is the concentration distribution with different $\tilde{\Omega}$ when the overall half filled. Higher $\tilde{\Omega}$ value indicates a thinner phase boundary thickness. The current density is set to be $i/i_0 = 10^{-4}$, while $i_0 = 500$ A/m^2 and no surface wetting is assumed in both of these simulations.

3.8 Conclusion

In summary, we have studied the dynamics of ion intercalation in an isotropic spherical battery intercalation particle using the heterogeneous CHR model with Butler-Volmer

reaction kinetics [15]. The model predicts either solid solution with radial nonlinear diffusion or core-shell phase separation, depending on the thermodynamic, geometrical, and electrochemical conditions. The model is able to consistently predict the transient voltage after a current step, regardless of the complexity of the dynamics, far from equilibrium. Surface wetting plays a major role in nucleating phase separation. The simplifying assumptions of radial symmetry and negligible coherency strain maybe be applicable to some materials, such as lithium titanate anodes or defective lithium iron phosphate cathodes, while the basic principles illustrated here have broad relevance for intercalation materials with complex thermodynamics and multiple stable phases.

Chapter 4

Two-Dimensional Cahn-Hilliard Reaction Model with Surface Electron-conducting Coating

4.1 Introduction

Surface modification of nanoparticles with a thin layer of carbon materials is one of the most important techniques for making high performance battery materials [175, 233, 127, 129, 167, 108, 73]. Such coatings not only can increase the electrical conductivity of the porous electrode [175, 105], but also prevent the nanoparticles from coarsening during high-temperature annealing [245]. Carbon coating is one of the most thoroughly studied surface modification methods, especially for lithium iron phosphate [175, 39, 65, 20, 66, 229, 235].

In electrochemical reactions, carbon coating provides the pathway of electrons, thus serving as an electron-donor or acceptor in reactions [168, 9]. The potential difference across the reaction interface enables such reactions, which would not be possible under pure chemical conditions [25]. It is easy to see that the properties of carbon coating will affect the lithium intercalation dynamics by limiting the electron supply. While making a high quality carbon coating on nanoparticles is still challeng-

ing, most mathematical models have assumed ideal electron conductivity and solely focused on the dynamics of lithium ions [220, 15].

Experimental results have revealed that the temperature of material annealing, usually around 700 degrees Celsius, cannot carbonize the precursor with good electrical conductivity [245]. Via an effective formula, assuming dilute solution and Ohm's law [86], the estimated diffusion coefficient of the electrons is of the same order as that of lithium in lithium iron phosphate (LFP). Furthermore, due to the low electrical conductivity of the carbon coating, nano-sized carbon black needs to be added for better connection with the current connector [220]. When working under high rate conditions, places far away from this contact point may not be able to get electrons to facilitate the intercalation of lithium ions, due to the transport limitation.

By coupling the transport process of electrons in the coating layer to the particle bulk Cahn-Hilliard reaction (CHR) kinetics, we establish a new mathematical model in this paper that takes account of both the particle bulk ion transport and the surface coating layer electron transport. This new model enables us to quantitatively analyze, for the first time, the surface coating effects at the battery dynamics on the thermodynamics level, as well as better interpret the "depth-average approximation" for the CHR models in the literature.

4.2 Model Description

4.2.1 General Cahn-Hilliard Reaction Model with Surface Coating

The lithium-ion intercalation dynamics is generally described by a generalized diffusion-reaction equation, which takes the form,

$$\frac{\partial c}{\partial t} = \nabla \cdot (Mc\nabla\mu) + R, \tag{4.1}$$

where c is the concentration of the lithium-ion, M the mobility, μ chemical potential of the ion, and R the volumetric reaction rate of lithium-ion. In this system, the

reaction rate R is non-zero only at the boundary of the particle, which is due to the nature of the intercalation process.

The mobility M of the ion can be related to a more well-accepted concept, the diffusivity in the dilute-solution limit D_0. By applying the Einstein relation, and the assumption that the transition state of ion diffusion within the particle will exclude two available sites for ions, we get,

$$M = \frac{D_0}{k_B T}\left(1 - \frac{c}{c_m}\right), \tag{4.2}$$

where k_B is the Boltzmann constant, T the temperature, and c_m the maximum possible ion concentration in the particle (or equivalently, the available intercalation site concentration).

As first introduced by Han et. al. [89], and later developed by Bazant and coworkers [15, 188, 31, 8, 48, 47, 237], the phase-field ion intercalation model based on the nonequilibrium chemical thermodynamics suggests that the chemical potential μ obeys a generalized Cahn-Hilliard type regular solution model,

$$\mu = k_B T \ln \frac{c}{c_m - c} + \Omega \frac{c_m - 2c}{c_m} - \frac{\nabla \cdot (\mathbf{K}\nabla c)}{c_m^2}, \tag{4.3}$$

where Ω is enthalpy of mixing per site and $\mathbf{K}$ the gradient energy penalty tensor. In fact, the four terms in the chemical potential expression represent the contributions from entropy, enthalpy, gradient energy penalty and the elastic stain effect, respectively.

In the surface electron-conducting coating layer, we assume that the transport of electron (polaron) satisfies the linear diffusion equation with reaction,

$$\frac{\partial c_e}{\partial t} = D_e \nabla^2 c_e + R_e, \tag{4.4}$$

where c_e is the concentration of electron, D_e the effective diffusivity of electron in the coating and R_e the volumetric reaction rate of electron. Due to the charge conservation restriction, along the particle surface $R + R_e = 0$ must hold.

At the particle surface, the reaction rate, or similarly the current density across the particle-coating interface, is governed by the generalized Butler-Volmer equation [15],

$$i = i_0 \left(1 - \frac{c}{c_m}\right) \left(\frac{c}{c_m}\right)^{\alpha} a_e^{1-\alpha} \exp\left(\frac{\alpha\mu}{k_B T}\right) \left(\exp\left(-\frac{\alpha\eta}{k_B T}\right) - \exp\left(\frac{(1-\alpha)\eta}{k_B T}\right)\right), \tag{4.5}$$

where I is the surface current density, I_0 the exchange current density, a_e the activity of electron, α the charge transfer coefficient, μ the chemical potential at the particle surface, and η the overpotential. Here we already assume that the number of electrons involved in the electrode reaction $n = 1$.

The assumption of no charge accumulation within the carbon coating is enforced, then by the charge conservation, total current I should equal to the integral of the current density over all the particle-carbon coating surface,

$$\int i dS = I. \tag{4.6}$$

4.2.2 Reduction to Two-dimensional Model and Boundary Conditions

The computational cost of a full three dimensional simulation for the general model system can be tremendously high, especially a shock wave is expected to propagate across the whole particle. In order to study the dynamics of ion-intercalation, we will reduce the system to a two dimensional one, and provide the boundary conditions to close the system.

According to the 3D single particle simulation by Tang, Belak and Dorr [202], the lithium ion concentration will mostly be uniform along the c-direction. Elastic strain studies on the lithium iron phosphate particle also provide supports to this statement [212, 48, 47]. This conclusion leads to an assumption that the c-direction can be neglected, which results a two dimensional system [55].

In this work, the geometry of the particle-carbon coating system is assumed to be in a "sandwich" shape. We assume that the intercalation particle is in the square shape of size l_p-by-l_p, with two thin carbon coating layers on the upper edge and the

lower edge of thichness l_c. The ion can enter the coating layer only at four corners of the coating, and ion intercalates into the particle through any surface other than the coating layer-particle interface will be neglected. Within the coating layer, we assume that the thickness of the coating is so small that the concentration is also uniform along the depth direction (b-direction).

On the boundaries of the particle, we apply the variational boundary condition, or the "surface wetting" condition,

$$\hat{n}_i \cdot \nabla c = c_m^2 \frac{\partial \gamma_s}{\partial c}, \tag{4.7}$$

where $\hat{n}_i$ is the normal unit vector of this boundary surface and γ_s the surface energy per area. In this work, we will simply assume γ_s be a constant independent of concentration, which leads to a "no-wetting" boundary condition,

$$\hat{n}_i \cdot \nabla c = 0. \tag{4.8}$$

Due to the mirror symmetry of our model, we can only simulate a quarter of the whole domain to obtain the full dynamics. Therefore, in the following parts, we apply this symmetric condition and report the results from this quarter domain. A schematic of this quarter domain is shown in Fig. 4-1.

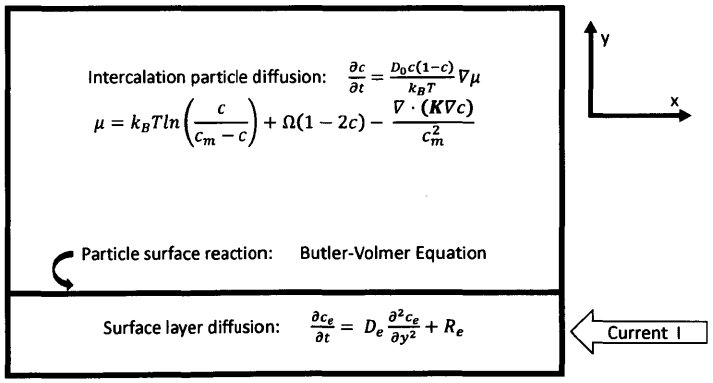

Figure 4-1: Quarter domain schematic of the 2D intercalation particle with conducting surface layer model addressed in this paper.

4.2.3 Simulation details

In the numerical studies, we follow the parameter setting in Table 4.1, which is consistent with the previous 1D Cahn-Hilliard system simulation [237]. We will neglect the effect of heat generation during the charging/discharging, which makes itself an isothermal system.

Table 4.1: Parameter settings for LFP [48, 47, 237] used in the numerical simulations, except as otherwise noted.

Parameter	Value	Unit	Parameter	Value	Unit
l_p	1×10^{-7}	m	l_c	1×10^{-9}	m
Ω	0.115	eV	c_m	1.379×10^{28}	m^-3
$c(x, y, t = 0)$	1.379×10^{26}	m^-3	$c_e(x, t = 0)$	1.379×10^{28}	m^-3
D_e	1×10^{-14}	m^2/s	α	0.5	-
V^{Θ}	3.42	V	i_0	1.6×10^{-4}	A/m^2

Ω is set to be greater than $2k_BT$, which indicates a phase separation is always favored in energy [237] at room temperature T.

The diffusion coefficients in two directions D_x and D_y are known to be very anisotropic in the lithium iron phosphate. While their fitting values to experiment data significantly differs from the *ab initio* calculation by several orders of magnitude [191, 52, 150], no value of them is widely accepted. We will vary these two parameters within some range and see observe how they affect the charging/discharging dynamics.

Another source of anisotropy comes from the penalty tensor $\mathbf{K}$, which controls the interfacial thickness scale of the phase boundary during phase separation. In this work, we assume $\mathbf{K}$ contains only diagonal non-zero components, κ_x and κ_y. In general, a larger κ value will make the sharp phase boundary less favorable in energy.

As the initial concentration of electron in the surface coating $c_e(x, t = 0)$ and the diffusivity of electron D_e are both unknown, we simply assume that $c_e(x, t = 0) = c_m$ and D_e matches the magnitude of ion diffusivity in the 1D CHR model [237] for an initial exploration.

4.3 Numerical results

In this section, we numerically study the phase separation dynamics of the coupled 2D Cahn-Hilliard reaction system given in Fig. 4-1. We mainly study how the phase boundary orientation is affected by the different parameters D_x, D_y and $\mathbf{K}$ during the constant voltage discharging processes. The study of surface carbon-coating effect on the overall electrokinetics is also conducted in a constant current discharging setting.

In order to solve the coupled PDE system, we simply apply the standard finite volume method to discretize the whole system into an ODE system. We then employ the ODE15s solver in MATLAB to solve the obtained ODE system.

4.3.1 Constant voltage: phase boundary orientations

In previous modeling work [8, 48, 47], one important method for model complexity reduction is called the "depth-average approximation", by which the concentration with the same x-coordinate will be assumed to be equal. This approximation is made according to the results from phase field simulation that the phase boundary always aligns with the depth direction [145, 202].

Intuitively, this assumption should hold for small particles with a low Li/Fe anti-site defect rate [133], which leads to a significant difference between two directional diffusion coefficients $D_y \gg D_x$. In this scenario, the diffusion in the y direction is so fast that it should easily reach the quasi-equilibrium state, a uniform concentration profile [188].

However, the result from a constant voltage discharging simulation shows an exactly opposite profile. By setting D_y eight orders larger than D_x, the penalty tensor in gradient isotropic $\kappa_x = \kappa_y$; contrary to our expectation, the phase boundary is perpendicular to our previous assumption, as shown in Fig. 4-2.

One possible way to interpret this phenomenon is by the Cahn-Hilliard chemical potential function. When the concentration hits the spinodal decomposition point during the discharging, it tends to attract ions from all nearby sites. Because of the anisotropy nature of directional diffusivities, it is much easier for ions to move along

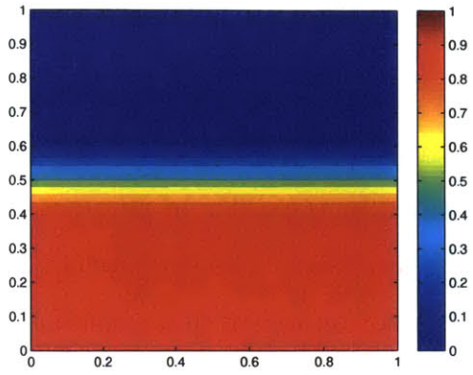

Figure 4-2: Concentration profile in the particle at half filled during a constant voltage discharging at $V = 3.0$ V. The diffusivities in two directions are $D_x = 1 \times 10^{-22}$ m^2/s and $D_y = 1 \times 10^{-14}$ m^2/s, while $\kappa_x = \kappa_y = 3 \times 10^{10}$ eV/m.

the y direction than in the other direction. Meanwhile, although the concentration changes considerably along each y axis channel, the Cahn-Hilliard chemical potential function guarantees that the chemical potential still stays constant in that channel, which is stable as a quasi-equilibrium state [31]. Therefore, the phase boundary will be stable kinetically as being perpendicular to the fast-diffusion axis.

One further observation supports the above explanation. When we enlarge the gradient penalty in the y direction, which makes it less likely to phase separate in this direction, we do observe a desired phase boundary orientation. However, when we decrease the diffusivity in the x direction, the boundary rotates 90 degrees again. The comparison of two simulations is shown in Fig. 4-3.

Consequently, contrary to previous statements [188], a depth-average approximation is more likely to be valid for a more isotropic environment for ion diffusion, which normally links to a high Li/Fe antisite defect rate or a bigger particle size. As we neglect the elasticity in the particle, this factor can also determine the boundary orientation, as reported [48, 47, 64].

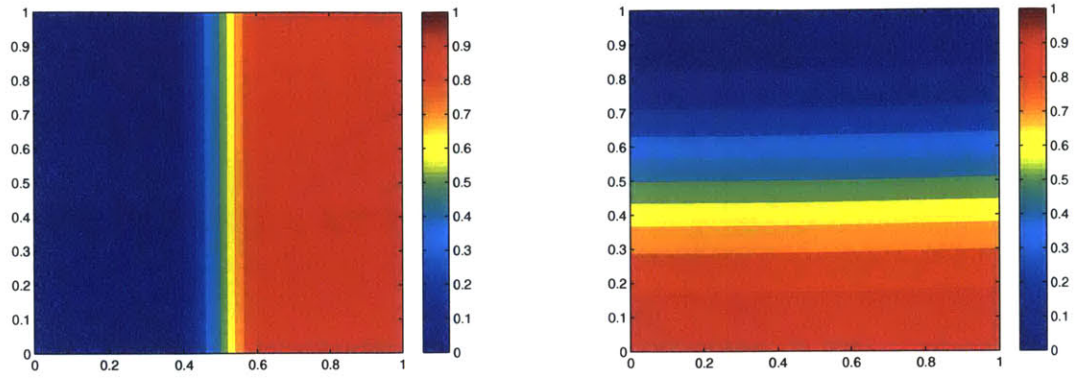

Figure 4-3: Phase boundary orientation comparison of two half-filled particles during a constant voltage discharging at $V = 3.0$ V. The diffusivity in y direction is $D_y = 1 \times 10^{-14}$ m^2/s, $\kappa_x = 3 \times 10^{10}$ eV/m and $\kappa_y = 3 \times 10^{11}$ eV/m for both. The diffusivity in x direction is $D_x = 1 \times 10^{-14}$ m^2/s $= D_y$ (left) and $D_x = 1 \times 10^{-22}$ m^2/s $\ll D_y$ (right), respectively

4.3.2 Constant current: voltage and capacity

During a constant current charging/discharging, the ion-intercalated battery potential drop from the open circuit voltage is generally interpreted as a result of the ion transport limitation. In fact, even for the same battery material, fitting the voltage curve by varying ion diffusivity in the particle bulk to different experimental data has led to various orders of magnitude in their resulting values. While this should not happen, since the ion diffusivity in the particle is a fixed material property under a given certain condition, the cause of this disagreement is still unknown.

In fact, in the constant current simulations of the new 2D Cahn-Hilliard reaction and surface coating model, we see that the coating property can dramatically change the dynamical behavior in the discharging process. As shown in Fig. 4-4, when the electron conduction in the surface coating layer is the rate-determining step for ion-intercalation, $D_e \ll D_{bulk}$, even while the bulk material properties may stay the same, the voltage curve could shift significantly and a reduction in capacity be observed.

A comparison of concentration profiles within the surface conducting layers at the moment of half-filled with different diffusivities is presented in Fig. 4-5. We observe that the lithium reaches the transport limit only in the case $D_e = 1 \times 10^{-16}$ m^2/s,

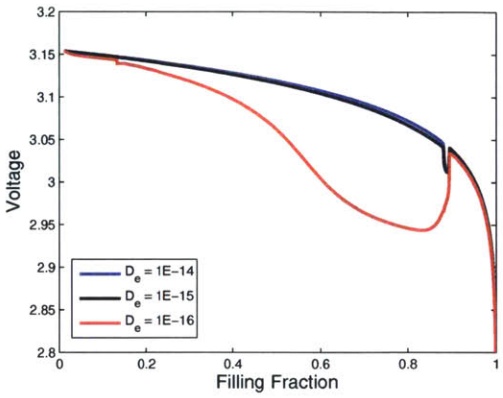

Figure 4-4: Voltage curves of three constant current discharging processes with the same bulk material properties but different surface coating diffusivities. The C-rate for discharging is at 1, and the electron diffusion coefficients D_e are at 1×10^{-14} m^2/s, 1×10^{-15} m^2/s and 1×10^{-16} m^2/s, respectively.

which corresponds to the significant capacity lost shown in Fig. 4-4. If one only fits the bulk diffusivity to the experimental data, neglecting the surface coating electron conduction, it will certainly lead to some misleading values of D_{bulk}.

4.4 Conclusion

In this work, we proposed a two-dimensional Cahn-Hilliard reaction ion-intercalation particle model, coupled with a thin electron-conducting coating layer on the particle surface, with interface electron transfer reaction rate governed by the phenomenological generalized Butler-Volmer equation. Numerically studying the discharging processes, we explored how the system dynamics depend on different material properties. We found that, under high rate situations, lithium intercalation is confined within a region that is limited by electron transport. This surface coating layer significantly affects the battery electrokinetics and could be an alternative reason for the capacity loss at high rate situations, which has previously only be interpreted as concentration polarization or transport limitation in the electrolyte.

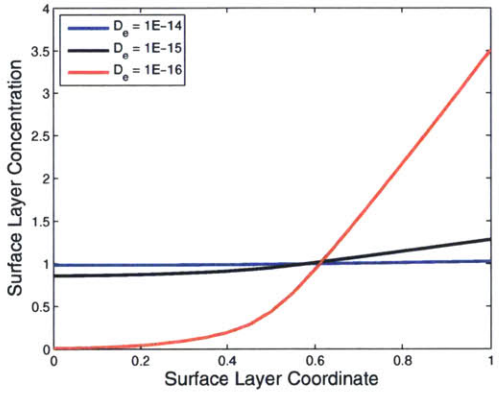

Figure 4-5: Concentration profiles within surface conducting layers of three constant current discharging processes with the same bulk material properties but different surface coating diffusivities. The C-rate for discharging is at 1, and the electron diffusion coefficients D_e are at 1×10^{-14} m^2/s, 1×10^{-15} m^2/s and 1×10^{-16} m^2/s, respectively.

Chapter 5

Simple Formula for Marcus-Hush-Chidsey Kinetics

5.1 Introduction

The microscopic theory of electron transfer [117, 13] has been developed and tested in electroanalytical chemistry for almost seventy years since the pioneering work of Marcus [136, 141, 137]. Although much of the early work focused on homogeneous electron transfer in solution, the theory was also extended to heterogeneous electron transfer at electrodes [137, 135, 95] and found to accurately predict Faradaic reaction kinetics for both liquid [42, 147, 95] and, more recently, solid [9] electrolytes. For metal electrodes, however, the theory is complicated by the need to integrate the Marcus rate over the Fermi-Dirac distribution of electrons. This integral cannot be evaluated in closed form in terms of elementary functions and has only been approximated (in certain limits) by relatively cumbersome series expansions [162, 147, 148].

Partly for this reason, despite its successes, the theory is rarely used and poorly known in engineering. Instead, standard mathematical models are based on the phenomenological Butler-Volmer (BV) equation [24, 155], which has the appeal of a simple analytical formula that fits many experimental measurements, even though it lacks a clear physical basis. The goal of this work is to derive an equally simple formula for the microscopic theory.

5.2 Background

For the simple redox reaction, R $\leftrightarrow$ O + e^-, the BV reductive and oxidative reaction rates, are expressed as,

$$\begin{aligned} k_{red}^{BV}(\eta,\alpha) &= k_0^{BV} \exp\left(\frac{-\alpha e\eta}{k_B T}\right), \\ k_{ox}^{BV}(\eta,\alpha) &= k_0^{BV} \exp\left(\frac{(1-\alpha) e\eta}{k_B T}\right), \end{aligned} \tag{5.1}$$

where k_0^{BV} is the rate constant, α the charge transfer coefficient, e the elementary charge, η the applied overpotential, k_B Boltzmann's constant and T the temperature. The net reduction current is proportional to the difference in forward and backward rates, $I \propto k_{red} - k_{ox}$, in the standard form of the BV equation. The ratio of forward and backward rates satisfies the de Donder relation,

$$\frac{k_{red}}{k_{ox}} = \exp\left(-\frac{e\eta}{k_B T}\right) \tag{5.2}$$

which is a general constraint from statistical thermodynamics for thermally activated chemical kinetics [15, 184]. The BV model asserts that the reaction rate in either direction follows the Tafel relationship, in which the thermodynamic driving force is a constant fraction of the applied overpotential. This dependence is empirical but can be justified by various phenomenological models [24, 13], where the electrostatic energy of the (ill-defined) transition state of the reaction is an average of that in the reduced and oxidized states, weighted by the charge transfer coefficient [15].

In contrast, the microscopic theory of outer-sphere electron transfer focuses on solvent reorganization prior to iso-energetic electron transfer [137, 117, 13]. In the simplest form of the theory, the free energy of the reduced and oxidized states has the same harmonic dependence on a reaction coordinate for solvent reorganization (such as local dielectric constant of the solvation shell), before and after electron transfer.

For the same redox reaction above, the reaction rates take the form [195, 42, 15],

$$k^M_{red/ox}(\Delta G) = k^M_0 \exp\left(-\frac{(\Delta G \pm \lambda)^2}{4\lambda k_B T}\right), \tag{5.3}$$

where ΔG is the free energy change upon reduction, and λ is the reorganization energy, i.e. the free energy required to completely reorganize the local atomic configuration of one state to the other state *without* charge transfer.

If the redox reaction occurs at an electrode, electrons in the metal electrode occupying different energy levels around the Fermi level may all participate in the reaction, which results in multiple intersections between two families of parabolae [135]. Although this principle was first identified decades ago, the importance of incorporating the Fermi-Dirac distribution of electrons/holes into the classical Marcus theory was not widely recognized until Chidsey found perfect agreement between the modified rate equation and the curved Tafel plot obtained from his seminal experiments on redox active self-assembled monolayers (SAMs) [42]. The rate equation implemented by Chidsey, now known as the Marcus-Hush-Chidsey (MHC) [95] or Marcus-DOS model [76], can be written as,

$$k^{MHC}_{ox/red}(\eta) = A \int_{-\infty}^{\infty} \exp\left(-\frac{(x - \lambda \pm e\eta)^2}{4\lambda k_B T}\right) \frac{dx}{1 + \exp(x/k_B T)}, \tag{5.4}$$

where A is the pre-exponential factor, accounting for the electronic coupling strength and the electronic density of states (DOS) of the electrode. The first term in the integrand is the classical Marcus rate for the transfer of an electron of energy x relative to the Fermi level, and the second factor is the Fermi-Dirac distribution assuming a uniform DOS. The reductive and oxidative reaction rates satisfy the de Donder relationship, Eq. 5.2, as well as a "reciprocity relationship" noted by Oldham and Myland [162], $k^{MHC}_{ox}(-\eta) = k^{MHC}_{red}(\eta)$.

The three models are compared on a Tafel plot in Figure 5-1, which highlights dramatic differences in the predicted rate for large overpotentials. While the BV rate increases exponentially without bound along a traditional "Tafel line", the Marcus rate reaches a maximum at the reorganization voltage ($\eta = \lambda/e$) and then decreases

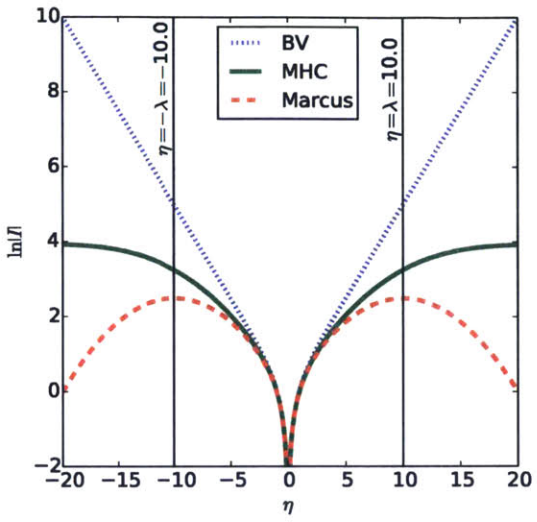

Figure 5-1: Dimensionless Tafel plots of Butler-Volmer kinetics (BV) with charge transfer coefficient $\alpha = \frac{1}{2}$ compared with Marcus (M) and Marcus-Hush-Chidsey (MHC) kinetics with reorganization energy λ (scaled to the thermal energy k_BT). The absolute value of the current $|I|$ scaled to the exchange current I_0 is plotted on a logarithmic scale versus the overpotential η scaled to the thermal voltage, k_BT/e. The M and MHC curves assume a typical value [42, 9] of the dimensionless reorganization energy, $\lambda = 10$ scaled to k_BT.

rapidly (as a Gaussian) along an inverted parabola. The latter is the famous "inverted region" predicted by Marcus for homogeneous electron transfer [137]. The MHC model predicts a curved Tafel plot that neither diverges nor decays, but instead approaches a constant reaction-limited current.

The disappearance of the inverted region originates from the distribution of electrons in the metal electrode, as shown in Fig. 5-2. When a positive free-energy barrier is formed in the inverted region in response to the large overpotential, electrons below the Fermi level (μ_e) with roughly unity Fermi factor follow a lower-energy parabola that enables a barrier-less transfer, which dominates the overall reduction rate and leads to a constant, non-zero limiting current [161, 88, 180]. More detailed comparisons between BV and MHC kinetics can be found in Appleby and Zagal [6], Chen and Liu [40], and the enlightening review of Henstridge et al. [95].

Evidence is mounting that MHC kinetics are essential for the understanding and engineering of important electrochemical interfaces. The MHC model has been extensively used in the microscopic analysis of electron transfer at SAMs [42, 95]

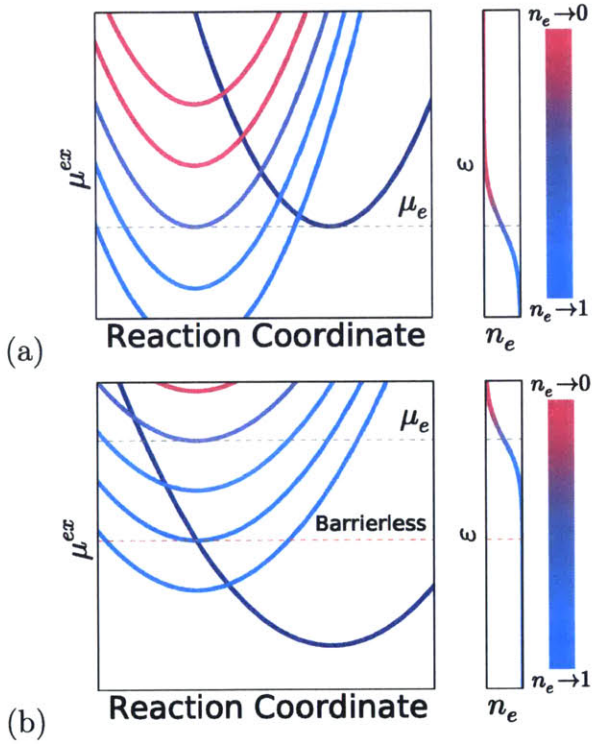

Figure 5-2: Physical interpretation of MHC kinetics for the Faradaic reaction, O + $e^- \rightarrow$ R, at a metal electrode. In each panel, a parabola for the free energy (or more precisely, excess electrochemical potential [15]) of the reduced state (R, right) versus reorganization reaction coordinate intersects a family of parabolae for the free energy of the oxidized state plus the free electron (O + e^-, left), sampled from the Fermi-Dirac distribution with electron energies, ε, shown. (a) Exchange process at zero overpotential, dominated by electrons near the Fermi level following Marcus kinetics. (b) Reaction-limited current at large negative overpotential, dominated by lower-energy electrons below the Fermi level undergoing barrier-less transitions.

and electrochemical molecular junctions [147]. It could also be important for nano-electrochemical systems working at large overpotentials, such as resistive-switching memory [221] or integrated circuits with ultrathin gate dielectrics, where the BV model predicts unrealistically large reaction rates [152]. Recent Tafel analysis of Li-ion battery porous electrodes consisting of carbon-coated $LiFePO_4$ particles has further verified MHC kinetics for electron transfer at the carbon-$LiFePO_4$ (solid-solid) interface [9], contrary to all existing battery models, which assume BV kinetics. For simple outer-sphere reactions, the symmetric MHC model (considered here) provides an excellent fit of the measured reaction rates [42, 9]. In other situations (with negligible double-layer Frumkin effects [26, 16, 22]), the asymmetric MH model is required with different reorganization energies for the forward and backward reactions [118, 200, 196], due to different inner-sphere (non-electrostatic, vibrational) [93, 97] or outer-sphere (nonlinear solvation) [143, 119] force constants for the reduced and oxidized states.

One possible reason MHC kinetics have been overlooked is the complexity of the rate expression Eq. 5.4 as an improper integral that cannot be evaluated in terms of elementary functions, like the BV equation. In order to avoid numerical quadrature, there have been several attempts to derive simpler analytical approximations. Oldham and Myland [162] recently obtained an exact solution involving sums of a function that is a product of an exponential function and a complementary error function, which leads to some convenient alternatives for limited ranges of the parameters. Migliore and Nitzan derived another series solution by an expansion of the Fermi function [147], which is mathematically equivalent to Oldham's solution [148]. As with any series expansion, however, accuracy is lost upon truncation, and the approximations are not uniformly valid across the range of possible reorganization energies and overpotentials.

In this paper, we derive a simple formula by asymptotic matching that accurately approximates the MHC integral over the entire realistic parameter range. In the following sections, we first perform asymptotic analysis of Eq. 5.4 for positive (oxidation) and negative (reduction) overpotentials, then unify both cases by asymptotic matching in a closed-form approximation, and finally demonstrate the accuracy of our

formula compared to numerical quadrature and the recent series solutions. Complete asymptotic series are derived in the appendices for large and small reorganization energies, but only the leading-order terms are used in the main text to obtain our uniformly valid formula.

5.3 Oxidation Rate for Positive Overpotentials

Without loss of generality, we neglect the prefactor A and begin by restricting $\eta > 0$ for the oxidation rate. Eq. 5.4 can then be rewritten as,

$$k(\lambda, \eta) = \int_{-\infty}^{+\infty} g(x; \lambda, \eta) f(x) dx, \tag{5.5}$$

where the original integrand is separated to a Gaussian function g and the Fermi distribution f,

$$\begin{aligned} g(x; \lambda, \eta) &= \exp\left(-\frac{(x - \lambda + \eta)^2}{4\lambda}\right), \\ f(x) &= \frac{1}{1 + \exp(x)}. \end{aligned} \tag{5.6}$$

For mathematical convenience, all quantities starting from Eq. 6.1 will be dimensionless: x and λ are scaled to $k_B T$ and η to $k_B T/e$.

5.3.1 Small reorganization energies, $\lambda \ll 1$

When $\lambda \ll 1$, the Gaussian function g has a narrow peak at $x = \lambda - \eta$. We will apply the Laplace method [41], where we expand the function g around the point $x = \lambda - \eta$ by Taylor expansion, and then integrate all the terms separately. Derivations and the full series solution can be found in Section 5.7. Here, we use the leading asymptotic term of the integral,

$$k(\lambda, \eta) \approx \frac{2\sqrt{\pi\lambda}}{1 + \exp(\lambda - \eta)}, \tag{5.7}$$

as our asymptotic approximation for cases of small λ.

5.3.2 Large reorganization energies, $\lambda \gg 1$

For an outer-sphere reaction, λ is usually larger than 1, and the series solution given in Eq. 5.23 may converge slowly. A more accurate approximation for the integral in Eq. 6.1 in this limit is based on the observation,

$$\lim_{a \to +\infty} \frac{1}{1 + \exp(ax)} = 1 - H(x), \tag{5.8}$$

where $H(x)$ is the Heaviside step function defined to be $H(x) = 0$ for $x < 0$ and, $H(x) = \frac{1}{2}$ for $x = 0$ and $H(x) = 1$ elsewhere. This corresponds to the zero temperature limit of the Fermi-Dirac distribution, which enables an accurate approximation to the original integral [88],

$$k(\lambda, \eta) \approx \int_{-\infty}^{+\infty} g(x; \lambda, \eta)\,(1 - H(x))\,dx = \sqrt{\pi\lambda}\,\mathrm{erfc}\left(\frac{\lambda - \eta}{2\sqrt{\lambda}}\right), \tag{5.9}$$

where $\mathrm{erfc}(\cdot)$ is the complementary error function. The derivation of the correction series to this approximation is available in Section 5.8.

5.4 Oxidation rate for negative overpotentials

Combining the de Donder relation and reciprocity relations for MHC kinetics [162], we obtain a symmetry condition

$$\frac{k(\lambda, \eta)}{k(\lambda, -\eta)} = \exp(\eta), \tag{5.10}$$

which directly yields the leading-order approximation for $\eta < 0$. When $\lambda \ll 1$, by using Eq. 5.7 and Eq. 5.10, we have,

$$k(\lambda, \eta) = \exp(\eta) k(\lambda, -\eta) \approx \frac{2\sqrt{\pi\lambda}\exp(\eta)}{1 + \exp(\lambda + \eta)}. \tag{5.11}$$

And for the case of $\lambda \gg 1$, by using Eq. 5.9 and Eq. 5.10, we obtain

$$k(\lambda, \eta) \approx \sqrt{\pi\lambda} \exp(\eta) \operatorname{erfc}\left(\frac{\lambda + \eta}{2\sqrt{\lambda}}\right). \tag{5.12}$$

We thus obtain asymptotic approximations of the integral 6.1 for all η, in the limit $\lambda \ll 1$,

$$k(\lambda, \eta) \approx \begin{cases} \dfrac{2\sqrt{\pi\lambda}}{1 + \exp(\lambda - \eta)} & \text{for } \eta \geq 0 \text{ and } \lambda \ll 1, \\ \dfrac{2\sqrt{\pi\lambda}\exp(\eta)}{1 + \exp(\lambda + \eta)} & \text{for } \eta < 0 \text{ and } \lambda \ll 1, \end{cases} \tag{5.13}$$

and the limit $\lambda \gg 1$,

$$k(\lambda, \eta) \approx \begin{cases} \sqrt{\pi\lambda} \operatorname{erfc}\left(\dfrac{\lambda - \eta}{2\sqrt{\lambda}}\right) & \text{for } \eta \geq 0 \text{ and } \lambda \gg 1, \\ \sqrt{\pi\lambda} \exp(\eta) \operatorname{erfc}\left(\dfrac{\lambda + \eta}{2\sqrt{\lambda}}\right) & \text{for } \eta < 0 \text{ and } \lambda \gg 1. \end{cases} \tag{5.14}$$

5.5 Uniformly Valid Approximation

In order to get a closed form expression valid for all η, we multiply the $\eta \geq 0$ approximation by a function $M(\eta)$ that interpolates between the asymptotic limits, $M(\eta) \to 1$ for $\eta \to \infty$ and $M(\eta) \sim e^{\eta}$ for $\eta \to -\infty$. In order to make the expression differentiable, we also introduce a function $N(\eta)$ to continuously approximate the absolute value function,

$$k(\lambda, \eta) \approx \sqrt{\pi\lambda} M(\eta) \operatorname{erfc}\left(\frac{\lambda - N(\eta)}{2\sqrt{\lambda}}\right). \tag{5.15}$$

Although it is possible to also construct a uniformly valid approximation for all λ in a similar way, we consider only the $\lambda \gg 1$ approximation, which turns out to be accurate even down to $\lambda \approx 0.1$ and covers the physically relevant range for outer sphere reactions. Below such small values of the reorganization energy, the barrier to charge transfer is too small to justify the use of transition state theory, and MHC kinetics break down.

For smooth $M(\eta)$ and $N(\eta)$, the uniformly valid approximation removes the dis-

continuous derivative at $\eta = 0$ that would arise by naively patching the two asymptotic approximations for $\eta > 0$ and $\eta < 0$. The de Donder relation can also be satisfied exactly if we require $M(\eta) = e^{\eta} M(-\eta)$. These properties are satisfied by the following simple choices for the interpolating functions

$$\begin{aligned} M(\eta) &= \frac{1}{1+\exp(-\eta)}, \\ N(\eta) &= \sqrt{a+\eta^2}, \end{aligned} \tag{5.16}$$

where a is an arbitrary constant, yielding the uniformly valid approximation

$$k(\lambda, \eta) \approx \frac{\sqrt{\pi\lambda}}{1+\exp(-\eta)} \operatorname{erfc}\left(\frac{\lambda - \sqrt{a+\eta^2}}{2\sqrt{\lambda}}\right). \tag{5.17}$$

A comparison between different approximations (small λ limit, large λ limit, and uniform approximation) and the direct numerical integration of MHC for various λ values are shown in Figure 5-3. Remarkably, we find that Eq. 5.17 with $a = 1 + \sqrt{\lambda}$ provides very accurate approximation to the MHC integral (Eq. 6.1) across the full range of physical parameter values. The numerical results almost overlap everywhere, as shown in Fig. 5-3.

Numerical evaluations of the relative errors of our simple formula 5.17 under different choices of λ are shown in Fig. 5-4, including a comparison with the series solution by Oldham and Myland [162] for $\lambda = 10$. It is clearly seen that our approximation exhibits $< 10\%$ relative error even in the most extreme cases. For more relevant cases for outer sphere reactions (e.g. $\lambda \approx 10$) [9, 42], the relative error is less than 5% for small overpotentials and vanishingly small at large positive or negative overpotentials.

Finally, we arrive at our main result. By subtracting the oxidation rate from the reduction rate, $I(\lambda, \eta) = k(-\eta, \lambda) - k(\eta, \lambda)$, we obtain a simple, accurate, formula for the net reduction current (up to a constant pre-factor):

$$I(\lambda, \eta) \approx \sqrt{\pi\lambda} \tanh\left(\frac{\eta}{2}\right) \operatorname{erfc}\left(\frac{\lambda - \sqrt{1+\sqrt{\lambda}+\eta^2}}{2\sqrt{\lambda}}\right). \tag{5.18}$$

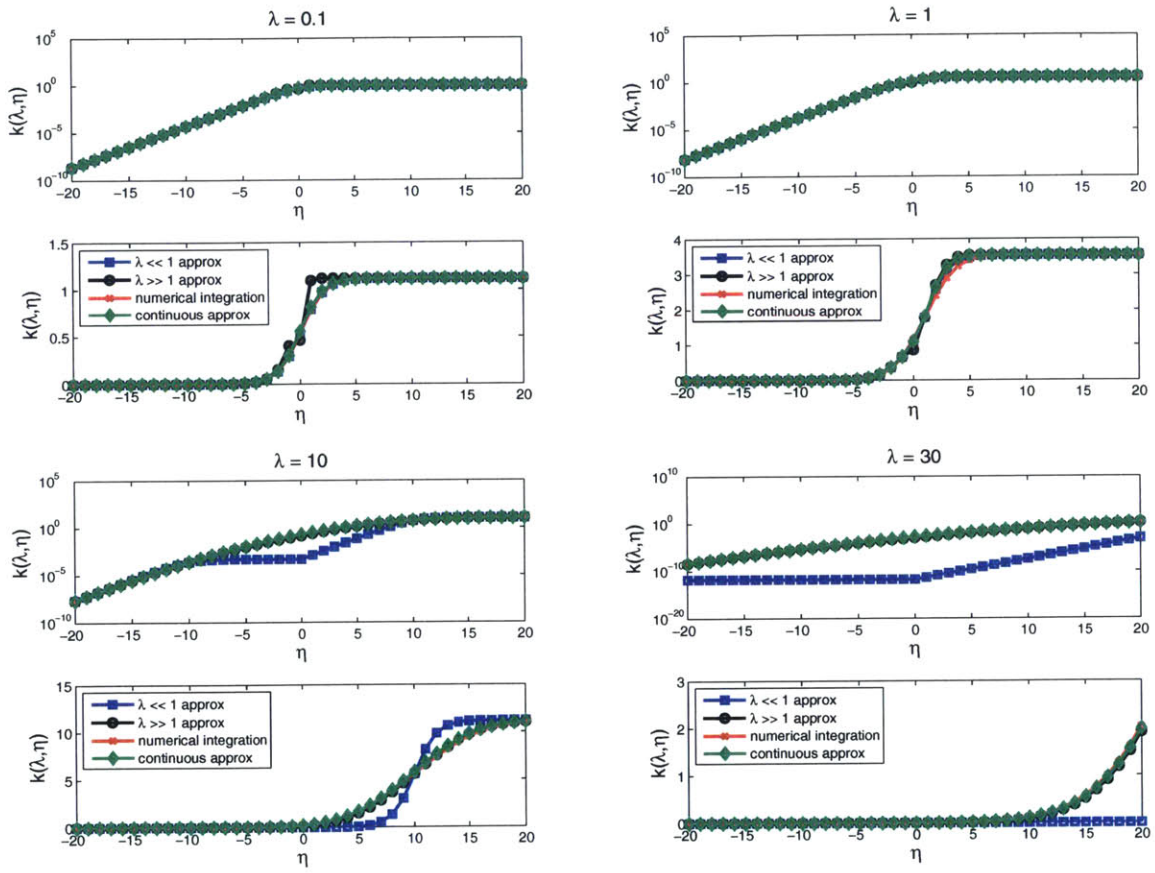

Figure 5-3: Numerical evaluations of reaction rates $k(\lambda, \eta)$ according to three asymptotic approximations Eq. 5.13 (blue square), Eq. 5.14 (black circle) and Eq. 5.17 (green diamond), together with the direct numerical quadrature of the MHC integral 6.1 (red cross) for $\lambda = 0.1$, 1, 10 and 30 and $|\eta| < 20$. Each comparison is shown in both log scale (top) and linear scale (bottom).

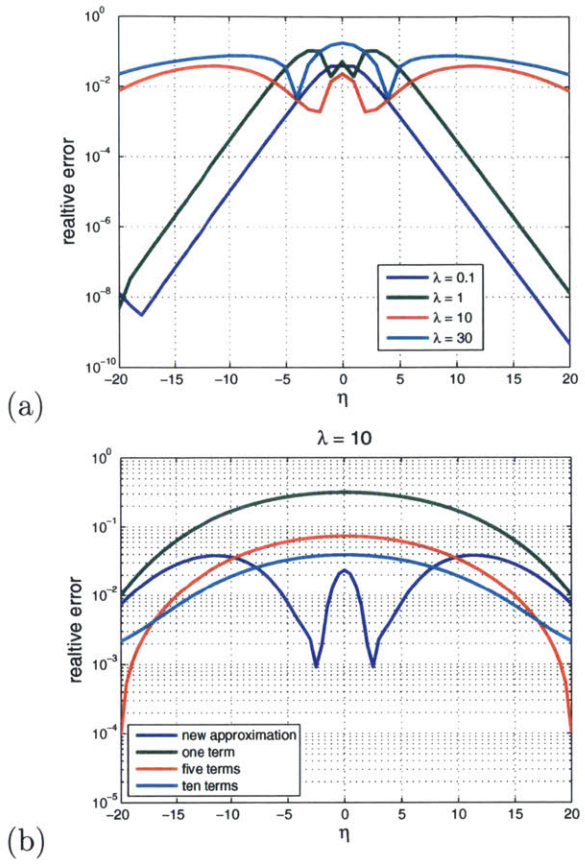

Figure 5-4: (a) Relative error of our simple formula Eq. 5.17 compared to numerical quadrature of the MHC integral 6.1 for $\lambda = 0.1$, 1, 10 and 30 and $|\eta| < 20$. (b) Relative error of our formula for $\lambda = 10$ compared with the series approximation of Oldham and Myland [162] with 1, 5 and 10 terms.

This expression is almost as simple and efficient to evaluate as the BV equation, while accurately approximating the MHC integral over the entire physical parameter range. For example, on a dual-core processor using Python with Scipy, the evaluation of Eq. 5.18 is only about four times slower than that of the BV equation, but about 1500 times faster than an efficient numerical quadrature of the MHC integral using a subroutine from the Fortran QUADPACK library (with $\lambda = 10$).

From Eq. 5.18, the exchange current (up to the same constant) is the forward or backward rate in equilibrium,

$$I_0(\lambda) = k(\lambda, 0) \approx \frac{\sqrt{\pi\lambda}}{2} \operatorname{erfc}\left(\frac{\lambda - \sqrt{1+\sqrt{\lambda}}}{2\sqrt{\lambda}}\right), \tag{5.19}$$

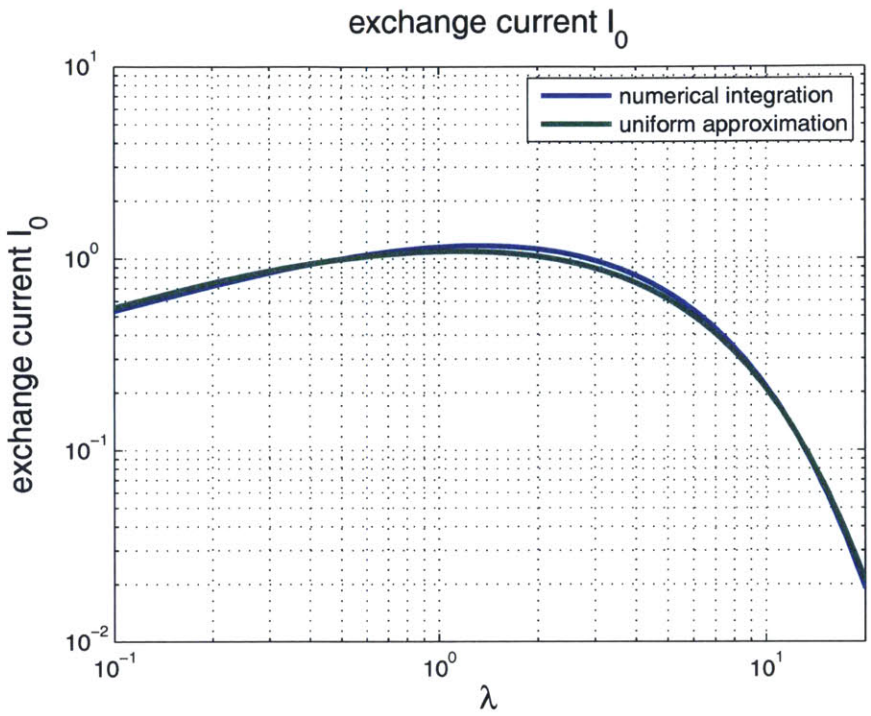

Figure 5-5: Dimensionless exchange current $k(\lambda, \eta = 0)$ versus reorganization energy λ for numerical quadrature of the MHC integral compared to the uniformly valid approximation, Eq. 5.19, showing maximum 5% error when $0.1 \leq \lambda \leq 20$.

which decays exponentially for large reorganization energies,

$$I_0 \approx \exp\left(-\frac{\lambda}{4}\right), \qquad \lambda \gg 1. \tag{5.20}$$

As shown in Fig. 5-4, the greatest error in our formula occurs at small over-potentials, but as shown in Fig. 5-5, the accuracy is quite satisfactory even at $\eta = 0$ for a wide range of reorganization energies.

5.6 Conclusion

In order to facilitate the application of the MHC kinetics in electrochemical engineering, we derive a simple approximation by asymptotic matching that serves as a practical alternative to the BV equation for electrochemical engineering. Our formula improves upon classical asymptotic approximations [161, 88, 180] and recent series

expansions [162, 147, 148] and provides the first uniformly valid approximation for all reasonable choices of the reorganization energy and overpotential with less than 5% error at small overpotentials and vanishing error at large overpotentials. A natural next step would be to extend our formula for the general asymmetric Marcus-Hush model with different reorganization energies for the reduced and oxidized states [118]. These results could be conveniently used in classical battery models [155] or new models based on non-equilibrium thermodynamics [15] for electrode phase transformations limited by Faradaic reactions [9]. Switching from Butler-Volmer to Marcus-Hush kinetics could have dramatic implications for the understanding and optimization of electrochemical systems working at high overpotentials.

5.7 Small λ Limit

The Taylor series of the Fermi distribution function f defined in Eq. 5.6 around $x = \lambda - \eta$ is,

$$f(x) = \sum_{n=0}^{\infty} \frac{(x - \lambda + \eta)^n}{n!} f^{(n)}(\lambda - \eta). \tag{5.21}$$

If we put this expression back to Eq. 6.1, we get,

$$\begin{aligned} k(\lambda, \eta) =& 2\sqrt{\pi\lambda} \sum_{n=0}^{\infty} \frac{f^{(n)}(\lambda - \eta)}{n!} \\ & \int_{-\infty}^{+\infty} \frac{1}{2\sqrt{\pi\lambda}} (x - \lambda + \eta)^n \exp\left(-\frac{(x - \lambda \pm \eta)^2}{4\lambda}\right) dx. \end{aligned} \tag{5.22}$$

For each n, the integral is exactly the n-th central moment of a normal distribution with variance $\sigma^2 = 2\lambda$, then the value for such an integration is,

$$\begin{aligned} & \int_{-\infty}^{+\infty} \tfrac{1}{2\sqrt{\pi\lambda}} (x - \lambda + \eta)^n \exp\left(-\tfrac{(x-\lambda\pm\eta)^2}{4\lambda}\right) dx \\ = & \begin{cases} 1 & \text{for } n = 0, \\ 0 & \text{for } n \text{ is odd}, \\ (2\lambda)^{\frac{n}{2}} (n-1)!! & \text{for } n > 0 \text{ is even}. \end{cases} \end{aligned}$$

Therefore, the series for $k(\lambda, \eta)$ is,

$$k(\lambda, \eta) = 2\sqrt{\pi\lambda} \sum_{n=0}^{\infty} \frac{\lambda^n}{n!} f^{(2n)}(\lambda - \eta). \tag{5.23}$$

5.8 Large λ Limit

For large λ, we first rewrite Eq. 6.1 as,

$$\begin{aligned} k(\lambda, \eta) = &\int_{-\infty}^{+\infty} g(x; \lambda, \eta) \left(1 - H(x)\right) dx \\ &+ \int_{-\infty}^{+\infty} g(x; \lambda, \eta) \left(f(x) - 1 + H(x)\right) dx. \end{aligned} \tag{5.24}$$

The first term on the right hand side of Eq. 5.24 can be exactly solved as shown in Eq. 5.9, while the second half can be simplified to,

$$\begin{aligned} &\int_{-\infty}^{+\infty} g(x; \lambda, \eta) \left(f(x) - 1 + H(x)\right) dx \\ &= -2 \exp\left(-\frac{(\lambda - \eta)^2}{4\lambda}\right) \int_0^{+\infty} \exp\left(-\frac{x^2}{4\lambda}\right) \frac{\sinh \frac{(\lambda - \eta)x}{2\lambda}}{1 + \exp(x)} dx. \end{aligned} \tag{5.25}$$

If we define a new function h as,

$$h(x) = \frac{\sinh \frac{(\lambda - \eta)x}{2\lambda}}{1 + \exp(x)}, \tag{5.26}$$

since $h(x = 0) = 0$, its Maclaurin series is,

$$h(x) = \sum_{n=1}^{\infty} \frac{x^n}{n!} h^{(n)}(0). \tag{5.27}$$

We substitute this back to Eq. 5.25 and obtain,

$$\begin{aligned}
&\int_{-\infty}^{+\infty} g(x;\lambda,\eta)\left(f(x)-1+H(x)\right)dx \\
&= -2\exp\left(-\frac{(\lambda-\eta)^2}{4\lambda}\right)\sum_{n=1}^{\infty}\frac{h^{(n)}(0)}{n!}\int_0^{+\infty} x^n \exp(-\frac{x^2}{4\lambda})dx \\
&= -2\exp\left(-\frac{(\lambda-\eta)^2}{4\lambda}\right)\sum_{n=1}^{\infty} h^{(n)}(0)\frac{2^n}{n!}\lambda^{\frac{n+1}{2}}\Gamma\left(\frac{n+1}{2}\right),
\end{aligned} \tag{5.28}$$

where $\Gamma(\cdot)$ is the gamma function. Thus, the MHC integral in Eq. 6.1 can be expanded asymptotically as,

$$\begin{aligned}
k(\lambda,\eta) &= \sqrt{\pi\lambda}\,\mathrm{erfc}\left(\frac{\lambda-\eta}{2\sqrt{\lambda}}\right) \\
&- 2\exp\left(-\frac{(\lambda-\eta)^2}{4\lambda}\right)\sum_{n=1}^{\infty} h^{(n)}(0)\frac{2^n}{n!}\lambda^{\frac{n+1}{2}}\Gamma\left(\frac{n+1}{2}\right).
\end{aligned} \tag{5.29}$$

Chapter 6

Simple Formula for Asymmetric Marcus-Hush Kinetics

6.1 Introduction

The microscopic electron transfer theory pioneered by Marcus [136, 137] and Hush [106, 107] has achieved great success in both homogeneous bulk reactions and heterogeneous electrode reactions [141] in terms of predicting more realistic reaction rates than the classical but phenomenological Butler-Volmer equation [13]. Marcus-Hush (MH) theory is applied by assuming quadratic dependence of the free energy of the reactant and product along a configurational reaction coordinate and relating the transition state to the intersection of these parabolas. In application, there is a distinction between solution phase approximations, in which simple analytical expressions can be used, and electrode reactions. At electrodes, the electrochemical reactions must be represented as an integral over all electron energy levels according to a Fermi distribution, leading to so-called Marcus-Hush-Chidsey (MHC) kinetics [134, 42].

The expression for MHC kinetics involves an improper integral requiring numerical evaluation, which has led to the development of a number of simplifying approximations to facilitate its implementation [162, 148, 21, 241], including both extremely accurate [21] and extremely simple [241] approaches. All these simplifying studies have examined the "symmetric" MHC case of electrode kinetics [95] in which the re-

actant and product parabolas have equal curvatures. However, "asymmetric" kinetics have been reported in many experiments [118, 87, 96, 98, 199, 197, 120] in which the symmetric MHC theory requires different reorganization energies to fit the cathodic and anodic reactions.

In his classical paper in 1965, Marcus envisoned the possibility of parabolas with different force constants and proposed an asymmetric theory in Appendix IV [135]. With the aid of numerical estimations, he further concluded that the asymmetric factors in equation (A13) of [135] can be neglected for cases of relatively small driving forces; while for cases of large driving forces, equation (A13) should be replaced by equation (A14a) [135]. Using the electrochemical variant of Marcus's equation (A14a), Compton and coworkers [119, 94, 118], has shown excellent agreement with these experiments using a single reorganization energy (Fig. 1). However, like the Marcus-Hush-Chidsey (MHC) model [42], this "asymmetric-Marcus-Hush" (AMH) model involves evaluation of an improper integral, yet the new cubic term, apparently cannot be easily obtained from Marcus's equation (A13), brings ambiguity in the definition of the integral, thus making practical implementation challenging. And unlike the symmetric case, the authors are unaware of simplifying expressions for evaluating AMH kinetics.

In this paper, we study mathematical characteristics of the aMH model, confirming Compton and coworkers' insights of the range of applicability of the AMH model. We also propose a simple closed form approximation to the AMH model, which can be easily implemented in engineering models with satisfying accuracy.

6.2 Asymmetric-Marcus-Hush Model: Description and Clarification

In this section, we will first introduce the formula for the asymmetric Marcus-Hush kinetics. Then we will demonstrate some characteristics about the formula that lead to a divergent result under certain situations, which leads to a modified model definition.

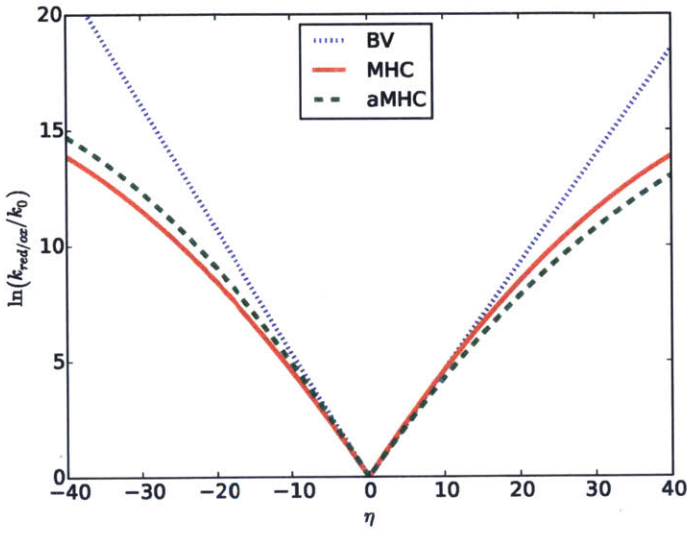

Figure 6-1: Comparison of Butler-Volmer (BV), symmetric Marcus-Hush-Chidsey (MHC), and asymmetric-Marcus-Hush (AMH) kinetics as a function of applied overpotential. Note that at small overpotentials, the AMH rates are well captured by BV with $\alpha \neq \frac{1}{2}$. However, for moderate overpotentials, BV significantly over-predicts the rate.

6.2.1 Asymmetric-Marcus-Hush Model

The symmetric Marcus model for electrode kinetics (MHC) assumes equal force constants for reactants and products, and results in the following expression for the reduction and oxidation rate constants:

$$\begin{aligned} k_{red/ox,s}(\lambda,\eta) &= A\int_{-\infty}^{+\infty} \exp\left(-\Delta G_{red/ox,s}(x)\right)\frac{1}{1+\exp(\mp x)}dx, \\ \Delta G_{red/ox,s}(x) &= \frac{\lambda}{4}\left(1\pm\frac{x+\eta}{\lambda}\right)^2, \end{aligned} \tag{6.1}$$

where A is a pre-exponential constant factor, λ is the dimensionless reorganization energy, η is the dimensionless overpotential, x is the dimensionless integration variable, and $\Delta G_{red/ox,s}$ is the activation energy. When two signs are present, the top refers to reduction and the bottom to oxidation. We note here that this overpotential is defined as the departure of the electrode potential from the formal potential rather than from the equilibrium potential; the latter is a common choice in engineering applications [155, 15]. The AMH model for electron kinetics takes into account the

unequal inner-sphere reorganization energies by introducing a parameter, γ, which describes the difference between inner-shell force constants of oxidized and reduced species in an electrochemical reaction. It is given by the following,

$$\begin{aligned} k_{red/ox,a}(\lambda,\eta,\gamma) &= A\int_{-\infty}^{+\infty}\exp\left(-\Delta G_{red/ox,a}(x)\right)\frac{1}{1+\exp(\mp x)}dx, \\ \Delta G_{red/ox,a}(x) &= \frac{\lambda}{4}\left(1\pm\frac{x+\eta}{\lambda}\right)^2+\gamma\left(\frac{\eta+x}{4}\right)\left[1-\left(\frac{\eta+x}{\lambda}\right)^2\right]+\gamma^2\frac{\lambda}{16}, \end{aligned} \tag{6.2}$$

Note that when $\gamma = 0$, this asymmetric formula reduces to the symmetric MHC model. Importantly, Eq. 6.2 is restricted in applicability based on the truncation of the approximating series by which it was derived [119]. Although the restrictions in relevant parameter ranges vary system to system, conservative estimates require $|\gamma| < 0.35$, $\lambda \gg 1$, and $|\eta| \lesssim 10$ [118]. Nevertheless, $\lambda \gg 1$ is typical for an asymmetric reaction [119].

For the remainder of the analysis, we will focus only on the oxidation rate constant and free energy, as the results are easily repeated for reduction. For ease of notation, we refer to the oxidation rate constant and free energy barrier as simply k_a and ΔG_a.

6.2.2 Clarification of the AMH Formula

This AMH formula has already demonstrated good agreement with experimental data in numerous studies [198, 119, 96] and is becoming increasingly important in understanding electrochemical systems, especially where symmetric MHC kinetics fails. However, mathematically Eq. 6.2 does not converge in its current form. Therefore, we modify the original formula, in agreement with observations made by Compton *et al.* [118]. This change does not affect the results of previous studies and may enable better understanding of this asymmetric kinetic theory.

As has been previously noted, the integrand in Eq. 6.2 is a function with a peak similar to a Gaussian for small x, and numerical evaluation of the integral must be done within some finite x range, typically ± 50 [94]. This integration limit is not solely for computational speed; we will show that the integrand diverges as x goes to either

positive or negative infinity unless γ is exactly zero (the symmetric MHC case).

The cause of the divergence of the integrand is that the nondimensional Gibbs free energy barrier, $\Delta G_a(x)$, is a cubic function of x when γ is non-zero. Depending on the sign of γ, $\Delta G_a(x)$ must tend to negative infinity at either $x = \infty$ or $x = -\infty$ with a speed of $\mathcal{O}(|x|^3)$. The second part of the integrand, $(1 + \exp(x))^{-1}$, which is related to the Fermi distribution, decays no faster than $\mathcal{O}(\exp(-|x|))$. Thus, the integrand diverges at a rate of $\mathcal{O}(\exp(x^3))$, and the integral in Eq. 6.2 must diverge for any $\gamma \neq 0$.

A numerical demonstration is provided in Fig. 6-2. For x within ± 50, the integrand is nearly a Gaussian function with a peak close to zero. However, when $x > 300$, it grows quickly and dominates the peak around zero.

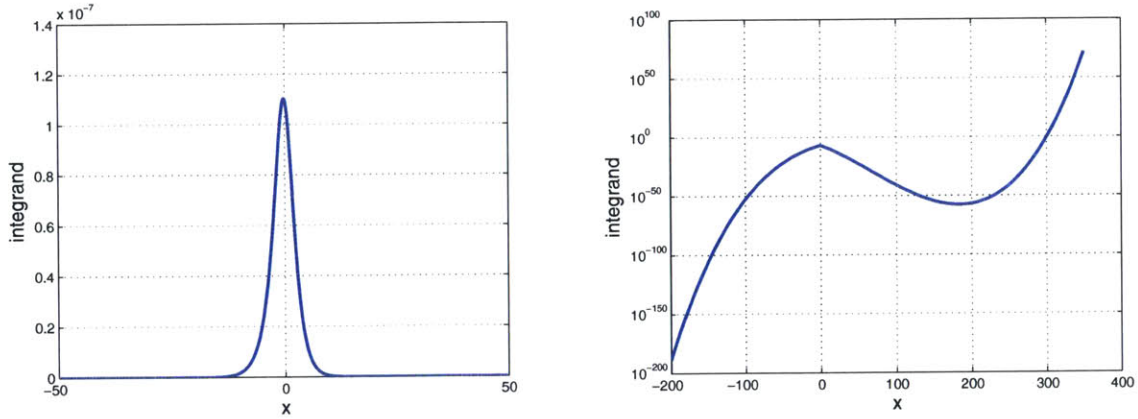

Figure 6-2: Numerical evaluation of the integrand in Eq. 6.2 with $\lambda = 60$, $\gamma = 0.3$ and $\eta = 0$. We see on the right that for $x \gg 50$, the integrand is dominated by the growing cubic term, which results from series truncation in the derivation of Eq. 6.2.

In order to avoid the divergence in Eq. 6.2, instead of integrating over the whole real number axis, we have to restrict the integral within a certain domain $\mathcal{D}$, such that the integrand has a peak within this domain, but takes small enough values on

both boundaries. Thus, we can write the AMH model as,

$$
\begin{aligned}
k_a(\lambda,\eta,\gamma) &= A\int_{\mathcal{D}} \exp\left(-\Delta G_a(x)\right)\frac{1}{1+\exp(x)}dx,\\
\Delta G_a(x) &= \frac{(x-\lambda+\eta)^2}{4\lambda}+\gamma\left(\frac{\eta+x}{4}\right)\left[1-\left(\frac{\eta+x}{\lambda}\right)^2\right]+\gamma^2\frac{\lambda}{16},
\end{aligned}
\tag{6.3}
$$

Unfortunately, the domain $\mathcal{D}$ has to be specified case by case according to the parameter choices. In general, $\mathcal{D}=\{x\in\mathbb{R}|-50\leq x\leq 50\}$ is a very good choice as suggested by Compton's group [118], but a check of the validity of this integral region needs to be done for any new parameter choices.

In addition, for small values of the nondimensional reorganization energy, λ, the peak domain $\mathcal{D}$ is not well separated from the "blow up region". A typical example is shown in Fig. 6-3. In this case, the integral domain $\mathcal{D}$ cannot be clearly defined, and the AMH model in Eq. 6.3 is out of its valid range.

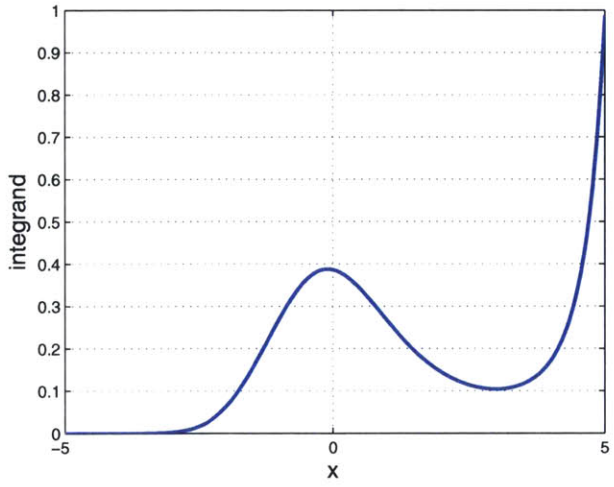

Figure 6-3: Numerical evaluation of the integrand in Eq. 6.3 with parameters $\lambda=1$, $\gamma=0.3$ and $\eta=0$.

In the following sections of our paper, we will always restrict our discussions to the cases in which the integral domain $\mathcal{D}$ can be well defined.

6.3 Closed form Approximation of AMH Theory

In this section, we present a closed form approximation for the domain-restricted AMH formula, Eq. 6.3, based on some empirical observations of the integrand. A mathematical reasoning on the validity of such an approximation is also discussed. Because Eq. 6.3 already relies on an empirical restriction of parameter values, the focus of this work is on providing a useful approximation formula for the applicable parameter ranges rather than formally deriving a uniformly valid approximation.

Compared to the symmetric MHC theory, the asymmetric formula only differs by the cubic term in ΔG_a. Since the integral domain $\mathcal{D}$ normally consists of only a small range of x, we may make some observations of the quadratic term and the cubic term within this range.

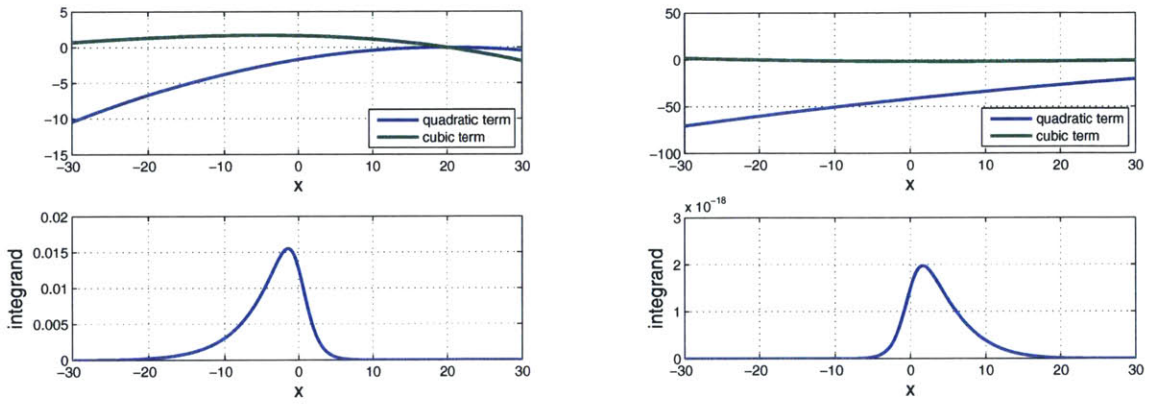

Figure 6-4: Comparisons of the quadratic term and the cubic term in Eq. 6.3 within the integral domain $\mathcal{D}$ with parameters $\lambda = 60$, $\gamma = 0.3$. The nondimensional overpotential η is chosen to be 40 (left) and -40 (right).

Typically, the cubic term varies considerably less than the quadratic term within the peak region of the integrand. Two examples are shown in Fig. 6-4. Therefore, one possible choice for approximating Eq. 6.3 is to treat the cubic term as independent of x over the integral domain $\mathcal{D}$. This is mathematically equivalent to taking only the first term of the Maclaurin series of the cubic term, and neglecting all higher order

terms. Then we get,

$$\begin{aligned}\Delta G_a(x) &= \frac{(x-\lambda+\eta)^2}{4\lambda} + \gamma\left(\frac{\eta+x}{4}\right)\left[1-\left(\frac{\eta+x}{\lambda}\right)^2\right] + \gamma^2\frac{\lambda}{16} \\ &\approx \Delta G_s(x) + \gamma\left(\frac{\eta}{4}\right)\left[1-\left(\frac{\eta}{\lambda}\right)^2\right] + \gamma^2\frac{\lambda}{16},\end{aligned} \tag{6.4}$$

where ΔG_s is the corresponding free energy function of the symmetric MHC theory in Eq. 6.1. Since the cubic term is independent of x, it can be moved out of the integral. Then we obtain the approximated reaction rate,

$$\begin{aligned}k_a(\lambda,\eta,\gamma) &\approx A\exp\left\{-\gamma\left(\frac{\eta}{4}\right)\left[1-\left(\frac{\eta}{\lambda}\right)^2\right] - \gamma^2\frac{\lambda}{16}\right\}\int_{\mathcal{D}}\exp\left(-\Delta G_s(x)\right)\frac{1}{1+\exp(x)}dx \\ &= \exp\left\{-\gamma\left(\frac{\eta}{4}\right)\left[1-\left(\frac{\eta}{\lambda}\right)^2\right] - \gamma^2\frac{\lambda}{16}\right\}k_s(\lambda,\eta),\end{aligned} \tag{6.5}$$

where $k_s(\lambda,\eta)$ is the corresponding reaction rate of the symmetric MHC kinetics, which can be approximated a number of ways as discussed above. For simplicity, we apply our previous approximation for the symmetric MHC kinetics formula here and finally obtain a closed form approximation for the AMH theory [241],

$$k_{red/ox,a}(\lambda,\eta,\gamma) \approx A\exp\left\{-\gamma\left(\frac{\eta}{4}\right)\left[1-\left(\frac{\eta}{\lambda}\right)^2\right] - \gamma^2\frac{\lambda}{16}\right\}\frac{\sqrt{\pi\lambda}}{1+\exp(\pm\eta)}\operatorname{erfc}\left(\frac{\lambda-\sqrt{1+\sqrt{\lambda}+\eta^2}}{2\sqrt{\lambda}}\right). \tag{6.6}$$

where the double sign corresponds to reduction (above) and oxidation (below). The reduction and oxidation formulas differ only in the substitution of the reduction/oxidation symmetric rate constant for k_s.

The approximation formula in Eq. 6.6 works well when $|\gamma| < 0.35$, in agreement with the valid region suggested by Compton and coworkers [118]. In addition, this requires $\lambda \gg 1$ because of the integral domain validation requirement. However, $\lambda \gg 1$ is typical for an asymmetric reaction [119]. Very importantly, the absolute value of the nondimensional overpotential η should not exceed the value of nondimensional reorganization energy λ, $|\eta| < \lambda$, consistent with Compton and coworkers' observations [118]. Finally, we consider the choice of the approximation for k_s. We note that

the approximation for symmetric MHC kinetics as used in Eq. 6.6 is less accurate for large λ and $\eta \approx 0$ [241]. However, over the entire relevant parameter space, small errors in η ($\lesssim$ 15 mV) correspond to the same magnitude of error as introduced by using the chosen uniformly valid approximation. Thus, it is unlikely that practical applications will require more accuracy for the symmetric part. Nevertheless, more accurate choices for k_s can be implemented instead [21].

6.4 Numerical Study

In this section, we will numerically compare our approximation formula in Eq. 6.6 to the numerical integration of the original AMH formula in Eq. 6.3 with different choices of γ and η. We will also demonstrate limitations of this approximation in the range of large η.

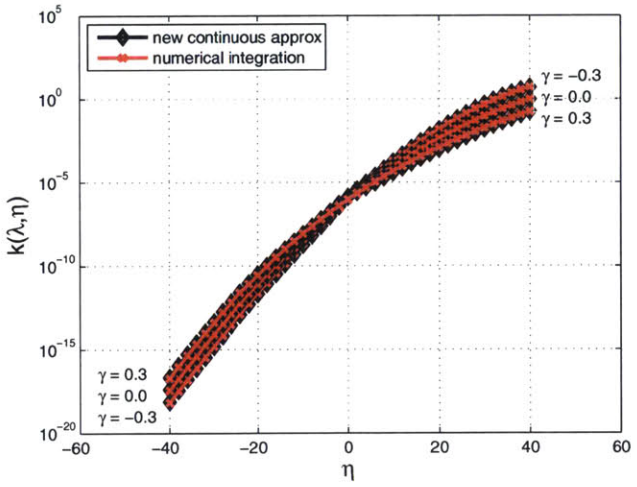

Figure 6-5: Comparisons of asymmetric reaction rates by numerically evaluating Eq. 6.3 and a direct calculation of the approximation in Eq. 6.6. Here, $\lambda = 60$ (roughly 1.5 eV at room temperature).

In Fig. 6-5, we compare the numerically integrated results of the reaction rate $k_a(\lambda, \eta, \gamma)$ to the approximated values obtained from Eq. 6.6. Even though the reaction rate varies by about 20 orders of magnitude over this parameter range, the approximations show good agreement with the numerical results, and accurately cap-

ture the effects of non-zero γ.

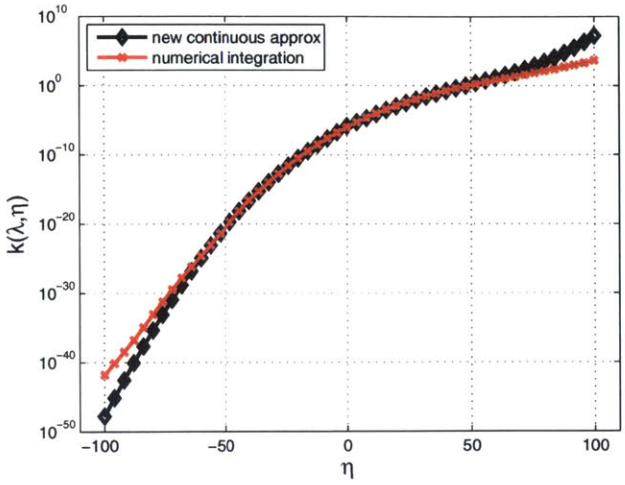

Figure 6-6: Comparisons of asymmetric reaction rates by numerically evaluating Eq. 6.3 and a direct calculation of approximation in Eq. 6.6. As in Fig. 6-5, $\lambda = 60$. The approximation values differ significantly from the true values when $|\eta| > \lambda$.

However, as mentioned in the previous section, this approximation loses its accuracy when $|\eta|$ gets larger than λ. A numerical demonstration in Fig. 6-6 shows that when $|\eta| > \lambda$, the approximation can be several orders off from the true value. Therefore, the application of approximation formula in Eq. 6.6 should be limited to the range $|\eta| < \lambda$. Nevertheless, as noted by Compton and co-workers, the original AMH formula is generally only accurate for $|\eta| < \lambda$ [118], so this restriction does not further limit the use of the developed approximation.

6.5 Conclusion

The asymmetric Marcus-Hush (AMH) formula, which has recently been shown to have excellent agreement with experimental results has been approximated with a simple, closed form solution, suitable for implementation in practical and large-scale engineering models. The new approximation relies on the observation that the integrand in the original expression can be approximated as having a nearly-constant factor over relevant parameter regions and associated integration limits. Then, using

a result from a previous study to approximate the remaining improper integral, we conclude with the final, closed form result. As noted by Compton and co-workers, the original AMH, when used for $|\eta| \lesssim 1$, is relatively similar to the Butler-Volmer equation with $\alpha \neq \frac{1}{2}$ [118], which provides an alternative to the formula presented here. However, doing so neglects all curvature in the Tafel plot, which becomes significant even at moderate overpotentials (Fig. 6-1), so Eq. 6.6 (or Eq. 6.5) still provides a practical, accurate approximation for AMH kinetics over the entire relevant range of overpotentials.

Chapter 7

Conclusions and Future Research

7.1 Conclusions

In the initial half of this work, we focused on the dynamical system of bulk ion transport in intercalation particles. We first developed an efficient numerical algorithm for solving the nonlinear diffusion equation, which is the core of single-particle battery models in electrochemical engineering. This new numerical method enabled us for the first time to study in detail the full phase separation dynamics of the Cahn-Hilliard reaction model, which is a new theoretical framework for modeling the thermodynamics and electrokinetics of a single intercalation particle, in one-dimensional spherical geometry. We also extended this Cahn-Hilliard reaction model to a more complicated two-dimensional case and explored the effects of the surface electron-conducting coating, since such a coating layer has been experimentally proven to be important in battery performance.

In the second half of this thesis, we mainly worked on the Marcus electron transfer theory, which can be applied to the modeling of heterogeneous electron transfer at electrodes in batteries. Despite its huge successes in predicting many reaction kinetics, it has remained unknown in electrochemical engineering, possibly due to its complicated mathematical form. We started with the symmetric Marcus-Hush-Chidsey model, and by applying several asymptotic techniques, we provided a more practical simple closed-form approximation formula for this theory. Then we extended

that result to a more complex asymmetric Marcus-Hush kinetics model. In addition to providing a simple approximation formula, we were also able to mathematically illustrate some reasoning about the model limitations given in the original literature.

7.2 Future research

For future research in this field, several possible exploration directions can be considered.

In the single-particle model, one important feature that has been neglected in this thesis is the elastic strain. The elastic strain is already known to be important in battery dynamics, but coupling the elastic equations to the Cahn-Hilliard reaction model is, as yet, too difficult to solve numerically. A fast computational method solving such a big system will be essential to study this model and facilitate fitting the model outputs to experimental data.

The electron transport within the surface coating could also be better modeled. As the current linear diffusion oversimplifies the charge-conducting process within this region, future research should consider the electric field distribution and potential drop within the coating layer.

As we now have good approximations to both symmetric and asymmetric Marcus electron transfer theories, they should replace the current phenomenological Butler-Volmer equation in the single particle surface electron transfer model. It would be interesting to study the overall dynamical behavior of the single-particle system with this more realistic surface reaction rate model, especially with high charging/discharging rates.

Furthermore, the current asymmetric Marcus-Hush charge transfer theory is subject to some mathematical ambiguities in its definition. It would be helpful to rederive this whole asymmetric model from the beginning to provide a more rigorous foundation than its current form does.

Once we have all these new features in the microscopic single particle system to accurately model the behavior at the particle level, we will be able to couple

that microscopic system to the macroscopic porous electrode theory to fully simulate real battery dynamics. We believe that, one day, when we have better and better microscopic single particle models, we will be able to replicate the experimental results using the model without any data fitting.

Appendix A

Unification of Algorithms for Minimum Mode Optimization

A.1 Introduction

An important challenge in chemical and materials science is the simulation of the dynamics of systems over long time scales. Most chemical reactions can not be simulated directly with traditional molecular dynamics (MD) simulations due to the limited accessible time scales. However, using the harmonic approximation to transition state theory [222, 216], which is generally valid for solid state systems at moderate temperature, any reaction rate can be determined from the reactant and transition states. Once these states are located, the dynamics of rare-event systems can be evolved by a kinetic Monte Carlo algorithm over time scales much longer than is possible with MD. Thus the challenge of studying such chemical reactions can be transformed into the task of searching for the saddle points (transition states) connected to a given minimum (reactant). Due to the high dimensionality and expensive force evaluation of chemical systems, great efforts have been made in developing efficient saddle point searching algorithms. A family of these algorithms, called minimum-mode following algorithms, employ the following evolution equation,

$$\dot{x} = F(x) - 2(\hat{\tau}^{\intercal} F(x))\hat{\tau}, \tag{A.1}$$

where x is the position vector, $-F(x)$ is the gradient of the potential energy surface $V(x)$, and $\hat{\tau}$ is the unit vector along the minimum curvature mode direction. We denote $\mathbf{H} = \nabla^2 V$ and $\hat{\tau}$ as the unit eigenvector of $\mathbf{H}$ with the minimum eigenvalue. When $\mathbf{H}$ has only one negative eigenvalue, the above equation reverses the force along that eigenvector and converges to a first-order saddle point. The efficiency of the algorithm relies on an efficient update of $\hat{\tau}$.

In this paper, we focus on the $\hat{\tau}$ updating algorithms that avoid calculating the Hessian matrix $\mathbf{H}$, since it is typically too expensive to calculate directly for large chemical systems of interest. We examine several existing methods for estimating $\hat{\tau}$, including the Lanczos [125] method as used in the activation relaxation technique (ART-nouveau) [132], the dimer method [92, 100, 112], Raleigh-Ritz minimization [103] as used in the hybrid eigenvector following method [151], the shifted power iteration method as used in gentlest ascent dynamics [70], and locally optimal block preconditioned conjugate gradient (LOBPCG) [126]. Here, these methods are unified into the same mathematical framework so that their relative theoretical efficiencies can be understood.

This paper is structured as follows. In Sec. A.2 the Lanczos method is presented and the essential idea of the Krylov subspace behind the algorithm. Another widely used numerical scheme, the dimer method, is presented in Sec. A.3. We show that the dimer method searches for the lowest eigenvector of the Hessian within the same Krylov subspace as the Lanczos algorithm. In Sec. A.4 we present the power iteration method with Rayleigh quotient shift. This method is shown to be a special restarted case of the Lanczos algorithm for which the convergence rate is significantly slower in high dimensional space. In Sec. A.5 we numerically compare the efficiency of the Lanczos algorithm, the dimer method coupled with three different optimizers, and the shifted power iteration method. Finally, we conclude in Sec. A.6 that the performance of methods such as the dimer, which are limited to the same Krylov subspace as the Lanczos method, do not exceed its efficiency for finding the lowest mode.

A.2 Lanczos Algorithm

The Lanczos algorithm is a specialized Arnoldi iteration method of eigenvalue calculations for symmetric matrices.[125] Before discussing the Lanczos algorithm, we first restate the minimum mode eigenvalue problem as a minimization problem in Theorem 1, and then review the concept of the Krylov subspace and present the Lanczos algorithm based on Krylov subspace projection and search. In this section, we assume that the smallest eigenvalue has multiplicity 1.

Theorem 1. *Given a symmetric matrix* $\mathbf{H} \in \mathbb{R}^{m \times m}$, v *is the eigenvector associated with the smallest eigenvalue* λ, *if and only if* v *solves the minimization problem,*

$$\min_{b \in \mathbb{R}^m \setminus \{0\}} \frac{b^\intercal \mathbf{H} b}{b^\intercal b}. \tag{A.2}$$

Proof. Since $\mathbf{H}$ is a symmetric matrix, all eigenvectors $v_1, v_2, \cdots, v_m$ form an orthogonal basis of the space $\mathbb{R}^m$ and all eigenvalues of $\mathbf{H}$ are real numbers. We can write $b = \sum_i a_i v_i$, then we have,

$$\frac{b^\intercal \mathbf{H} b}{b^\intercal b} = \frac{\sum_i \lambda_i a_i^2}{\sum_i a_i^2} \tag{A.3}$$

This function takes its minimum value when b is equivalent to the eigenvector v. Thus, v solves the minimization problem.

The other side of the statement follows from the uniqueness of the eigenvector corresponding to the smallest eigenvalue. □

Remark 1. *Such an optimal solution* v *must be unique also due to the uniqueness of the eigenvector associates with the smallest eigenvalue.*

Having transformed the eigenvalue problem to a minimization problem, the minimization problem can be solved as follows. We first solve the optimization problem in a low dimension subspace, which can be done more easily than in the original space $\mathbb{R}^m$. Then we consider the optimal solution in a space with one more dimension to find a better solution. As we move to higher and higher dimensional subspaces, this optimal solution will converge to the true solution. Here the low dimensional subspace we will use is the Krylov subspace, $\mathcal{K}_n$, which is defined as in Remark 2.

Remark 2. *The n-th order Krylov subspace $\mathcal{K}_n$ generated by a square matrix $\mathbf{H} \in \mathbb{R}^{m\times m}$ and a nonzero vector $v \in \mathbb{R}^m$ is defined as,*

$$\mathcal{K}_n = span\{v, \mathbf{H}v, \mathbf{H}^2v, \cdots, \mathbf{H}^{n-1}v\}. \tag{A.4}$$

When n is smaller than the rank r of the matrix $\mathbf{H}$, $\mathcal{K}_n$ is a n dimensional space; when n is greater or equal to r, $\mathcal{K}_n$ is an r dimensional space. The product $\mathbf{H}v$ is calculated by the following approximation,

$$\mathbf{H}v = \frac{F(x) - F(x+v)}{||v||} + \mathcal{O}\left(||v||^2\right). \tag{A.5}$$

To solve the minimization problem in the Krylov subspace, a set of orthogonal basis is utilized. This basis can be obtained by the Gram-Schmidt process iteratively as shown in Refs. [178, 208]. We define such a basis for a n-dimensional Krylov subspace $\mathcal{K}_n$ as $\mathbf{Q}_n = [q_1, q_2, \cdots, q_n] \in \mathbb{R}^{m\times n}$. Therefore, any vector $b \in \mathcal{K}_n$ can be represented by, $b = \mathbf{Q}_n r$, where $r \in \mathbb{R}^n$. Then the minimization problem projected on a Krylov subspace $\mathcal{K}_n$ can be solved, as shown in Theorem 2.

Theorem 2. *$\mathbf{Q}_n r$ solves the minimization problem on the Krylov subspace $\mathcal{K}_n$*

$$\min_{b\in\mathcal{K}_n\setminus\{0\}} \frac{b^\intercal \mathbf{H} b}{b^\intercal b}, \tag{A.6}$$

if r is the eigenvector corresponding to the smallest eigenvalue of the matrix $\mathbf{Q}_n^\intercal \mathbf{H}\mathbf{Q}_n$.

Proof. Since any vector $b \in \mathcal{K}_n$ can be written as, $b = \mathbf{Q}_n r_b$

$$\frac{b^\intercal \mathbf{H} b}{b^\intercal b} = \frac{(\mathbf{Q}_n r_b)^\intercal \mathbf{H}\mathbf{Q}_n r_b}{(\mathbf{Q}_n r_b)^\intercal (\mathbf{Q}_n r_b)} = \frac{r_b^\intercal (\mathbf{Q}_n^\intercal \mathbf{H}\mathbf{Q}_n) r_b}{r_b^\intercal r_b}. \tag{A.7}$$

By Theorem 1, the eigenvector r associated with the smallest eigenvalue of the matrix $\mathbf{Q}_n^\intercal \mathbf{H}\mathbf{Q}_n$ solves this minimization problem. Therefore, the vector $\mathbf{Q}_n r$ solves the original optimization problem in the space $\mathcal{K}_n$. □

Remark 3. *By construction of the orthogonal basis $\mathbf{Q}_n$, the matrix $\mathbf{Q}_n^\intercal \mathbf{H}\mathbf{Q}_n$ is an upper Hessenberg matrix, e.g., an upper triangular matrix plus a nonzero first sub-*

diagonal. It is also symmetric since $\mathbf{H}$ *is symmetric and* $\mathbf{Q}_n$ *is an orthogonal basis. These two properties confirm that the matrix* $\mathbf{Q}_n^{\intercal}\mathbf{H}\mathbf{Q}_n$ *is tridiagonal.*

Finally, the eigenvalue problem of a unknown matrix $\mathbf{H}$ is transformed to a iterative series of calculations to find the smallest eigenvalue of a known low dimensional matrix $\mathbf{Q}_n^{\intercal}\mathbf{H}\mathbf{Q}_n$, which can be done efficiently, for example, by the QR algorithm. In theory, this scheme is guaranteed to converge if n grows to the rank of the matrix $\mathbf{H}$, but in practice, the convergence will be faster than this bound [177, 115].

A.3 Dimer Method

The dimer method is another iterative algorithm for minimum mode finding [92]. With improvements in the implementation [171, 163, 100, 112], the dimer method has become widely used in calculating chemical reaction rates with the forces evaluated from self-consistent field methods.

We note that the Raleigh-Ritz optimization method used in hybrid eigenvector following, as developed by the Wales group [151], is based upon the same finite-difference gradient of the lowest eigenvector that is used in the dimer method. So while the methods are described using different language and have some minor differences in their implementation, they are equivalent for the purposes of this analysis. The same approach was also used previously by Voter to construct a bias potential for the acceleration of MD in his hyperdynamics method[217].

In this section, we present the dimer method within the same theoretical framework as the Lanczos algorithm. Numerical comparisons have been previously made between these two algorithms [163], but now, under this mathematical framework, we can compare their relative theoretical efficiency.

In the dimer method, the minimum curvature mode is determined by rotating a pair of images separated by a small distance $||v||$ according to the torque acting on the dimer. The torque is the force difference divided by the distance, and thus has the same form as $\mathbf{H}v$ in Eq. A.5. Rotating along the torque direction is the mechanism by which the dimer method finds the minimum curvature mode in a specific subspace

of the Krylov subspace.

At each iteration, the new direction τ that minimizes $\frac{\tau^\intercal \mathbf{H}\tau}{\tau^\intercal\tau}$ is found in the plane spanned by $\{v, \mathbf{H}v\}$, assuming the simplest case in which the SD direction is taken for the rotation plane. A second direction Θ is then constructed perpendicular to v to form an orthogonal basis set $\mathbf{Q}_2 = [v, \Theta]$, reducing the optimization problem to two dimensions,

$$\Theta = \mathbf{H}v - (v^\intercal \mathbf{H}v)v, \tag{A.8}$$

$$\mathbf{A} = \mathbf{Q}_2^\intercal \mathbf{H}\mathbf{Q}_2 = \begin{pmatrix} v^\intercal \mathbf{H}v & v^\intercal \mathbf{H}\Theta \\ \Theta^\intercal \mathbf{H}v & \Theta^\intercal \mathbf{H}\Theta \end{pmatrix}. \tag{A.9}$$

Here, calculating $\mathbf{H}\Theta$ requires a second force evaluation, $F(x+\Theta)$. The 2×2 matrix $\mathbf{A}$ can then be diagonalized. The eigenvector τ, which is expressed as $\tau = r_1 v + r_2 \Theta$, is then the starting point of the next iteration. Note that

$$\mathbf{H}\tau = r_1 \mathbf{H}v + r_2 \mathbf{H}\Theta, \tag{A.10}$$

can be obtained without any further force evaluation since $\mathbf{H}v$ and $\mathbf{H}\Theta$ are already known, as pointed out in Ref. [112]. The minimization is repeated in a sequence of two dimensional spaces: $\mathrm{span}\{v, \mathbf{H}v\}, \mathrm{span}\{\tau, \mathbf{H}\tau\}, \cdots$, where $\mathrm{span}\{v, \mathbf{H}v\}$ is the Krylov subspace $\mathcal{K}_2$. Also because

$$\mathbf{H}\tau = (r_1 - r_2(v^\intercal \mathbf{H}v))\mathbf{H}v + r_2 \mathbf{H}^2 v, \tag{A.11}$$

τ and $\mathbf{H}\tau$ are in the Krylov subspace $\mathcal{K}_3 = \mathrm{span}\{v, \mathbf{H}v, \mathbf{H}^2 v\}$. After the n-th iteration, n force evaluations have been made, which is the same number as in the Lanczos method. However, each two dimension space considered in the dimer method is a subspace of $\mathcal{K}_{n+1}$. Therefore, the dimer method convergence is theoretically limited by that of the Lanczos algorithm.

In previous descriptions of the dimer method, the above procedure was done by finding a unit vector $\hat{r} \in \mathbb{R}^2$ to minimize $\hat{r}^\intercal \mathbf{A}\hat{r}$, which is exactly the dimer energy

in Ref. [92]. The connection between minimizing the dimer energy and solving the eigenvector problem of Eq. A.9 can be seen by expanding $\hat{r}$ by the unit eigenvectors of $\mathbf{A}$,

$$\hat{r}^{\intercal}\mathbf{A}\hat{r} = (a_x\hat{v}_x + a_y\hat{v}_y)^{\intercal}\mathbf{A}(a_x\hat{v}_x + a_y\hat{v}_y) = a_x^2\lambda_x + a_y^2\lambda_y, \tag{A.12}$$

where λ_x and λ_y are eigenvalues of the matrix $\mathbf{A}$.

Theorem 3. *The steepest descent dimer method is equivalent to the Lanczos algorithm with restarts every two steps; its theoretical efficiency must be lower than the Lanczos algorithm.*

When the rotation plane is determined by algorithms based on the previous search direction Θ, as in the conjugate gradient (CG) algorithm, the dimer method is more efficient but remains under the limit of the Lanczos method. The Broyden-Fletcher-Goldfarb-Shanno (BFGS) algorithm for updating Θ, as well as the limited memory version (L-BFGS),[159] are even more efficient. When the initial Hessian is set as a constant times the identity matrix (the standard case in practice), BFGS/L-BFGS is also searching for the lowest mode in the subspace of $\mathcal{K}_{n+1}$ at iteration n. The LOBPCG method performs the minimization in a three dimensional subspace, with one extra direction that is a linear combination of the previous directions [126]. The search space of LOBPCG is therefore still a subspace of the Krylov subspace, and its theoretical efficiency also cannot exceed the Lanczos limit.

A.4 Power Iteration Method with a Rayleigh Shift

Another method for finding the lowest mode is the power iteration method, which has been employed in some recent saddle point searching algorithms [70, 179]. In this section, we present the motivation and mechanism of the power iteration method with a Rayleigh shift, and prove the convergence of this method. Similar to the dimer method, we demonstrate that the search space of this method is contained in the Krylov subspace $\mathcal{K}_n$ for the minimization problem of Eq. A.2.

A.4.1 Derivation of the shifted power iteration method

The power iteration method is an iterative eigenvector computation method which can be described as,

$$v_{i+n} = \frac{\mathbf{H}v_n}{\|\mathbf{H}v_n\|}, \tag{A.13}$$

where $\mathbf{H}$ is a square matrix with eigenvalues $|\lambda_1| > |\lambda_2| \geq |\lambda_3| \geq \cdots$. In this scheme, v_i will converge to the eigenvector associated with eigenvalue λ_1 as $i \to \infty$ [208].

We already know that all eigenvalues of our Hessian matrix $\mathbf{H}$ are on the real axis. Moreover, if λ is an eigenvalue of $\mathbf{H}$ associated with the eigenvector v, and $\mathbf{I}$ is the identity matrix, then for any constant $a \in \mathbb{R}$, $a - \lambda$ is the eigenvalue of a new matrix $a\mathbf{I} - \mathbf{H}$ with eigenvector v. As a result, we can linearly shift the desired eigenvalue to become the eigenvalue with greatest absolute value without changing the eigenvector. Therefore, the power iteration method will converge to our desired eigenvector if we find such a shift.

To pick an appropriate shift, a, we use the current maximum absolute value of Rayleigh quotients at each iteration plus a small increment,

$$a_n = \max\{|\frac{v_1^\intercal \mathbf{H} v_1}{v_1^\intercal v_1}|, |\frac{v_2^\intercal \mathbf{H} v_2}{v_2^\intercal v_2}|, \cdots |\frac{v_n^\intercal \mathbf{H} v_n}{v_n^\intercal v_n}|\} + \log n. \tag{A.14}$$

The $\log n$ term is added to prevent the case where the shift exactly equals to $\frac{\lambda_n - \lambda_1}{2}$, even though this scenario is unlikely. With the dynamical update of the shift constant a_n according to Eq. A.14, the modified power iteration method can be described,

$$v_{n+1} = \frac{(a_n\mathbf{I} - \mathbf{H})v_n}{\|(a_n\mathbf{I} - \mathbf{H})v_n\|}. \tag{A.15}$$

Theorem 4. *The iterative algorithm shown in Eq. A.15 will converge to the eigenvector associated with the smallest eigenvalue of* $\mathbf{H}$*, if this eigenvalue has multiplicity* 1.

Proof. Let λ_1 be the smallest eigenvalue and λ_2 the second smallest one, by our assumption smallest eigenvalue has multiplicity 1, $\lambda_1 < \lambda_2$.

The Rayleigh quotient is bounded by the maximal absolute value of eigenvalues,

which we assume to be L. Let v be the true eigenvector we want to obtain, then the convergence rate of the v_n depends on the ratio of two eigenvalues which is with largest absolute values [208]. The convergent rate is,

$$\|v_n - v\| = \mathcal{O}(\prod_k \frac{L + \log k - \lambda_1}{L + \log k - \lambda_2}) \to 0, \tag{A.16}$$

as $n \to \infty$, which proves the convergence of the algorithm. □

A.4.2 Krylov Subspace of the Shifted Power Iteration Method

While the convergence of the power iteration method with a Rayleigh shift is guaranteed in principle, the convergence is slow in practice. The resulting v_n at the n-th iteration from this method is located in the Krylov subspace $\mathcal{K}_n$, which is defined in Remark 2. We will prove this statement in Lemma 1 in order to conclude that the shifted power iteration method will always converge slower than the Lanczos algorithm.

Lemma 1. *For any $n > 0$, $v_n \in \mathcal{K}_n$, where $\mathcal{K}_n = span\{v_0, \mathbf{H}v_0, \cdots, \mathbf{H}^n v_0\}$.*

Proof. We will prove this by induction.

When $n = 1$, $v_1 = (a_1\mathbf{I} - \mathbf{H})v_0 = a_1 v_0 + \mathbf{H}v_0 \in \mathcal{K}_1$.

Given $v_n \in \mathcal{K}_n$, we can write $v_n = \sum_{i=0}^{n} c_i \mathbf{H}^i v_0$. Then,

$$v_{n+1} = (a_n\mathbf{I} - \mathbf{H})v_n = (a_n\mathbf{I} - \mathbf{H}) \sum_{i=0}^{n} c_i \mathbf{H}^i v_0 \in \mathcal{K}_{n+1}. \tag{A.17}$$

Thus, the statement holds for any general $n > 0$. □

Since the eigenvalue problem can be taken as a minimization problem as shown in Theorem 1, the power iteration solution is within the same Krylov subspace as the Lanczos algorithm, with the same number of iterations. Therefore, the convergence rate of the power iteration method is limited by the Lanczos algorithm.

A.5 Numerical Test

In the previous sections, we have compared the theoretical efficiencies of the Lanczos algorithm, dimer method, and the shifted power iterative method. We proved the convergence rates of the later two methods are bounded by the Lanczos algorithm due to the restriction of a smaller search space than Lanczos at each step. In this section, we conduct a numerical comparison to demonstrate our results in practice.

The convergence rates of the algorithms are compared for Lennard Jones clusters with 38 atoms. Geometry configurations are chosen randomly near saddle points where the existence of one negative eigenvalue of the Hessian is guaranteed. A random direction is used as an initial guess for each of the minimum-mode searches. More details of the benchmark system are discussed elsewhere [43, 1]. The Lanczos method is implemented with full reorthogonalization, which is faster by one step on average than without reorthogonalization. The dimer method is implemented with three optimizers for determining the rotation plane: SD, CG, and BFGS. The initial Hessian for BFGS is taken as $\alpha\mathbf{I}$, where α is set to be 60 $\text{eV}/^2$ and $\mathbf{I}$ is the identity matrix. Other α values tested did not give significantly better results. When the rotation direction from the BFGS become almost perpendicular (within 3°) of the SD direction, the BFGS is restarted with the initial Hessian. No parameters are needed for the other methods. All the methods are implemented in the TSASE software [2, 3].

The angle between the estimated lowest mode and the true minimum mode is plotted at each iteration in a typical run in Fig. A-1. Clearly the Lanczos method is the fastest, while the shifted power iteration and the SD dimer are significantly slower. The CG dimer and the BFGS dimer are marginally slower than Lanczos. The similar convergence trends of these three methods indicates some commonality between them.

The two slowest methods were not considered for further study, but for the three competitive methods, 200 minimum mode searches were run at different cluster geometries for a more statistically significant comparison. A summary of the results is presented in Table A.1. The convergence criteria is that the angle to the true

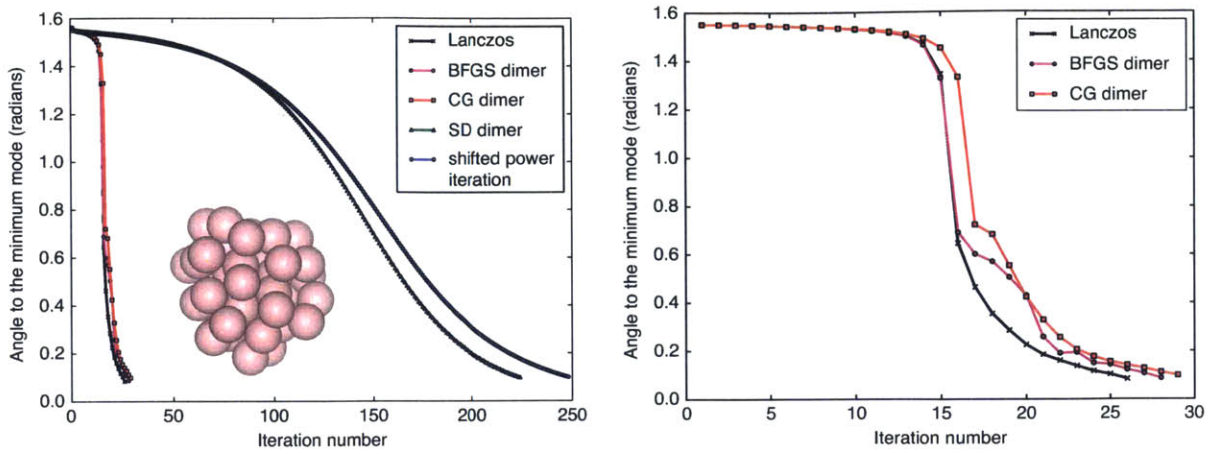

Figure A-1: The angle, in radians, towards the true minimum mode as a function of iteration number (left) and a zoom in of the region of relevance for the Lanczos, BFGS dimer, and CG dimer methods (right).

Table A.1: Steps to Convergence.

Method	N	max N	min N
Lanczos	25	54	13
BFGS Dimer	27	65	13
CG Dimer	29	80	13

minimum mode is smaller than 0.14, which corresponds to an overlap (dot product of unit vectors) greater than 0.99. We did not observe any case in which the dimer method converges faster than Lanczos, although in some cases they converge at the same rate. Typically, the BFGS dimer is faster than the CG dimer when a reasonable initial Hessian value, α, is chosen. These numerical results are consistent with our theoretical conclusions.

A.6 Conclusion

In summary, we have presented three classes of minimum mode searching algorithms, the Lanczos algorithm, dimer method, and the shifted power method, under the same mathematical framework of minimization in the Krylov subspace. With a theoretical

understanding of these methods, we can see the dimer and shifted power methods are searching in a subspace of the Krylov subspace for which the Lanczos method explicitly finds the minimum curvature mode. This leads to the conclusion that with the same number of evaluations of the potential gradient, the Lanczos algorithm will theoretically converge no slower than the other two classes of methods. The result of this research can provide theoretical guidance for any future improvements to methods for finding the minimum curvature mode. Key to methods that can outperform the Lanczos algorithm will be the determination of subspaces that are outside of the Krylov subspace.

Appendix B

Synchrony and Periodicity in Excitable Neural Networks with Multiple Subpopulations

B.1 Introduction

The study of oscillator synchronization has made a significant contribution to the understanding of the dynamics of real biological systems [29, 149, 130, 169, 85, 81, 50, 210, 71, 111, 211, 37, 90, 166], and has also inspired many ideas in modern dynamical systems theory. See [193, 170, 225] for reviews. The prototypical model in mathematical neuroscience is a system of "pulse-coupled" oscillators, that is, oscillators that couple only when one of them "fires". More concretely, each oscillator has a prescribed region of its phase space where it is active, and only then does it interact with its neighbors. There has been a large body of work on deterministic pulse-coupled networks [116, 80, 209, 214, 28, 205, 215, 36, 114, 169, 149, 185], mostly studying the phenomenon of synchronization on such networks.

In [62, 63], the first author and collaborators considered a specific example of a network containing both refractoriness and noise; the particular model was chosen to study the effect of *synaptic failure* on the dynamics of a neuronal network. What was

observed in this class of models is that when the probability of synaptic success was taken small, the network acted as a stationary process with a low degree of correlation in time; when the probability of synaptic success was taken large, the system exhibited synchronous behavior that was close to periodic. Both of these behaviors are, of course, expected: strong coupling tends to lead to synchrony, and weak coupling tends not to do so. The most interesting observation was that for intermediate values of the coupling, the network could support both synchronized and desynchronized behaviors, and would dynamically switch between the two. This was explained in [63] by showing that the large network limit was, for certain parameters, multistable. Then, large but finite networks switch stochastically between the attractors of the limiting system.

One unusual aspect of the large network limit, or mean-field system, of [62, 63] is that it is a *hybrid* system: a system of a continuous flow coupled to a map of the phase space. This system has piecewise continuous trajectories that jump at prescribed times. This is due to the fact that the interneuronal connections in the model undergo cascades, where the firing of one neuron can cause other neurons to fire, which cause other neurons to fire, and so on, causing an avalanche of activity throughout the network. This sort of neural activity has been observed experimentally in [18, 19, 186] and a model of the type considered in this paper was matched to experimental data in [77]. Since these cascading events are on the order of the size of the network, yet happen quickly, they correspond to discontinuities in the dynamics, leading to the hybrid character of the dynamics. Moreover, as we argue below, the model we consider here is a prototypical model of cascading neuronal dynamics, and is in some sense the simplest model possible of this type. The model we analyze here is a cascading version of the three-state excitable network model analyzed in [172, 173, 154] (although one notes that the details of the analysis differ significantly).

In this paper, we consider a generalization of the mean-field model that allows for several independent subpopulations with different intrinsic firing rates. We show that this model has the property that for sufficiently small interneuronal coupling, the system has a globally attracting fixed point, and for sufficiently large interneuronal coupling, the system has a globally attracting periodic orbit. We also give bounds on

the parameter ranges of validity for each of the two behaviors. Moreover, we make the surprising observation that all of these attractors exist no matter how many subpopulations exist, and how much their firing rates differ — in particular, we show that the critical coupling parameter for the existence of a globally attracting limit cycle does not depend on the firing rates, or relative sizes, of the subpopulations in the network.

We also connect the model studied in this paper to the stochastic cascading neural system considered in [63]. Since this result follows with only minor changes from the theorems in [63], we present a short argument of the connection between the stochastic model and its mean-field equation, but only for completeness.

B.2 Model definition

B.2.1 Overview of model

We consider a network of neurons which is coupled all-to-all and which all coupling is excitatory. We also assume that the interneuronal coupling is much faster than the other timescales in the system, so that the interaction between different neurons happens in zero time. Each neuron can be in one of three states: "refractory", "excitable", and "firing". Every refractory neuron will need an input to become excitable, and then takes one more input to fire. We also assume that neurons have variable firing rates.

We will assume that there is a finite number M of subpopulations of neurons, and that different subpopulations have different firing rates; we will denote the fraction of neurons in subpopulation m by α_m, and the firing rate of these neurons will be denoted ρ_m. For shorthand, we will say that the refractory neurons are at level 0, and the excitable at level 1. We use the index $k = 0, 1$ to denote the state of a given neuron, and $m = 1, \ldots, M$ to index certain subpopulations. Thus we will denote the proportion of neurons of type m that are refractory by $x_{0,m}$, and the proportion that are excitable by $x_{1,m}$.

The interneuronal coupling will be determined by the parameter β. The interpretation of β is that whenever there is a proportion of neurons that are firing, they will promote a fraction of neurons in the network through synaptic connections, and β represents the ratio of neurons being promoted to those currently firing. We also assume that whenever neurons fire, we compute the entire cascade of firing until there are no longer any firing neurons. Moreover, we assume that all neurons that fire are set to the refractory state at the end of the cascade. Thus, the entire state of the network will be determined by the vector $x_{k,m}$ with $k = 0, 1$ and $m = 0, \ldots, M$, as all of the firing neurons will be processed as soon as they fire.

B.2.2 Mathematical definition of model

Choose a natural number M. Let $\boldsymbol{\alpha} = (\alpha_1, \ldots, \alpha_M)$ be any vector with $0 < \alpha_m < 1$, and $\sum_m \alpha_m = 1$, and let $\boldsymbol{\rho} \in (\mathbb{R}^+)^M$. The domain of our dynamical system will be

$$D^{\boldsymbol{\alpha}} := \left\{ x = \{x_{k,m}\} \in \mathbb{R}^{2M} \,|\, x_{0,m} + x_{1,m} = \alpha_m \right\}.$$

We write $y_k = y_k(x) := \sum_m x_{k,m}$, and write $D^{\boldsymbol{\alpha}}$ as the disjoint union $D^{\boldsymbol{\alpha}} = D_{\mathcal{L}}^{\boldsymbol{\alpha},\beta} \dot{\cup} D_G^{\boldsymbol{\alpha},\beta}$, where

$$D_G^{\boldsymbol{\alpha},\beta} := \{ x \in D^{\boldsymbol{\alpha}} \,|\, \beta y_1 \geq 1 \}, \quad D_{\mathcal{L}}^{\boldsymbol{\alpha},\beta} = D^{\boldsymbol{\alpha}} \setminus D_G^{\boldsymbol{\alpha},\beta}.$$

We will also write

$$\partial D_G^{\boldsymbol{\alpha},\beta} = \{ x \colon y_1 = \beta^{-1} \}.$$

We now define a deterministic hybrid dynamical system $\xi^{\boldsymbol{\alpha},\boldsymbol{\rho},\beta}(t)$ with state space $D^{\boldsymbol{\alpha}}$. The system will be hybrid since it will have two different rules on complementary parts of the phase space.

Definition 1 (Definition of $\mathcal{L}$). *Consider the flow defined by*

$$\frac{d}{dt}\xi_{k,m}(t) = \rho_m \mu(\xi)(\xi_{k-1,m}(t) - \xi_{k,m}(t)), \tag{B.1}$$

where $\mu(\xi)$ *is the* scalar *function*

$$\mu(\xi) = \frac{1}{1-\beta y_1} = \frac{1}{1-\beta\sum_m x_{1,m}},$$

and we interpret indices modulo 2. More compactly, define the matrix $\mathcal{L}$ *by*

$$\mathcal{L}_{(k,m),(k',m')} = \delta_{m,m'}(-1)^{1+k+k'}\rho_m, \tag{B.2}$$

and (B.1) *can we written* $\dot{\xi} = \mu(\xi)\mathcal{L}\xi$.

Definition 2 (Definition of G). *Let us now index* $\mathbb{R}^{2M+1}$ *by* (k,m) *with* $k = 0, 1$, $m = 1, \ldots, M$, *plus a state that we denote as* Q. *Define the matrix* $\mathcal{M}$ *whose components are given by*

$$\mathcal{M}_{z,z'} = \begin{cases} -1, & z = (0,m), z' = (0,m), \\ 1, & z = (0,m), z' = (1,m), \\ 1, & z = (1,m), z' = Q \\ 0, & else. \end{cases}$$

Define P_z *as projection onto the* z*th coordinate, and*

$$s_\star^\beta(\xi) = \inf_{s>0}\left\{s \middle| P_Q\left(e^{s\beta\mathcal{M}}\xi\right) = s\right\},$$

and then define $G^{\boldsymbol{\alpha},\beta}(\xi)$ *componentwise by*

$$\begin{aligned} P_{(1,m)}(G^{\boldsymbol{\alpha},\beta}(\xi)) &= P_{(1,m)}(e^{\beta s_\star^\beta(\xi)\mathcal{M}}\xi), \\ P_{(0,m)}(G^{\boldsymbol{\alpha},\beta}(\xi)) &= \alpha_m - P_{(1,m)}(G^{\boldsymbol{\alpha},\beta}(\xi)). \end{aligned} \tag{B.3}$$

Definition 3 (Definition of full system). *We combine the above to define a hybrid system for all* $t > 0$. *In short, the system uses flow given by* $\mathcal{L}$ *on the domain* $D_{\mathcal{L}}^{\boldsymbol{\alpha},\beta}$, *and if the system ever enters the domain* $D_G^{\boldsymbol{\alpha},\beta}$, *it immediately applies the map* G.

More specifically: fix $\boldsymbol{\rho}, \beta$. *Define the flow map* $\varphi(x,t)$ *by*

$$\frac{d}{dt}\varphi(\xi,t) = \mu(\xi)\mathcal{L}\xi, \quad \varphi(\xi,0) = \xi.$$

Assume $\xi(0) \in D_{\mathcal{L}}^{\alpha,\beta}$, *and let*

$$\tau_1 = \inf_{t>0}\{\varphi(\xi(0),t) \in D_G^{\alpha,\beta}\}. \tag{B.4}$$

We then define

$$\xi(t) = \varphi(\xi(0),t) \text{ for } t \in [0,\tau_1), \quad \xi(\tau_1) = G(\varphi(\xi(0),\tau_1)).$$

(Of course, it is possible that $\tau_1 = \infty$, *in which case we have defined the system for all positive time, otherwise we proceed recursively.) Now, given* $\tau_n < \infty$ *and* $\xi(\tau_n) \in D_{\mathcal{L}}^{\alpha,\beta}$, *define*

$$\tau_{n+1} = \inf_{t>\tau_n}\{\varphi(\xi(\tau_n), t-\tau_n) \in D_G^{\alpha,\beta}\}, \tag{B.5}$$

and

$$\xi(t) = \varphi(\xi(\tau_n), t-\tau_n) \text{ for } t \in [\tau_n, \tau_{n+1}), \quad \xi(\tau_{n+1}) = G(\varphi(\xi(\tau_n), \tau_{n+1}-\tau_n)).$$

If $\tau_n = \infty$ *then we define* $\tau_{n+1} = \infty$ *as well. We call the times* $\tau_1, \tau_2, \ldots$ *the* **big burst times**, *and we call* $s_\star^\beta(\xi(\tau_n))$ *the* **size of the big burst**.

Remark 4. *We note that the definition given above is well-defined and gives a unique trajectory for* $t \in [0,\infty)$ *if and only if we know that* $G(\xi) \in D_{\mathcal{L}}$ *for any* $\xi \in D_G$. *We will show below that this is the case. We will also see below that some trajectories have infinitely many big bursts, and some have finitely many—this depends both on parameters and initial conditions.*

B.2.3 Intuition behind definition

This is no doubt a complicated description, but all of the pieces of this definition can be well-motivated. We give an intuitive description of this justification now, and make a connection to a stochastic model in Section B.2.4 below.

First consider an infinite network where each parent neuron firing gives rise to

an independent random number of children neurons firing, and the expected number of children per parent is β. Then assume that when a neuron fires, we recursively compute all descendants of this initial neuron until the activity dies away. The expected number firing in the first generation is β, and the expected number firing in the second generation is β^2, etc. It is clear that the expected number of neurons that fire in the entire cascade is $\sum_{\ell=0}^{\infty} \beta^\ell = (1-\beta)^{-1}$, if this sum converges, i.e. if $\beta < 1$. Let us call this $\beta < 1$ case **subcritical**. If $\beta > 1$, then the expected size of the cascade is infinite, and let us call this case **supercritical**.

Now consider the network defined above. Notice that a neuron is only primed to fire if it is excitatory, and the total proportion of excitatory neurons is y_1. Thus, when a neuron fires, the proportion of neurons that are "available" is given by y_1, and the average number of children per parent is βy_1, and so we should consider the case $\beta y_1 < 1$ as subcritical, and the cascade size is $(1-\beta y_1)^{-1}$. This means that the "force multiplier" of each neuron is $\mu(\xi)$ as defined above, by which we mean if an infinitesimal fraction of neurons enter the firing state, then the total size of the burst that arises should be $\mu(\xi)$ times this fraction. With β positive but subcritical, this just "speeds up" the ODE by the multiplicative factor $\mu(\xi)$.

If the state ξ is supercritical ($\beta y_1 > 1$), then the above argument implies an infinite cascade. However, notice that y_1 will evolve during the cascading process as neurons are drawn from the excitatory state into the firing state. To model this, we should consider a system where neurons in the queue are being processed and thrown away at rate 1, and this induces neurons to move from refractory to excitatory at rate β times the proportion that are refractory, and from excitatory to firing at rate β times the proportion that are excitatory. But notice the definition of $\mathcal{M}$: this is exactly what happens as the system evolves, and we stop the system when the proportion of neurons in the queue is equal to the time that we have evolved — which is of course equivalent to saying that if we are removing neurons from the queue at constant rate 1, then it is the first time the queue is empty. Then, all of the neurons that have fired are then reset to be refractory, which is the same as saying that they are reinjected at level zero.

B.2.4 Connection to stochastic model

We now present a stochastic neuronal network model that generalizes the one considered in [62, 63]. The model has N neurons, each of which has an intrinsic firing rate ρ_n. Each neuron can be in one of three states: "quiescent", "excitable", and "firing", which we denote as levels 0,1,2.

If there are no neurons firing, we promote the nth neuron in the network with rate ρ_n, i.e. we choose N independent random times T_n, where T_n is exponentially distributed with rate ρ_n, and define

$$T = \min_n T_n, \quad n^\star = \arg\min_n T_n,$$

and then we promote neuron $n^\star$ by one level and increment the time variable by T.

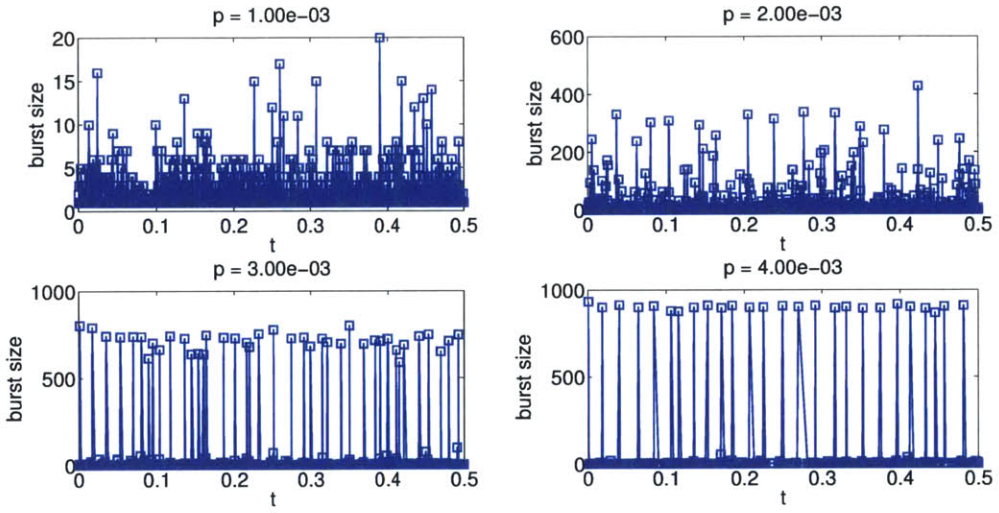

Figure B-1: Different behaviors of the model. We fix $M = 10$, $N = 1000$, and plot different dynamics of the model that correspond to different p. As we increase p, we see the change from asynchronous and irregular behavior to synchronous and periodic behavior.

If there are neurons firing, we compute the effect of a cascade as follows: for each neuron in the firing queue, we promote each other neuron in the network, independently, with probability p. If any neurons are raised to the level of firing, we add them to the queue, and we continue this process until the firing queue is empty. Note that the probability of any neuron promoting any other neuron is the same, so it will

not matter how we process the neurons in the queue (FIFO, LIFO, etc.). However, if a neuron fires in a given burst, we temporarily remove it from the population until the burst is completed, then reinsert all of the neurons that have fired back to the quiescent state. This is a type of refractoriness, in that no neuron can fire more than once in a burst.

Clearly, all of the interneuronal coupling in this model is through the parameter p. The larger the value of p, the more tightly coupled the system is. What has been observed for models of this type [62, 63, 77] is that when p is small, the typical event size in the system is small, and the system is incoherent; conversely, when p is large, the system is synchronous and periodic (see Figure B-1 for an example, but see other references for more detail).

We can now consider a limit as $N \to \infty$ for this system. Choose M a natural number, and $\boldsymbol{\alpha}, \boldsymbol{\rho}$ as defined in the system above, i.e. $\rho_m > 0$ for all m, $0 < \alpha_m < 1$ for all m and $\sum_m \alpha_m = 1$. For each N, define a partition of N into M disjoint sets, denoted by $A_m^{(N)}$, and require that the firing rate of every neuron in $A_m^{(N)}$ be ρ_m. As $N \to \infty$, assume that $||A_m^{(N)}| - \alpha_m N| < 1$ for all m. (Note that $\alpha_m N$ is not in general an integer, but we require that $|A_m^{(N)}|$ be as close to this number as possible.)

It is not hard to see that the description defines a stochastic process with parameters $N, \boldsymbol{\alpha}, \boldsymbol{\rho}, p$, which we will denote as $X_t^{N,\boldsymbol{\alpha},\boldsymbol{\rho},p}$ below. In the limit $N \to \infty$, we will state the convergence theorem of the stochastic neuronal network to a mean-field limit — the proof given there will work with some technical changes.

Theorem 5. *Consider any $x \in D^{\boldsymbol{\alpha}} \cap \mathbb{Q}^{2M}$. For N sufficiently large, Nx has integral components and we can define the neuronal network process $X_t^{N,\boldsymbol{\alpha},\boldsymbol{\rho},p}$ as above, with initial condition $X_0^{N,\boldsymbol{\alpha},\boldsymbol{\rho},p} = Nx$.*

Choose and fix $\epsilon, h, T > 0$. Let $\xi^{\boldsymbol{\alpha},\boldsymbol{\rho},\beta}(t)$ be the solution to the mean-field defined in Definition 3 with initial condition $\xi^{\boldsymbol{\alpha},\boldsymbol{\rho},\beta}(0) = x$. Define the times $\tau_1, \tau_2, \ldots$ at which the mean field jumps, and define $b_{min}(T) = \min\{s_\star^\beta(\xi(\tau_k)) : \tau_k < T\}$, i.e. b_{min} is the size of the smallest big burst which occurs before time T, and let $m(T) = \arg\max_k \tau_k < T$, i.e. $m(T)$ is the number of big bursts in $[0, T]$.

Pick any $\gamma < b_{min}(T)$. For the stochastic process $X_t^{N,\boldsymbol{\alpha},\boldsymbol{\rho},p}$, denote by $T_k^{(N)}$ the

(random) times at which the $X_t^{N,\boldsymbol{\alpha},\boldsymbol{\rho},p}$ *has a burst of size larger than* γN*. Then there exists* $C_{0,1}(\epsilon) \in [0,\infty)$ *and* $\omega(M) \geq 1/(5M)$ *such that for* N *sufficiently large,*

$$\mathbb{P}\left(\sup_{j=1}^{m(T)} \left|T_j^{(N)} - \tau_j\right| > \epsilon\right) \leq C_0(\epsilon) N e^{-C_1(\epsilon) N^{\omega(M)}}. \tag{B.6}$$

Moreover, if we define $\mathcal{T} := ([0,T] \setminus \cup_{j=1}^{m(T)}(T_j^{(N)} - \epsilon, T_j^{(N)} + \epsilon))$*, and*

$$\varphi(t) = t - (T_j^{(N)} - \tau_j) \text{ where } j = \max\{k\colon \tau_k < t\},$$

then

$$\mathbb{P}\left(\sup_{t\in\mathcal{T}} \left|N^{-1} X_t^{K,\boldsymbol{\alpha},\boldsymbol{\rho},p} - \xi^{\boldsymbol{\alpha},\boldsymbol{\rho},\beta}(\varphi(t))\right| > \epsilon\right) \leq C_0(\epsilon) N e^{-C_1(\epsilon) N^{\omega(M)}}. \tag{B.7}$$

In summary, the theorem has two main conclusions about what happens if we consider a stochastic neuronal network with N large. The first is that (up to some technical details) the stochastic system is a fluctuation around the mean-field system when N is sufficiently large. Recalling Figure B-1 again: we will show below that the mean-field system has an attracting fixed point for β sufficiently small, and the incoherent dynamics for small p correspond to fluctuations around this fixed point. Conversely, we show that for β sufficiently large, the mean-field system has a limit cycle, and the periodic dynamics for large p correspond to fluctuations around this limit cycle.

In Figure B-2, we show numerically the convergence result in another way: in dark blue, we plot the mean and standard deviation of the sizes of burst in the stochastic model, and in red we corresponding quantity in the mean-field model, the function $s_\star(\beta)$ defined in Lemma 4 below. We see that they match well even for $N = 1000$.

The guaranteed rate of convergence is subexponential due to the presence of the $\omega(M)$ power in the exponent, but note that the convergence is asymptotically faster than any polynomial. Numerical simulations done for the case of $M = 1$ were reported in [62] show that $\omega(1)$ seemed to be close to 1, and this closeness was uniform in K. This suggests that the lower bound is pessimistic and that the convergence may in

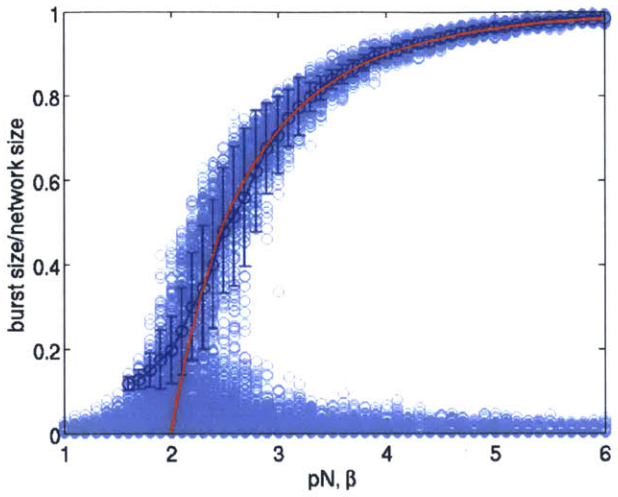

Figure B-2: The meaning of the blue data: we fix a choice of $\boldsymbol{\alpha}$, and $N = 1000$, then run the stochastic neuronal network described in this section. We plot the burst sizes in light blue. For p large enough, we also plot the mean and standard deviations of the burst sizes for all of the bursts larger than one-tenth the size of the network. In red, we plot the deterministic burst size (as a proportion of network size) in the deterministic limit defined in Section B.3.2 below (in fact, we are plotting the function $s_\star(\beta)$ defined in Lemma 4. The result of Theorem 5 is that the dark blue circles lie on the red curve, and that the error bars get small, as $N \to \infty$. The numerics seem to verify this.

fact be exponential. However, the lower bound given in the theorem above seems to be the best that can be achieved by the authors' method of proof. For the details comprising a complete proof of Theorem 5, see [63].

B.3 Main theorem and analysis

The main result of this paper is to prove that for any M, $\boldsymbol{\alpha}$, and $\boldsymbol{\rho}$, then for β sufficiently small, the system has a globally attractive fixed point, and for β sufficiently large, the system has a globally attracting periodic orbit.

It should be noted that the there is no clear *a priori* method of analyzing the stability of the model considered here. As is well known, the analysis of hybrid systems can be exceedingly complicated [27, 128]; questions just about the stability of fixed points is much more complicated than in the non-hybrid (flow or map) case, and stability of periodic orbits are more complicated still. As we see below, the state

of the art technique for this kind of problem is very problem-specific; in general, one contrives to construct some sort of Lyapunov function for the system, and this is what we are able to do here.

B.3.1 Main result

We now state the main result of the paper.

Theorem 6. *Choose and fix $M, \boldsymbol{\alpha}, \boldsymbol{\rho}$, and consider the hybrid system $\xi^{\boldsymbol{\alpha},\boldsymbol{\rho},\beta}(t)$ defined in Definition 3. Then:*

- *For $\beta < 2$ and all M, the system has a globally attracting fixed point $\xi_{\mathsf{FP}}^{\boldsymbol{\alpha},\boldsymbol{\rho},\beta}$.*
- *For any $M \geq 1$, there exists $\beta_M \geq 2$ such that, for $\beta > \beta_M$, the hybrid system has a globally attracting limit cycle $\xi_{\mathsf{LC}}^{\boldsymbol{\alpha},\boldsymbol{\rho},\beta}(t)$. This orbit $\xi_{\mathsf{LC}}^{\boldsymbol{\alpha},\boldsymbol{\rho},\beta}(t)$ undergoes infinitely many big bursts. Moreover, $\limsup_{M\to\infty} \beta_M / \log(\sqrt{M}) \leq 1$.*

We delay the formal proof of the main theorem until after we have stated and proved all of the auxiliary results below, but we give a sketch here.

The main analytic technique we use is a contraction mapping theorem, and we prove this in two parts. We first show that for any two initial conditions, the flow part of the system stretches the distance between them by no more than $1 + \sqrt{M}/2$ (Theorem 7). We then show that the map G_β is a contraction, and, moreover, its modulus of contraction can be made as small as desired by choosing β large enough (Theorem 9). The stretching modulus of one "flow, map" step of the hybrid system is the product of these two numbers, and as long as this is less than one we have a contraction. Finally, we also show that for $\beta > 2$, there exists an orbit with infinitely many big bursts (Lemma 6)—in fact, we show the stronger result that all initial conditions give an orbit with infinitely many big bursts. All of this together, plus compactness of the phase space, implies that this orbit is globally attracting.

We point out that several parts of the argument that seem straightforward at first glance are actually nontrivial for a few reasons.

First, consider the task of computing the growth rate for the flow part of the hybrid system. Clearly $e^{t\mathcal{L}}$ is a contraction, since its eigenvalues are

$$\{0^M, -2\rho_1, -2\rho_2, \ldots, -2\rho_M\},$$

and the vector in the null space is unique once $\boldsymbol{\alpha}$ is chosen. (We use the notation 0^M to denote M repeated eigenvalues at 0.) However, even though the linear flow $e^{t\mathcal{L}}$ is contracting, and clearly $\left|e^{t\mathcal{L}}x - e^{t\mathcal{L}}x'\right| < |x - x'|$ for any fixed $t > 0$, the difficulty is that two different initial conditions can flow for a different interval of time until the first big burst, and clearly we cannot guarantee that $e^{t\mathcal{L}}x$ and $e^{t'\mathcal{L}}x'$ are close at all. For example, consider the extreme case where the flow $e^{t\mathcal{L}}x$ hits the set $D_G^{\boldsymbol{\alpha},\beta}$ at some finite time, and the flow $e^{t\mathcal{L}}x'$ never does—then these trajectories can end up arbitrarily far apart, regardless of the spectrum of $\mathcal{L}$. For both of these reasons, we cannot simply use the spectral analysis of $\mathcal{L}$ for anything useful and have to work harder at establishing a uniform contraction bound.

Moreover, we point out another subtlety of hybrid systems, which is that the composition of two stable systems is not stable in general. In fact, establishing stability properties for hybrid systems, even when all components are stable and linear, is generally a very nontrivial problem (see, for example [122]). We get around this by showing the subsystems are each contractions (i.e. we show that $\|\cdot\|_2$ is a strict Lyapunov function for the system), but needing to control every potential direction of stretching adds complexity to the analysis.

B.3.2 Intermediate results

This section lists several intermediate results that we now quickly summarize. In Lemma 2 we show that we can in practice ignore the scalar function $\mu(\xi)$. In Lemma 3, we show that the size of the big burst can be written as the root of a certain analytic function. In Lemma 4, we show that for fixed parameters, the size of the big burst is independent of where we enter $D_G^{\boldsymbol{\alpha},\beta}$ and derive some of the properties of the size of the big burst when parameterized by β.

Lemma 2. *Recall the equation* (B.1), *written as*

$$\frac{d\xi}{dt} = \mu(\xi)\mathcal{L}\xi.$$

If we replace the scalar function $\mu(\xi)$ *with any constant, this does not affect the trajectories of the hybrid system whatsoever (although it does affect the speed with which they are traced).*

Proof. Since $\mu(\xi(t))$ is a scalar function of time, we can remove it by the time change $\tau = \mu(\xi)t$, and then we have

$$\frac{d}{d\tau} = \mathcal{L}\xi.$$

Clearly this does not affect the trajectories of the hybrid system and thus will not affect any of the conclusions of Theorem 6. Thus w.l.o.g. we will drop μ below. □

Since the flow has the form

$$\frac{d}{dt}\begin{pmatrix} x_{0,m} \\ x_{1,m} \end{pmatrix} = \rho_m \begin{pmatrix} -1 & 1 \\ 1 & -1 \end{pmatrix} \begin{pmatrix} x_{0,m} \\ x_{1,m} \end{pmatrix}, \tag{B.8}$$

the solution is

$$x_{1,m}(t) = \frac{\alpha_m}{2} + \frac{x_{1,m}(0) - x_{0,m}(0)}{2} e^{-2\rho_m t} = \frac{\alpha_m}{2} - \left(\frac{\alpha_m}{2} - x_{1,m}(0)\right) e^{-2\rho_m t}, \tag{B.9}$$

and of course $x_{0,m}(t) = \alpha_m - x_{1,m}(t)$.

Lemma 3. *If we define*

$$\begin{aligned} \psi^\beta(x,s) &= -s + \sum_{m=1}^{M} x_{1,m}\left(1 - e^{-s\beta}\right) + \sum_{m=1}^{M} x_{0,m}\left(1 - e^{-s\beta} - s\beta e^{-s\beta}\right) \\ &= -s + y_1\left(1 - e^{-s\beta}\right) + y_0\left(1 - e^{-s\beta} - s\beta e^{-s\beta}\right), \end{aligned} \tag{B.10}$$

then

$$s_\star^\beta(x) = \inf_{s>0} \psi^\beta(x,s).$$

Proof. If $\dot{z} = \beta \mathcal{M} z$, then writing this in coordinates gives

$$\dot{z}_Q = \beta \sum_{m=1}^{M} z_{1,m}, \quad \dot{z}_{1,m} = \beta(z_{0,m} - z_{1,m}), \quad \dot{z}_{0,m} = -\beta z_{0,m}.$$

One can compute directly that

$$z_Q(s) = \sum_{m=1}^{M} z_{1,m}(0)\left(1 - e^{-s\beta}\right) + \sum_{m=1}^{M} z_{0,m}(0)\left(1 - e^{-s\beta} - s\beta e^{-s\beta}\right)$$

and thus $z_Q(s) = s$ iff $\psi^\beta(z, s) = 0$. The remainder follows from the definition of $s_\star^\beta$. □

Lemma 4. *$s_\star^\beta(x)$ is constant on $\partial D_G^{\boldsymbol{\alpha},\beta}$, and its value depends only on β. We write $s_\star(\beta)$ for its value on this set. $s_\star(\beta)$ is an increasing function of β, and*

$$\lim_{\beta \to \infty} s_\star(\beta) = 1.$$

Proof. We see from (B.10) that $\psi^\beta(x, s)$, and thus $s_\star^\beta(x)$, depend on x only through the sums y_0 and y_1. By definition y_0 and y_1 are constant on $\partial D_G^{\boldsymbol{\alpha},\beta}$, and therefore $s_\star^\beta(\cdot)$ is as well. On $\partial D_G^{\boldsymbol{\alpha},\beta}$, $y_0 = (\beta - 1)/\beta$ and $y_1 = 1/\beta$, so on this set we can ignore x and simplify ψ to

$$\psi^\beta(s) = 1 - s - e^{-s\beta} - \frac{\beta - 1}{\beta} s\beta e^{-s\beta} = 1 - s - ((\beta - 1)s + 1)e^{-s\beta}. \tag{B.11}$$

It follows from this formula that

$$\psi^\beta(0) = 0, \quad \psi^\beta(1) = -\beta e^{-\beta} < 0, \quad \frac{d\psi^\beta}{ds}(0) = 0, \quad \frac{d^2\psi^\beta}{ds^2}(0) = \beta(\beta - 2).$$

If $\beta < 2$, then $\psi^\beta(s)$ is negative for some interval of s around zero, and thus $s_\star(\beta) = 0$. If $\beta > 2$, then the graph $\psi^\beta(s)$ is tangent to the x-axis at $(0, 0)$ but is concave up, and thus positive for some interval of s around zero, and therefore $s_\star(\beta) > 0$. Since $\psi^\beta(1) < 0$, it is clear that $s_\star(\beta) < 1$. Taking β large, we see that $\psi^\beta(s) \approx 1 - s$, so that $s_\star(\beta) \approx 1$ for β large.

Finally, thinking of $\psi^\beta(s)$ as a function of both s and β, we have

$$\frac{\partial}{\partial s}\psi^\beta(s) = e^{-s\beta}\left(1 - e^{s\beta} + \beta(\beta-1)s\right), \quad \frac{\partial}{\partial \beta}\psi^\beta(s) = e^{-\beta s}(\beta-1)s^2.$$

Since the second derivative of $e^{s\beta}\partial\psi^\beta/\partial s$ is always negative, this means that $\partial\psi^\beta/\partial s$ can have at most two roots, and one of them is at $s = 0$. From the fact that $\psi^\beta(s)$ is concave up at zero, this means that the single positive root of $\partial\psi^\beta/\partial s$ is strictly less than $s_\star(\beta)$. From this it follows that $\partial\psi^\beta/\partial s|_{s=s_\star(\beta)} > 0$. It is clear from inspection that $\partial\psi^\beta/\partial\beta|_{s=s_\star(\beta)} < 0$, and from this and the implicit function theorem, we have $\partial s_\star/\partial\beta > 0$. □

Remark 5. *By definition, a big burst occurs on the set $D_G^{\boldsymbol{\alpha},\beta}$, where $y_1 \geq \beta^{-1}$. Since the flow has continuous trajectories, it must enter $D_G^{\boldsymbol{\alpha},\beta}$ on the boundary $\partial D_G^{\boldsymbol{\alpha},\beta}$, and note that on this set, formula* (B.11) *is valid.*

We can further simplify the formula for $G^{\boldsymbol{\alpha},\beta}$ as follows:

$$\begin{aligned} G_{0,m}^{\boldsymbol{\alpha},\beta}(x) &= \alpha_m - e^{-\beta s_\star^\beta(x)}(\beta s_\star^\beta(x)x_{0,m} + x_{1,m}), \\ G_{1,m}^{\boldsymbol{\alpha},\beta}(x) &= e^{-\beta s_\star^\beta(x)}(\beta s_\star^\beta(x)x_{0,m} + x_{1,m}). \end{aligned} \tag{B.12}$$

Note that different subpopulations are coupled only through $s_\star^\beta(x)$.

B.3.3 Infinitely many big bursts

In this section, we show that for $\beta > 2$, all orbits of $\xi^{\boldsymbol{\alpha},\boldsymbol{\rho},\beta}(t)$ have infinitely many big bursts.

Lemma 5.

$$G^{\boldsymbol{\alpha},\beta}\colon D_G^{\boldsymbol{\alpha},\beta} \to D_{\mathcal{L}}^{\boldsymbol{\alpha},\beta}.$$

Proof. Let $x \in D_G^{\boldsymbol{\alpha},\beta}$, and consider the flow $\dot{z} = \beta\mathcal{M}z$, with $z(0) = x$. Since $d\mathbf{z}_Q(s)/ds > 0$ and $z_Q(0) = 0$, we have that $z_Q(s) > 0$ for $s \in [0, s_\star^\beta(x))$. This means that

$$\frac{d}{ds}(z_Q(s) - s) < 0,$$

or

$$1 > \frac{d}{ds} z_Q(s) = \beta \sum_{m=1}^{M} z_{1,m}(s).$$

From this, it follows that

$$\sum_{m=1}^{M} G_{1,m}^{\boldsymbol{\alpha},\beta}(x) < \frac{1}{\beta},$$

and $G^{\boldsymbol{\alpha},\beta}(x) \in D_{\mathcal{L}}^{\boldsymbol{\alpha},\beta}$. □

It is apparent that the flow (B.8) has a family of attracting fixed points given by $x_{0,m} = x_{1,m}$, and, moreover that $x_{0,m} + x_{1,m}$ is a conserved quantity under this flow. Therefore, if we assume that $x_{0,m}(t) + x_{1,m}(t) = \alpha_m$ for some t, then this is true for all t. Under this restriction, there is a unique attracting fixed point $\xi_{\mathsf{FP}}^{\boldsymbol{\alpha},\boldsymbol{\rho},\beta}$ given by

$$\left(\xi_{\mathsf{FP}}^{\boldsymbol{\alpha},\boldsymbol{\rho},\beta}\right)_{0,m} = \left(\xi_{\mathsf{FP}}^{\boldsymbol{\alpha},\boldsymbol{\rho},\beta}\right)_{1,m} = \frac{\alpha_m}{2}.$$

Lemma 6. *If $\beta > 2$, then $\xi_{\mathsf{FP}}^{\boldsymbol{\alpha},\boldsymbol{\rho},\beta} \in D_G^{\boldsymbol{\alpha},\beta}$ and every initial condition gives rise to a solution with infinitely many big bursts. Moreover, the time it takes any initial condition to enter $D_G^{\boldsymbol{\alpha},\beta}$ is uniformly bounded above.*

Proof. Notice that

$$\sum_{m=1}^{M} \left(\xi_{\mathsf{FP}}^{\boldsymbol{\alpha},\boldsymbol{\rho},\beta}\right)_{1,m} = \sum_{m=1}^{M} \frac{\alpha_m}{2} = \frac{1}{2}.$$

If $\beta > 2$, this is greater than β^{-1}; every initial condition will enter $D_G^{\boldsymbol{\alpha},\beta}$ under the flow. A stronger result is true: for any fixed $\beta > 2$, and any initial condition $x \in D_{\mathcal{L}}^{\boldsymbol{\alpha},\beta}$, there is a global upper bound on the amount of time the system will flow until it hits $D_G^{\boldsymbol{\alpha},\beta}$. Let $\rho_{\mathsf{min}} = \min_{m=1}^{M} \rho_m$ and note that the initial condition $x_{0,m}(0) \leq \alpha_m$ for all m. Then $x_{0,m}(t) = \alpha_m e^{-\rho_m t}$, and we have

$$\sum_{m=1}^{M} x_{0,m}(t) \leq \sum_{m=1}^{M} \alpha_m e^{-\rho_m t} \leq \sum_{m=1}^{M} \alpha_m e^{-\rho_{\mathsf{min}} t} = e^{-\rho_{\mathsf{min}} t},$$

so that at some time less than $t = \rho_{\mathsf{min}}^{-1} \log(\beta/(\beta-1))$, we have $y_0 = 1 - \beta^{-1}$ and thus $y_1 = \beta^{-1}$. By existence-uniqueness and using the fact that different m modes are

decoupled in the flow, any other initial condition must reach this threshold at least as quickly.

Since the only way for the hybrid system to have finitely many big bursts is that it stay in the flow mode for an infinite time, we are done. □

B.3.4 Growth properties of stopped flow

The main result of this subsection is Theorem 7, from which we obtain an upper bound on the maximal stretching given by the stopped flow.

Definition 4.

$$F^{\boldsymbol{\alpha}} := \left\{ x \in D^{\boldsymbol{\alpha}} \colon x_{1,m} < \frac{\alpha_m}{2} \text{ for all } m \right\}.$$

Lemma 7. *For any $\beta > 2$, there exists $n_\star(\beta)$ such that for any $\boldsymbol{\rho} > 0$, and any solution of the hybrid system $\xi^{\boldsymbol{\alpha},\boldsymbol{\rho},\beta}(t)$ with initial condition $\xi^{\boldsymbol{\alpha},\boldsymbol{\rho},\beta}(0) \in D_{\mathcal{L}}^{\boldsymbol{\alpha},\beta}$, we have $\xi^{\boldsymbol{\alpha},\boldsymbol{\rho},\beta}(t) \in F^{\boldsymbol{\alpha}}$ for all $t > \tau_{n_\star(\beta)}$.*

Remark 6. *In short, this lemma says that any initial condition will remain in $F^{\boldsymbol{\alpha}}$ after a finite number of big bursts, and this number depends only on β.*

Proof. We will break this proof up into two steps: first, we will show that $F^{\boldsymbol{\alpha}}$ is absorbing; second, we will show that every initial condition will enter it after $n_\star(\beta)$ big bursts. Together, this will prove the lemma.

First assume that $\xi^{\boldsymbol{\alpha},\boldsymbol{\rho},\beta}(t) \in F^{\boldsymbol{\alpha}}$, and let τ_n be the time of the next big burst after t. From (B.9), the $(1,m)$ coordinate cannot cross $\alpha_m/2$ under the flow, so $\xi^{\boldsymbol{\alpha},\boldsymbol{\rho},\beta}(\tau_n-) \in F^{\boldsymbol{\alpha}}$. Let us denote $x = \xi^{\boldsymbol{\alpha},\boldsymbol{\rho},\beta}(\tau_n-)$, and, recalling (B.12), we have

$$G_{1,m}^{\boldsymbol{\alpha},\beta}(x) = e^{-\beta s_\star^\beta(x)}(\beta s_\star^\beta(x) x_{0,m} + x_{1,m}). \tag{B.13}$$

This is a linear combination of $x_{0,m} \in [\alpha_m/2, \alpha_m]$ and $x_{1,m} \in [0, \alpha_m/2]$, so we need only check the extremes. If we take $x_{0,m} = \alpha_m$ and $x_{1,m} = 0$, then we have $G_{1,m}^{\boldsymbol{\alpha},\beta}(x) = ze^{-z}\alpha_m$ for some $z > 0$, and $\sup_{z>0} ze^{-z} = 1/e$. Considering the other extreme gives $G_{1,m}^{\boldsymbol{\alpha},\beta}(x) = (z+1)e^{-z}\alpha_m/2$, and $\sup_{z>0}(z+1)e^{-z} = 1$. In either case, we have $G_{1,m}^{\boldsymbol{\alpha},\beta}(x) < \alpha_m/2$ and we see that $F^{\boldsymbol{\alpha}}$ is absorbing.

Now assume that $\xi^{\boldsymbol{\alpha},\boldsymbol{\rho},\beta}(0) \notin F^{\boldsymbol{\alpha}}$. Since $\beta > 2$, it follows from Lemma 6 that $\xi^{\boldsymbol{\alpha},\boldsymbol{\rho},\beta}(t)$ has infinitely many big bursts. Let $x = \xi^{\boldsymbol{\alpha},\boldsymbol{\rho},\beta}(\tau_1-)$, noting by definition that $x \in \partial D_G^{\boldsymbol{\alpha},\beta}$. Using (B.13) and $x_{1,m} > \alpha_m/2$, $x_{0,m} < x_{1,m}$,

$$G_{1,m}^{\boldsymbol{\alpha},\beta}(x) < e^{-\beta s_\star^\beta(x)}(\beta s_\star^\beta(x) + 1)x_{1,m}.$$

By Lemma 4 and again recalling that $(z+1)e^{-z} < 1$ for all $z > 0$, this means that there is an $h(\beta) \in (0,1)$ with

$$\xi_{1,m}^{\boldsymbol{\alpha},\boldsymbol{\rho},\beta}(\tau_1) < h(\beta) \cdot x_{1,m}.$$

If $h(\beta)x_{1,m} < \alpha_m/2$, then we are done. If not, notice that the flow generated by $\mathcal{L}$ will make the $(1,m)$ coordinate decrease, so it is clear that if $\xi_{1,m}^{\boldsymbol{\alpha},\boldsymbol{\rho},\beta}(t) \notin F^{\boldsymbol{\alpha}}$ for all $t \in [0,\tau_n)$, then by induction $\xi_{1,m}^{\boldsymbol{\alpha},\boldsymbol{\rho},\beta}(\tau_n) < (h(\beta))^n \alpha_m$. Choose $n_\star(\beta)$ so that $(h(\beta))^{n_\star(\beta)} < 1/2$, and we have that $\xi_{1,m}^{\boldsymbol{\alpha},\boldsymbol{\rho},\beta}(\tau_{n_\star(\beta)}) < \alpha_m/2$ and thus $\xi^{\boldsymbol{\alpha},\boldsymbol{\rho},\beta}(\tau_{n_\star(\beta)}) \in F^{\boldsymbol{\alpha}}$. □

Theorem 7. *Choose any two initial conditions* $x(0), \widetilde{x}(0) \in F^{\boldsymbol{\alpha}} \cap D_{\mathcal{L}}^{\boldsymbol{\alpha},\beta}$, *and define* $\tau, \widetilde{\tau}$ *as in* (B.4). *Then*

$$\left\| e^{\tau\mathcal{L}}x(0) - e^{\widetilde{\tau}\mathcal{L}}\widetilde{x}(0) \right\| \leq \left(1 + \frac{\sqrt{M}}{2}\right) \left\| x(0) - \widetilde{x}(0) \right\|,$$

i.e. for any two initial conditions, the distance at the time of the first big burst has grown by no more than a factor of $1 + \sqrt{M}/2$.

Proof. Before we start, recall that the map $\epsilon^{\tau\mathcal{L}}x$ is nonlinear in x, because τ itself depends nonlinearly on x. Let $\mathbf{1}_M$ be the all-ones column vector in $\mathbb{R}^M$. Let $x(0) \in D_{\mathcal{L}}^{\boldsymbol{\alpha},\beta}$ and consider a perturbation $\boldsymbol{\epsilon} = \{\epsilon_m\}$ with $\sum_m \epsilon_m = 0$, i.e. $\boldsymbol{\epsilon} \in \mathbf{1}_M^\perp$, and define $\widetilde{x}(0)$ by

$$\widetilde{x}_{m,1}(0) = x_{m,1}(0) + \epsilon_m, \quad \widetilde{x}_{m,0}(0) = x_{m,0}(0) - \epsilon_m.$$

Define $\tau, \widetilde{\tau}$ as the burst times associated with these initial conditions as in (B.4), and

by definition, we have

$$\sum_{m=1}^{M} x(\tau-)_{1,m} = \sum_{m=1}^{M} \widetilde{x}(\widetilde{\tau}-)_{1,m} = \frac{1}{\beta}.$$

Writing $\widetilde{\tau} = \tau + \delta$ and using (B.9), we have

$$\sum_{m=1}^{M} \left(\frac{\alpha_m}{2} - \left(\frac{\alpha_m}{2} - x_{1,m}(0) \right) e^{-2\rho_m \tau} \right) = \sum_{m=1}^{M} \left(\frac{\alpha_m}{2} - \left(\frac{\alpha_m}{2} - \widetilde{x}_{1,m}(0) \right) e^{-2\rho_m (\tau+\delta)} \right).$$

Since $\widetilde{x} - x = O(\epsilon)$ and $e^{-2\rho_m \delta} = (1 + O(\delta))$, we can see from this expression that the leading order terms in both ϵ and δ are of the same order. Thus, Taylor expanding to first order in ϵ and δ and canceling gives a solution for δ:

$$\delta = -\frac{\sum_\ell \epsilon_\ell e^{-2\rho_\ell \tau}}{2 \sum_\ell \rho_\ell \left(\frac{\alpha_\ell}{2} - x_{1,\ell}(0) \right) e^{-2\rho_\ell \tau}} + O(\epsilon^2). \tag{B.14}$$

We then have

$$\begin{aligned} \widetilde{x}_{1,m}(\tau + \delta) - x_{1,m}(\tau) &= \epsilon_m e^{-2\rho_m \tau} - 2\rho_m \left(\frac{\alpha_m}{2} - x_{1,m}(0) \right) \delta e^{-2\rho_m \tau} \\ &= \epsilon_m e^{-2\rho_m \tau} - c_m \sum_\ell \epsilon_\ell e^{-2\rho_\ell \tau} + O(\epsilon^2), \end{aligned}$$

where

$$c_m = \frac{\rho_m \left(\frac{\alpha_m}{2} - x_{1,m}(0) \right) e^{-2\rho_m \tau}}{\sum_\ell \rho_\ell \left(\frac{\alpha_\ell}{2} - x_{1,\ell}(0) \right) e^{-2\rho_\ell \tau}}. \tag{B.15}$$

Since $x(0) \in F^{\boldsymbol{\alpha}}$, $c_m > 0$. It is then clear from the definition that $c_m < 1$. Writing this in matrix form in terms of ϵ gives

$$\begin{pmatrix} \widetilde{x}_{1,m}(\tau + \delta) - x_{1,m}(\tau) \\ \widetilde{x}_{2,m}(\tau + \delta) - x_{2,m}(\tau) \\ \vdots \\ \widetilde{x}_{2,M}(\tau + \delta) - x_{2,M}(\tau) \end{pmatrix} = \mathbf{M}_M \begin{pmatrix} \epsilon_1 \\ \epsilon_2 \\ \vdots \\ \epsilon_N \end{pmatrix} + O(\epsilon^2), \tag{B.16}$$

where the matrix $\mathbf{M}_M$ is defined as,

$$\mathbf{M}_M = \begin{pmatrix} e^{-2\rho_1\tau} - c_1 e^{-2\rho_1\tau} & -c_1 e^{-2\rho_2\tau} & \cdots & -c_1 e^{-2\rho_M\tau} \\ -c_2 e^{-2\rho_1\tau} & e^{-2\rho_2\tau} - c_2 e^{-2\rho_2\tau} & \cdots & -c_2 e^{-2\rho_M\tau} \\ \vdots & \vdots & \ddots & \vdots \\ -c_M e^{-2\rho_1\tau} & -c_N e^{-2\rho_2\tau} & \cdots & e^{-2\rho_M\tau} - c_N e^{-2\rho_M\tau} \end{pmatrix}, \quad \text{(B.17)}$$

or, more compactly,

$$(\mathbf{M}_M)_{ij} = -c_i e^{-2\rho_j\tau} + \delta_{ij} e^{-2\rho_i\tau}.$$

Thus, the map $e^{\tau\mathcal{L}}x$ has Jacobian $\mathbf{M}_M$. Since $\mathbf{M}_M$ has zero column sums, it is apparent that $\mathbf{1}^\intercal \mathbf{M}_M = \mathbf{0}$ and thus $0 \in \mathrm{Spec}(\mathbf{M}_M)$. Since all of the nondiagonal entries of $\mathbf{M}_M$ are bounded above by one, the standard Gershgorin estimate implies that all of the eigenvalues of $\sqrt{\mathbf{M}_M^\intercal \mathbf{M}_M}$ lie in a disk of radius $O(M)$ around the origin, but this is not good enough to establish our result.

We can work out a more delicate bound: by the definition of D^α, we need only consider zero sum perturbations, and so in fact we are concerned with $\mathbf{M}_M$ restricted to $\mathbf{1}_M^\perp$. From this and the fundamental theorem of calculus, it follows that

$$\left\| e^{\tau\mathcal{L}}x(0) - e^{\tilde{\tau}\mathcal{L}}\tilde{x}(0) \right\| \leq \left\| \mathbf{M}_M|_{\mathbf{1}_m^\perp} \right\|_2 \left\| x(0) - \tilde{x}(0) \right\|,$$

where $\|\cdot\|_2$ is the spectral norm of a matrix (q.v. Definition 5 below). Using the bound in Lemma 8 proves the theorem. □

Definition 5. *We define the* **spectral norm** *of a square matrix A by*

$$\|A\|_2 = \sup_{x \neq \mathbf{0}} \frac{\|Ax\|_2}{\|x\|_2},$$

where $\|\cdot\|_2$ is the Euclidean (L^2) norm of a vector.

The spectral norm of a matrix is equal to its largest singular value, and if the matrix is symmetric, this is the same as the largest eigenvalue. In particular, it

follows from the definition that

$$\|Ax\|_2 \leq \|A\|_2 \|x\|_2 .$$

Theorem 8. *Let $\mathbf{1}_M^\perp \subseteq \mathbb{R}^M$ denote the subspace of zero-sum vectors. Then $\mathbf{M}_M : \mathbf{1}_M^\perp \to \mathbf{1}_M^\perp$ since it is a zero column sum matrix, and thus the restriction is well-defined. Then*

$$\left\| \mathbf{M}_M|_{\mathbf{1}_M^\perp} \right\|_2 < 1 + \frac{\sqrt{M}}{2}. \tag{B.18}$$

Proof. Let us denote $\mathbf{I}_M$ to be the M-by-M identity matrix and $\mathbf{1}_M$ the all-one column vector in $\mathbb{R}^M$. We will also define the matrix $\mathbf{D}_M$ and vector $\mathbf{d}_M$ by

$$\mathbf{d}_M = [e^{-2\rho_1 s}, e^{-2\rho_2 s}, \cdots, e^{-2\rho_N s}]^\intercal,$$

and $\mathbf{D}_M$ is the matrix with $\mathbf{d}_M$ on the diagonal, i.e. $(\mathbf{D}_M)_{ij} = \delta_{ij} e^{-2\rho_i \tau}$.

Any vector $\mathbf{v} \in \mathbf{1}_M^\perp$ is in the null space of the matrix $\mathbf{1}\mathbf{1}^\intercal$, and thus $(\mathbf{I}_M - M^{-1}\mathbf{1}\mathbf{1}^\intercal)\mathbf{v} = \mathbf{v}$, and $\mathbf{M}_M = \mathbf{M}_M(\mathbf{I}_M - M^{-1}\mathbf{1}\mathbf{1}^\intercal)$ on $\mathbf{1}^\perp$, so it suffices for our result to bound the norm of $\mathbf{M}_M(\mathbf{I}_M - M^{-1}\mathbf{1}\mathbf{1}^\intercal)$.

We can factorize

$$\mathbf{M}_M = (\mathbf{I} - \mathbf{c}\mathbf{1}^\intercal)\mathbf{D}_M, \tag{B.19}$$

where the components of $\mathbf{c}$ are given in B.15. To see this, we compute

$$\begin{aligned}((\mathbf{I} - \mathbf{c}\mathbf{1}^\intercal)\mathbf{D}_M)_{ij} &= (\mathbf{D}_M)_{ij} - (\mathbf{c}\mathbf{1}^\intercal\mathbf{D}_M)_{ij} = (\mathbf{D}_M)_{ij} - \sum_k c_i \cdot 1 \cdot \delta_{k,j} e^{-2\rho_j \tau} \\ &= \delta_{ij} e^{-2\rho_i \tau} - c_i e^{-2\rho_j \tau}.\end{aligned}$$

Let us first write

$$\begin{aligned}\mathbf{M}_M &= (\mathbf{I} - \mathbf{c}\mathbf{1}^\intercal)\mathbf{D}_M = (\mathbf{D}_M - \mathbf{D}_M\mathbf{c}\mathbf{1}^\intercal + \mathbf{D}_M\mathbf{c}\mathbf{1}^\intercal - \mathbf{c}\mathbf{1}^\intercal\mathbf{D}_M) \\ &= \mathbf{D}_M(\mathbf{I} - \mathbf{c}\mathbf{1}^\intercal) + (\mathbf{D}_M\mathbf{c}\mathbf{1}^\intercal - \mathbf{c}\mathbf{d}_M^\intercal),\end{aligned}$$

where we use the relation $\mathbf{1}^\intercal \mathbf{D}_M = \mathbf{d}_M^\intercal$, and then

$$\mathbf{M}_M(\mathbf{I}-M^{-1}\mathbf{1}\mathbf{1}^\intercal) = \mathbf{D}_M(\mathbf{I}-\mathbf{c}\mathbf{1}^\intercal)(\mathbf{I}-M^{-1}\mathbf{1}\mathbf{1}^\intercal)+(\mathbf{D}_M\mathbf{c}\mathbf{1}^\intercal-\mathbf{c}\mathbf{d}_M^\intercal)(\mathbf{I}-M^{-1}\mathbf{1}\mathbf{1}^\intercal). \quad \text{(B.20)}$$

We break this into two parts. Using the fact that $\mathbf{1}^\intercal\mathbf{1} = M$, we have

$$\mathbf{c}\mathbf{1}^\intercal(\mathbf{I}_M - M^{-1}\mathbf{1}\mathbf{1}^\intercal) = \mathbf{I}_M\mathbf{c}\mathbf{1}^\intercal - M^{-1}\mathbf{c}\mathbf{1}^\intercal\mathbf{1}\mathbf{1}^\intercal = \mathbf{c}\mathbf{1}^\intercal - \mathbf{c}\mathbf{1}^\intercal = 0,$$

and thus the first term can be simplified to

$$\begin{aligned}&\mathbf{D}_M(\mathbf{I} - \mathbf{c}\mathbf{1}^\intercal)(\mathbf{I} - M^{-1}\mathbf{1}\mathbf{1}^\intercal)\\ &= \mathbf{D}_M(\mathbf{I} - M^{-1}\mathbf{1}\mathbf{1}^\intercal) - \mathbf{D}_M(\mathbf{c}\mathbf{1}^\intercal)(\mathbf{I}_M - M^{-1}\mathbf{1}\mathbf{1}^\intercal) = \mathbf{D}_M(\mathbf{I} - M^{-1}\mathbf{1}\mathbf{1}^\intercal).\end{aligned} \quad \text{(B.21)}$$

Since the matrix $M^{-1}\mathbf{1}\mathbf{1}^\intercal$ is an orthogonal projection matrix with norm 1 and rank 1, it follows that $\mathbf{I}_M - M^{-1}\mathbf{1}\mathbf{1}^\intercal$ is also a projection matrix with norm 1 and rank $M-1$. By Cauchy-Schwarz, the norm can be bounded by

$$\left\|\mathbf{D}_M(\mathbf{I} - M^{-1}\mathbf{1}\mathbf{1}^\intercal)\right\|_2 \leq \|\mathbf{D}_M\|_2 \left\|\mathbf{I}_M - M^{-1}\mathbf{1}\mathbf{1}^\intercal\right\|_2 = \|\mathbf{D}_M\|_2 < 1. \quad \text{(B.22)}$$

(The last inequality follows from the fact that $\mathbf{D}_M$ is diagonal and all entries are less than one in magnitude.)

For the second term in Equation (B.20) and noting that $\mathbf{d}^\intercal\mathbf{1} = \sum_m d_m$, we obtain

$$\begin{aligned}&(\mathbf{D}_M\mathbf{c}\mathbf{1}^\intercal - \mathbf{c}\mathbf{d}^\intercal)(\mathbf{I} - M^{-1}\mathbf{1}\mathbf{1}^\intercal)\\ &\quad = \mathbf{D}_M\mathbf{c}\mathbf{1}^\intercal - \mathbf{c}\mathbf{d}^\intercal - \mathbf{D}_M\mathbf{c}\mathbf{1}^\intercal + \frac{\mathbf{d}^\intercal\mathbf{1}}{M}\mathbf{c}\mathbf{1}^\intercal = \mathbf{c}\left(\frac{\sum_m d_m}{M}\mathbf{1} - \mathbf{d}\right)^\intercal.\end{aligned}$$

This outer product is of rank 1, and thus it has exactly one non-zero singular value; this singular value is the product of the L^2 norms of the two vectors, and therefore

$$\left\|(\mathbf{D}_M\mathbf{c}\mathbf{1}^\intercal - \mathbf{c}\mathbf{d}^\intercal)(\mathbf{I}_M - M^{-1}\mathbf{1}\mathbf{1}^\intercal)\right\|_2 = \|\mathbf{c}\|_2 \left\|\mathbf{d} - \frac{\sum_m d_m}{M}\mathbf{1}\right\|_2 < 1 \cdot \frac{\sqrt{M}}{2}.$$

Using Equation (B.20), and the triangle inequality gives the result. □

B.3.5 Contraction of the big burst map

In this section, we demonstrate that $G^{\boldsymbol{\alpha},\beta}$ is a contraction for β large enough, and, moreover, that one can make the contraction modulus as small as desired by choosing β sufficiently large.

Theorem 9. *For any $M \geq 1$ and $\delta > 0$, there is a $\beta_1(M,\delta)$ such that for all $\beta > \beta_1(M,\delta)$ and $x, \widetilde{x} \in \partial D_G^{\boldsymbol{\alpha},\beta}$,*

$$\left\| G^{\boldsymbol{\alpha},\beta}(x) - G^{\boldsymbol{\alpha},\beta}(\widetilde{x}) \right\| \leq \delta \left\| x - \widetilde{x} \right\|.$$

In particular, by choosing β sufficiently large, we can make this map have as small a modulus of contraction as required.

Proof. Let us define the vector $\boldsymbol{\epsilon}$ by

$$\epsilon_m = \widetilde{x}_m - x_m.$$

Since $x, \widetilde{x}$ are both in $\partial D_G^{\boldsymbol{\alpha},\beta}$, $\boldsymbol{\epsilon} \perp \mathbf{1}$. It follows from (B.10) that $\nabla_{\boldsymbol{\epsilon}} \psi^{\beta}(s,x) = 0$. Recall from (B.12) that

$$G_{1,m}^{\boldsymbol{\alpha},\beta}(x) = e^{-\beta s_\star^\beta(x)}(\beta s_\star^\beta(x) x_{0,m} - x_{1,m}),$$

and thus

$$\begin{aligned}
\nabla_\epsilon G_{1,m}^{\boldsymbol{\alpha},\beta}(x) &= e^{-\beta s^*(x)} \left(-\beta \nabla_{\boldsymbol{\epsilon}} s_\star^\beta(x)\right) (\beta s_\star^\beta(x) x_{0,m} - x_{1,m}) \\
&\quad + e^{-\beta s_\star^\beta(x)} (\beta \nabla_{\boldsymbol{\epsilon}} x_{0,m} - \nabla_{\boldsymbol{\epsilon}} x_{1,m}) \\
&= e^{-\beta s_\star^\beta(x)}(\beta s_\star^\beta(x)(-1) - 1),
\end{aligned}$$

so

$$\nabla_{\boldsymbol{\epsilon}} G^{\boldsymbol{\alpha},\beta}(x) = -(e^{-\beta s_\star^\beta(x)}(\beta s_\star^\beta(x) + 1))\mathbf{1}.$$

Note that Lemma 4 implies that $\beta s_\star^\beta(x) \to \infty$ as $\beta \to \infty$ for any x. If we define the function $g(z) = e^{-z}(1+z)$, then it is easy to see that

$$0 < g(z) < 1 \text{ for } z \in (0,\infty), \quad \lim_{z\to\infty} g(z).$$

From this and the fundamental theorem of calculus, the result follows. □

B.3.6 Proof of Main Theorem

Finally, to prove the theorem, we will show that, under sufficient conditions on β, the composition of the map and the flow is eventually a strict contraction for any initial condition.

Definition 6. *We define*

$$\begin{aligned} \mathcal{H}^{\boldsymbol{\alpha},\boldsymbol{\rho},\beta} \colon D_{\mathcal{L}}^{\boldsymbol{\alpha},\beta} &\to D_{\mathcal{L}}^{\boldsymbol{\alpha},\beta} \\ x &\mapsto G^{\boldsymbol{\alpha},\beta}(e^{\tau\mathcal{L}}x), \end{aligned}$$

where τ is the first hitting time defined in (B.4).

Proof of Theorem 6. If we consider any solution of the hybrid system $\xi^{2,\boldsymbol{\alpha},\boldsymbol{\rho}}\beta(t)$ that has infinitely many big bursts, then it is clear from chasing definitions that

$$\xi^{\boldsymbol{\alpha},\boldsymbol{\rho},\beta}(\tau_n) = \left(\mathcal{H}^{\boldsymbol{\alpha},\boldsymbol{\rho},\beta}\right)^n \xi^{\boldsymbol{\alpha},\boldsymbol{\rho},\beta}(0).$$

$\mathcal{H}^{\boldsymbol{\alpha},\boldsymbol{\rho},\beta}$ is the composition of two maps, one coming from a stopped flow and the other coming from the map G. It follows from Theorem 7 that the modulus of contraction of the stopped flow is no more than $1 + \sqrt{M}/2$ on the set $F^{\boldsymbol{\alpha}}$ whenever $\beta > 2$. It follows from Theorem 9 that we can make the modulus of the second flow less than δ by choosing $\beta > \beta_1(M,\delta)$. Let us define

$$\beta_M := \beta_1\left(M, \frac{1}{1+\sqrt{M}/2}\right),$$

and then by composition it follows that $\mathcal{H}^{\boldsymbol{\alpha},\boldsymbol{\rho},\beta}$ is a strict contraction on $F^{\boldsymbol{\alpha}}$. From Lemma 7, it follows that $D_{\mathcal{L}}^{\boldsymbol{\alpha},\beta}$ is mapped into $F^{\boldsymbol{\alpha}}$ in a finite number of iterations, so that $\mathcal{H}^{\boldsymbol{\alpha},\boldsymbol{\rho},\beta}$ is eventually strictly contracting on $D_{\mathcal{L}}^{\boldsymbol{\alpha},\beta}$, and therefore $\mathcal{H}^{\boldsymbol{\alpha},\boldsymbol{\rho},\beta}$ has a globally attracting fixed point, which means that the hybrid system has a globally attracting limit cycle.

Finally, we want to understand the asymptotics as $M \to \infty$. Choose any $0 < \gamma_1, \gamma_2 < 1$. By Lemma 4, $\beta s_\star(\beta) > \gamma_1 \beta$ for β sufficiently large, and it is clear that $e^{-z}(z+1) < e^{-\gamma_2 z}$ for z sufficiently large. From these it follows that for β sufficiently large,

$$e^{-\beta s_\star(\beta)}(\beta s_\star(\beta) + 1) < e^{-\gamma_1 \gamma_2 \beta}.$$

From this we have that $\beta_M < \ln(1 + \sqrt{M}/2)/\gamma_1\gamma_2$ and the result follows.

□

We have shown that β_M is finite and determined its asymptotic scaling as $M \to \infty$. It was shown in [63] that $\beta_1 = 2$, and we can now show that this is the case as well for $M = 2$, i.e.

Proposition 1. *The computations in the proof of Theorem 6 imply that β_2 is, at most, the largest solution of the equation $e^{-\beta s_\star(\beta)}(\beta s_\star(\beta) + 1) < 2/3$. Numerical approximation of this root gives $\beta \approx 2.48$. However, in fact, $\beta_2 = 2$.*

Proof. In $\mathbb{R}^2$, $\mathbf{1}^\perp$ is a one-dimensional space spanned by $(1, -1)^\intercal$, and thus we need only compute the eigenvalue associated with this vector. If we define $\mathbf{v} = \mathbf{M}_2 \cdot (1, -1)^\intercal$ and show $|v_1 - v_2| < 2$, then we have established the result. When $M = 2$, we can write (B.17) as

$$\mathbf{M}_2 = \begin{pmatrix} e^{-2\rho_1\tau} - c_1 e^{-2\rho_1\tau} & -c_1 e^{-2\rho_2\tau} \\ -c_2 e^{-2\rho_1\tau} & e^{-2\rho_2\tau} - c_2 e^{-2\rho_2\tau} \end{pmatrix}, \tag{B.23}$$

and thus

$$\mathbf{v} = \begin{pmatrix} e^{-2\rho_1\tau} - c_1 e^{-2\rho_1\tau} + c_1 e^{-2\rho_2\tau} \\ -c_2 e^{-2\rho_1\tau} - e^{-2\rho_2\tau} + c_2 e^{-2\rho_2\tau} \end{pmatrix}.$$

Thus

$$v_1 - v_2 = e^{-2\rho_1\tau}(1 - c_1 + c_2) + e^{-2\rho_2\tau}(1 + c_1 - c_2).$$

Using $c_1 + c_2 = 1$, this simplifies to

$$v_1 - v_2 = 2c_2e^{-2\rho_1\tau} + 2c_1e^{-2\rho_2\tau}.$$

Since it is clear that $v_1 - v_2 > 0$, we need to show that $v_1 - v_2 < 2$, or

$$2c_1e^{2\rho_1\tau} + 2c_2e^{2\rho_2\tau} < 2e^{(\rho_1+\rho_2)\tau}.$$

Writing $A = \rho_1(\alpha_1/2 - x_{1,1}(0))$, $B = \rho_2(\alpha_2/2 - x_{1,2}(0))$, this becomes

$$\frac{A + B}{Ae^{2\rho_2\tau} + Be^{2\rho_1\tau}} < 1, \tag{B.24}$$

but this must be satisfied, since $e^{2\rho_1\tau}, e^{2\rho_2\tau} > 1$. □

Remark 7. *We conjecture from numerical evidence (cf. Figure B-5) that, in fact, $\beta_M = 2$ for all M.*

B.4 Numerical simulations

In this section, we present some numerical simulations; we verify the existence of the unique attractor whose existence is proven above and give evidence for the conjecture that $\beta_M = 2$ for all M.

We first numerically solve the hybrid ODE-mapping system, with $M = 3$ and random α_i, ρ_i. The ODE portion of the hybrid system can be solved explicitly, and we use MATLAB's `fsolve` to determine the hitting times τ_i. We plot the trace of the system for $\beta = 2.1$, $\beta = 2.5$ for a single initial condition in Figure B-3. We observe that each neuron population is attracted to a periodic orbit after several bursts.

To further demonstrate convergence, we also plot trajectories for the same parameters for various initial conditions in Figure B-4. We see that after three to four

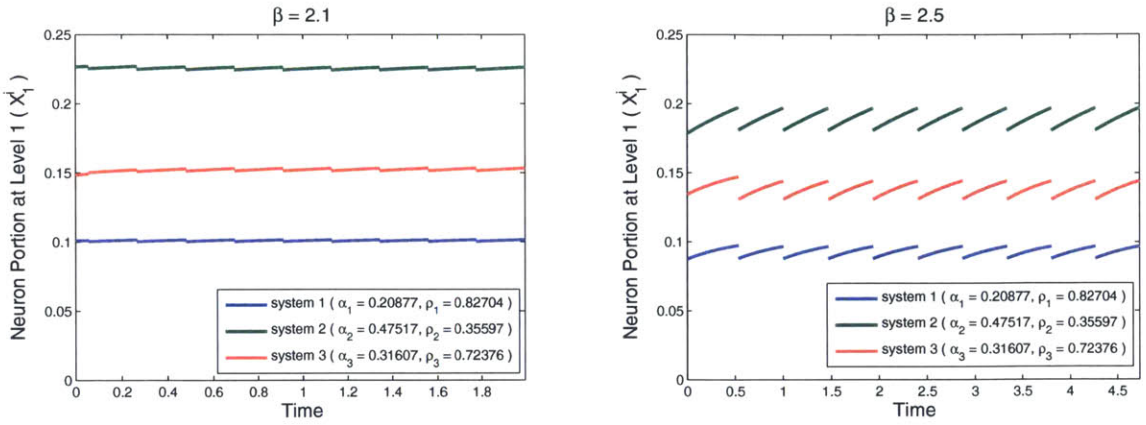

Figure B-3: Plots of the hybrid ODE-mapping system numerical simulation results with $\beta = 2.1$ (left) and $\beta = 2.5$ (right). Both of them are with three neuron populations. The neuron portions at energy level 1 over simulation time are shown in the plots.

bursts, the trajectories converge to the same periodic orbit.

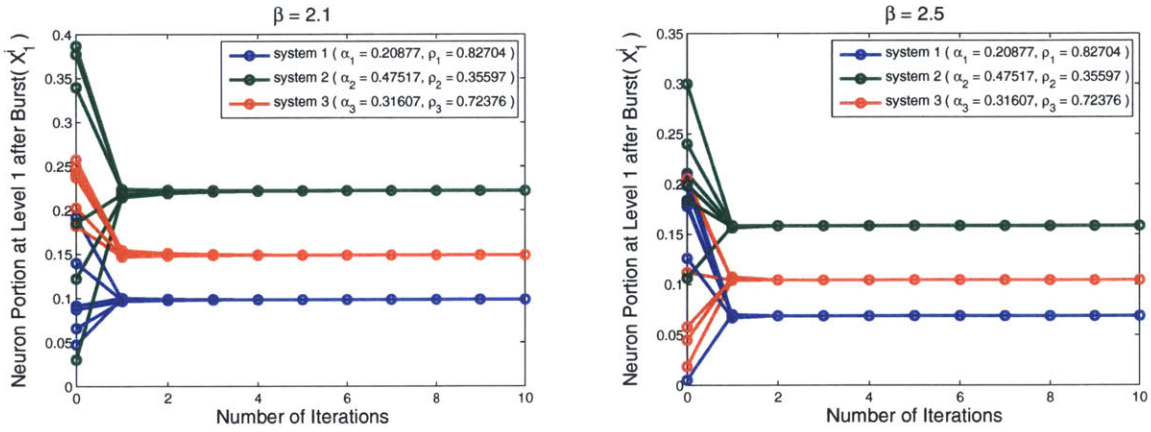

Figure B-4: Plots of neuron proportions after each burst iteration with $\beta = 2.1$ (left) and $\beta = 2.5$ (right). Both subfigures are for $M = 3$. For all initial conditions, the population seems to converge after about four bursts.

We also present some numerics verifying the conjecture in Remark 7, i.e. the numerical evidence in B-5 suggests that $\beta_M = 2$ in general, or, at least, it is much less than the upper bound given in the main theorem. To check this, we choose $10,000$ initial conditions uniformly random in the simplex, and verified that all initial conditions converged to the attracting limit cycle, for all $\beta > 2$. We also see that the

eigenvalues of the map $\mathcal{H}^{\alpha,\rho,\beta}$ have a complicated dependence on β: there seem to be regions where this map has negative eigenvalues and some where it does not, which can be detected by whether we converge monotonically to the limit cycle or not. But it seems to always converge for any $\beta > 2$.

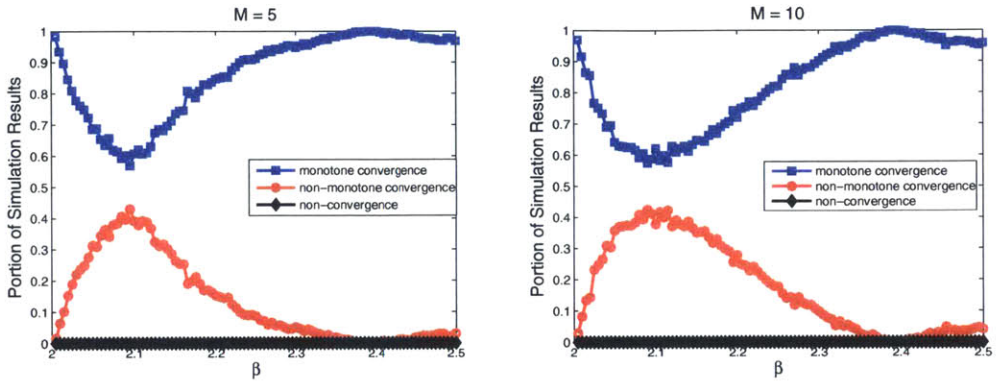

Figure B-5: Proportions of initial conditions that converge monotonically, converge non-monotonically, or do not converge, for $M = 5$ and $M = 10$ subpopulations. The parameters $\boldsymbol{\alpha}$ and $\boldsymbol{\rho}$ are chosen at random and fixed. For each β, we choose $10,000$ initial conditions uniformly in the simplex, and determine which proportion falls into each of three categories: monotone convergent, non-monotone convergent and non-convergent. We vary β from 2.005 to 2.5. We see that all initial conditions converge, but the montonicity of the convergence depends on β.

B.5 Conclusion

We generalized the mean-field model derived in of [62, 63] to the case of multiple subpopulations with different intrinsic firing rates. We analyzed the limiting mean field in the case where each neuron has at most two inactive states, and proved that for sufficiently large coupling parameters, the mean-field limit has a globally attracting limit cycle.

We point out a few similar results in the literature. A similar three-state model was considered in [172, 173, 154] where the number of neurons in the analogous firing state affected the firing rates of all of the neurons in the system. The mean-field model derived there was a delay system instead of a hybrid system, but that model also exhibited the coexistence of a attracting periodic orbit and an attracting limit

cycle, similar to the case considered here. In a different direction, the complete characterization of the dynamics of a network of interacting theta neurons was studied in [131]. Again, this model exhibits the coexistence of macroscopic limit cycles and fixed points, and the bifurcation structure discovered there was more complex, but similar to the only found here (cf. Figure (8b) of [131] and Figure B-2 of the current paper). The model considered here is at first glance quite different from these other two models, in that it explicitly incorporates cascades directly in the dynamics; interestingly, it shows many of the same macroscopic phenomena.

Bibliography

[1] See http://theory.cm.utexas.edu/benchmarks to see the optimization benchmarks.

[2] See https://wiki.fysik.dtu.dk/ase/ for information about the ASE project.

[3] See http://theory.cm.utexas.edu/henkelman/code/ to obtain the TSASE code.

[4] Paul Albertus, Jake Christensen, and John Newman. Experiments on and modeling of positive electrodes with multiple active materials for lithium-ion batteries. *Journal of The Electrochemical Society*, 156(7):A606–A618, 2009.

[5] JL Allen, TR Jow, and J Wolfenstine. Analysis of the $FePO_4$ to $LiFePO_4$ phase transition. *Journal of Solid State Electrochemistry*, 12(7-8):1031–1033, 2008.

[6] Anthony John Appleby and José Heráclito Zagal. Free energy relationships in electrochemistry: a history that started in 1935. *Journal of Solid State Electrochemistry*, 15(7-8):1811–1832, 2011.

[7] Michel Armand and J-M Tarascon. Building better batteries. *Nature*, 451(7179):652–657, 2008.

[8] P. Bai, D. A. Cogswell, and Martin Z. Bazant. Suppression of phase separation in $LiFePO_4$ nanoparticles during battery discharge. *Nano Letters*, 11(11):4890–4896, 2011.

[9] Peng Bai and Martin Z Bazant. Charge transfer kinetics at the solid–solid interface in porous electrodes. *Nature Communications*, 5:3585, 2014.

[10] Robert W. Balluffi, Samuel M. Allen, and W. Craig Carter. *Kinetics of materials*. Wiley, 2005.

[11] Lubomir Banas and Robert Nürnberg. Adaptive finite element methods for cahn–hilliard equations. *Journal of Computational and Applied Mathematics*, 218(1):2–11, 2008.

[12] Paul F Barbara, Thomas J Meyer, and Mark A Ratner. Contemporary issues in electron transfer research. *The Journal of Physical Chemistry*, 100(31):13148–13168, 1996.

[13] A. J. Bard and L. R. Faulkner. *Electrochemical Methods.* J. Wiley & Sons, Inc., New York, NY, 2001.

[14] G.I. Barenblatt. *Similarity, Self-Similarity and Intermediate Asymptotics.* Cambridge University Press, 2nd edition edition, 1996.

[15] M. Z. Bazant. Theory of chemical kinetics and charge transfer based on non-equilibrium thermodynamics. *Accounts of Chemical Research*, 46:1144–1160, 2013.

[16] M. Z. Bazant, K. T. Chu, and B. J. Bayly. Current-voltage relations for electrochemical thin films. *SIAM J. Appl. Math.*, 65:1463–1484, 2005.

[17] Martin Z. Bazant. *10.626 Electrochemical Energy Systems.* MIT OpenCourseWare: Massachusetts Institute of Technology, Spring 2011. Lecture notes for subject 10.626.

[18] John M. Beggs and Dietmar Plenz. Neuronal avalanches in neocortical circuits. *J. Neurosci.*, 23(35):11167–11177, 2003.

[19] John M. Beggs and Dietmar Plenz. Neuronal avalanches are diverse and precise activity patterns that are stable for many hours in cortical slice cultures. *J. Neurosci.*, 24(22):5216–5229, 2004.

[20] I Belharouak, C Johnson, and K Amine. Synthesis and electrochemical analysis of vapor-deposited carbon-coated lifepo 4. *Electrochemistry Communications*, 7(10):983–988, 2005.

[21] Leslaw K Bieniasz. A procedure for rapid and highly accurate computation of marcus–hush–chidsey rate constants. *Journal of Electroanalytical Chemistry*, 683:112–118, 2012.

[22] P. M. Biesheuvel, M. van Soestbergen, and M. Z. Bazant. Imposed currents in galvanic cells. *Electrochimica Acta*, 54:4857–4871, 2009.

[23] M Bixon and Joshua Jortner. *Electron transferâĂŤfrom isolated molecules to biomolecules.* Wiley Online Library, 2007.

[24] J. O.'M Bockris and A. K. N. Reddy. *Modern Electrochemistry.* Plenum, New York, 1970.

[25] John O'M Bockris, Amulya KN Reddy, and Maria E Gamboa-Adelco. *Modern Electrochemistry 1, 2A, and 2B.* Springer US, 2006.

[26] A. Bonnefont, F. Argoul, and M.Z. Bazant. Analysis of diffuse-layer effects on time-dependent interfacial kinetics. *J. Electroanal. Chem.*, 500:52–61, 2001.

[27] M.S. Branicky. Stability of hybrid systems: state of the art. In *Decision and Control, 1997., Proceedings of the 36th IEEE Conference on*, volume 1, pages 120–125 vol.1, 1997.

[28] P. C. Bressloff and S. Coombes. Desynchronization, mode locking, and bursting in strongly coupled integrate-and-fire oscillators. *Physical Review Letters*, 81(10):2168–2171, September 1998.

[29] John Buck and Elisabeth Buck. Mechanism of rhythmic synchronous flashing of fireflies. *Science*, 159(3821):1319–1327, March 22 1968.

[30] Damian Burch. *Intercalation Dynamics in Lithium-Ion Batteries.* Ph.D. Thesis in Mathematics, Massachusetts Institute of Technology, 2009.

[31] Damian Burch and Martin Z. Bazant. Size-dependent spinodal and miscibility gaps for intercalation in nanoparticles. *Nano Letters*, 9(11):3795–3800, 2009.

[32] J. W. Cahn. Critical point wetting. *J. Chem. Phys.*, 66:3667–3672, 1977.

[33] J. W. Cahn and J. W. Hilliard. Free energy of a non-uniform system: I. interfacial energy. *J. Chem Phys.*, 28:258–267, 1958.

[34] John Cahn. Free energy of a nonuniform system. ii. thermodynamic basis. *Journal of Chemical Physics*, 30(5):1121–1124, 1959.

[35] John Cahn and John Hilliard. Free energy of a nonuniform system. iii. nucleation in a two-component incompressible fluid. *Journal of Chemical Physics*, 31(3):688–699, 1959.

[36] S. R. Campbell, D. L. L. Wang, and C. Jayaprakash. Synchrony and desynchrony in integrate-and-fire oscillators. *Neural Computation*, 11(7):1595–1619, October 1999.

[37] Julyan H. E. Cartwright, Victor M. Eguï£¡luz, Emilio Hernï£¡ndez-Garcï£¡a, and Oreste Piro. Dynamics of elastic excitable media. *Int. J. of Bifurcation and Chaos*, 9(11):2197–2202, 1999.

[38] Guoying Chen, Xiangyun Song, and Thomas Richardson. Electron microscopy study of the $LiFePO_4$ to $FePO_4$ phase transition. *Electrochemical and Solid State Letters*, 9(6):A295–A298, 2006.

[39] L. Q. Chen. Phase-field models for microstructural evolution. *Annual Review of Materials Research*, 32:113–140, 2002.

[40] Shengli Chen and Yuwen Liu. Electrochemistry at nanometer-sized electrodes. *Physical Chemistry Chemical Physics*, 16(2):635–652, 2014.

[41] Hung Cheng. *Advanced analytic methods in applied mathematics, science, and engineering.* Luban Pr, 2006.

[42] Christopher ED Chidsey. Free Energy and Temperature Dependence of Electron Transfer at the Metal-Electrolyte Interface. 251(4996):919–922, 1991.

[43] S. T. Chill, J. Stevenson, V. Ruehle, C. Shang, P. Xiao, D. Wales, and G. Henkelman. Benchmarks for characterization of minima, transition states and pathways in atomic systems, 2013. in preparation.

[44] SM Choo and SK Chung. Conservative nonlinear difference scheme for the cahn-hilliard equation. *Computers & Mathematics with Applications*, 36(7):31–39, 1998.

[45] K. T. Chu. A direct matrix method for computing analytical jacobians of discretized nonlinear integro-differential equations. *Journal of Computational Physics*, 228:5526–5538, 2009.

[46] William C Chueh, Farid El Gabaly, Josh D Sugar, Norman C. Bartelt, Anthony H. McDaniel, Kyle R Fenton, Kevin R. Zavadil, Tolek Tyliszczak, Wei Lai, and Kevin F. McCarty. Intercalation pathway in many-particle $LiFePO_4$ electrode revealed by nanoscale state-of-charge mapping. *Nano Letters*, 13:866 – 872, 2013.

[47] D. A. Cogswell and M. Z. Bazant. Theory of coherent nucleation in phase-separating nanoparticles. *Nano Letters*, 13:3036–3041, 2013.

[48] Daniel A. Cogswell and Martin Z. Bazant. Coherency strain and the kinetics of phase separation in $LiFePO_4$ nanoparticles. *ACS Nano*, 6:2215–2225, 2012.

[49] Luis Cueto-Felgueroso and Jaume Peraire. A time-adaptive finite volume method for the cahn-hilliard and kuramoto–sivashinsky equations. *Journal of Computational Physics*, 227(24):9985–10017, 2008.

[50] C. A. Czeisler, E. Weitzman, M. C. Moore-Ede, J. C. Zimmerman, and R. S. Knauer. Human sleep: its duration and organization depend on its circadian phase. *Science*, 210(4475):1264–1267, 1980.

[51] S. Dargaville and T. W. Farrell. The persistence of phase-separation in lifepo4 with two-dimensional li+ transport: The cahn-hilliard-reaction equation and the role of defects. *Electrochimica Acta*, 94:143–158, 2013.

[52] S. Dargaville and T.W. Farrell. Predicting active material utilization in $LiFePO_4$ electrodes using a multiscale mathematical model. *Journal of the Electrochemical Society*, 157(7):A830–A840, 2010.

[53] Steven Dargaville. *Mathematical Modelling of $LiFePO_4$ Cathodes*. Ph.D. Thesis in Mathematics, Queensland University of Technology, 2013.

[54] Steven Dargaville and Troy W Farrell. A least squares based finite volume method for the cahn-hilliard and cahn-hilliard-reaction equations. *Journal of Computational and Applied Mathematics*, 2012.

[55] Steven Dargaville and Troy W Farrell. The persistence of phase-separation in lifepo 4 with two-dimensional li+ transport: the cahn–hilliard-reaction equation and the role of defects. *Electrochimica Acta*, 94:143–158, 2013.

[56] EVL De Mello and Otton Teixeira da Silveira Filho. Numerical study of the cahn–hilliard equation in one, two and three dimensions. *Physica A: Statistical Mechanics and its Applications*, 347:429–443, 2005.

[57] Mehdi Dehghan and Davoud Mirzaei. A numerical method based on the boundary integral equation and dual reciprocity methods for one-dimensional cahn–hilliard equation. *Engineering analysis with boundary elements*, 33(4):522–528, 2009.

[58] Charles Delacourt, Philippe Poizot, Jean-Marie Tarascon, and Christian Masquelier. The existence of a temperature-driven solid solution in Li_xFePO_4 for $0 \leq x \leq 1$. *Nature materials*, 4(3):254–260, 2005.

[59] C. Delmas, M. Maccario, L. Croguennec, F. Le Cras, and F. Weill. Lithium deintercalation of $LiFePO_4$ nanoparticles via a domino-cascade model. *Nature Materials*, 7:665–671, 2008.

[60] A. Van der Ven, K. Garikipati, S. Kim, and M. Wagemaker. The role of coherency strains on phase stability in li_xfepo_4: Needle crystallites minimize coherency strain and overpotential. *J. Electrochem. Soc.*, 156:A949–A957, 2009.

[61] L. DeVille and Y. Zeng. Synchrony and periodicity in excitable neural networks with multiple subpopulations. *SIAM Journal on Applied Dynamical Systems*, 13(3):1060–1081, 2014.

[62] R. E. Lee DeVille and Charles S. Peskin. Synchrony and asynchrony in a fully stochastic neural network. *Bull. Math. Bio.*, 70(6):1608–1633, August 2008.

[63] R. E. Lee DeVille, Charles S. Peskin, and Joel H. Spencer. Dynamics of stochastic neuronal networks and the connections to random graph theory. *Mathematical Modeling of Natural Phenomena*, 5(2):26–66, 2010.

[64] Claudio V Di Leo, Elisha Rejovitzky, and Lallit Anand. A cahn–hilliard-type phase-field theory for species diffusion coupled with large elastic deformations: Application to phase-separating li-ion electrode materials. *Journal of the Mechanics and Physics of Solids*, 70:1–29, 2014.

[65] Marca M Doeff, Yaoqin Hu, Frank McLarnon, and Robert Kostecki. Effect of surface carbon structure on the electrochemical performance of lifepo4. *Electrochemical and solid-state letters*, 6(10):A207–A209, 2003.

[66] Robert Dominko, Marjan Bele, M Gaberscek, M Remskar, D Hanzel, Stane Pejovnik, and Janko Jamnik. Impact of the carbon coating thickness on the electrochemical performance of lifepo4/c composites. *Journal of the Electrochemical Society*, 152(3):A607–A610, 2005.

[67] Marc Doyle, Thomas F. Fuller, and John Newman. Modeling of galvanostatic charge and discharge of the lithium/polymer/insertion cell. *Journal of the Electrochemical Society*, 140(6):1526–1533, 1993.

[68] D. Dreyer, C. Guhlke, and R. Huth. The behavior of a many-particle electrode in a lithium-ion battery. *Physica D*, 240:1008–1019, 2011.

[69] Wolfgang Dreyer, Janko Jamnik, Clemens Guhlke, Robert Huth, Joze Moskon, and Miran Gaberscek. The thermodynamic origin of hysteresis in insertion batteries. *Nat. Mater.*, 9:448–453, 2010.

[70] W. E and X. Zhou. The gentlest ascent dynamics. *Nonlinearity*, 24(6):1831, 2011.

[71] G. Bard Ermentrout and John Rinzel. Reflected waves in an inhomogeneous excitable medium. *SIAM Journal on Applied Mathematics*, 56(4):1107–1128, 1996.

[72] Vinodkumar Etacheri, Rotem Marom, Ran Elazari, Gregory Salitra, and Doron Aurbach. Challenges in the development of advanced li-ion batteries: a review. *Energy & Environmental Science*, 4(9):3243–3262, 2011.

[73] Jeffrey W Fergus. Recent developments in cathode materials for lithium ion batteries. *Journal of Power Sources*, 195(4):939–954, 2010.

[74] T. R. Ferguson and M. Z. Bazant. Non-equilibrium thermodynamics of porous electrodes. *Journal of The Electrochemical Society*, 159:A1967–A1985, 2012.

[75] Todd R Ferguson and Martin Z Bazant. Phase transformation dynamics in porous battery electrodes. *Electrochimica Acta*, 146:89–97, 2014.

[76] HO Finklea, K Yoon, E Chamberlain, J Allen, and R Haddox. Effect of the metal on electron transfer across self-assembled monolayers. *The Journal of Physical Chemistry B*, 105(15):3088–3092, 2001.

[77] Nir Friedman, Shinya Ito, Braden A W Brinkman, Masanori Shimono, Lee DeVille, Karin A Dahmen, John M Beggs, and Thomas C Butler. Universal Critical Dynamics in High Resolution Neuronal Avalanche Data. *Physical Review Letters*, 108(20):208102, May 2012.

[78] Thomas Fuller, Marc Doyle, and John Newman. Simulation and optimization of the dual lithium ion insertion cell. *Journal of the Electrochemical Society*, 141(1):1–10, 1994.

[79] Semyon Aranovich Gershgorin. über die abgrenzung der eigenwerte einer matrix. *Bulletin de l'Académie des Sciences de l'URSS. Classe des sciences mathématiques et na*, (6):749–754, 1931.

[80] W. Gerstner and J. L. van Hemmen. Coherence and incoherence in a globally-coupled ensemble of pulse-emitting units. *Physical Review Letters*, 71(3):312–315, July 1993.

[81] L. Glass, A. L. Goldberger, M. Courtemanche, and A. Shrier. Nonlinear dynamics, chaos and complex cardiac arrhythmias. *Proc. Roy. Soc. London Ser. A*, 413(1844):9–26, 1987.

[82] John B Goodenough and Kyu-Sung Park. The li-ion rechargeable battery: a perspective. *Journal of the American Chemical Society*, 135(4):1167–1176, 2013.

[83] Ian R Gould, Dimitri Noukakis, Luis Gomez-Jahn, Ralph H Young, Joshua L Goodman, and Samir Farid. Radiative and nonradiative electron transfer in contact radical-ion pairs. *Chemical physics*, 176(2):439–456, 1993.

[84] John B Greer, Andrea L Bertozzi, and Guillermo Sapiro. Fourth order partial differential equations on general geometries. *Journal of Computational Physics*, 216(1):216–246, 2006.

[85] Michael R. Guevara and Leon Glass. Phase locking, period doubling bifurcations and chaos in a mathematical model of a periodically driven oscillator: A theory for the entrainment of biological oscillators and the generation of cardiac dysrhythmias. *Journal of Mathematical Biology*, 14(1):1–23, March 1982.

[86] JE Guyer, WJ Boettinger, JA Warren, and GB McFadden. Phase field modeling of electrochemistry. ii. kinetics. *Physical Review E*, 69(2):021604, 2004.

[87] Robert M Haddox and Harry O Finklea. Proton-coupled electron transfer of an osmium aquo complex on a self-assembled monolayer on gold. *The Journal of Physical Chemistry B*, 108(5):1694–1700, 2004.

[88] JM Hale. The potential-dependence and the upper limits of electrochemical rate constants. *Journal of Electroanalytical Chemistry and Interfacial Electrochemistry*, 19(3):315–318, 1968.

[89] B.C. Han, A. Van der Ven, D. Morgan, and G. Ceder. Electrochemical modeling of intercalation processes with phase field models. *Electrochimica Acta*, 49:4691–4699, 2004.

[90] D. Hansel and H. Sompolinsky. Synchronization and computation in a chaotic neural network. *Phys. Rev. Lett.*, 68(5):718–721, Feb 1992.

[91] Li-ping He and Yunxian Liu. A class of stable spectral methods for the cahn–hilliard equation. *Journal of Computational Physics*, 228(14):5101–5110, 2009.

[92] G. Henkelman and H. Jónsson. A dimer method for finding saddle points on high dimensional potential surfaces using only first derivatives. *J. Chem. Phys.*, 111:7010–7022, 1999.

[93] Martin C Henstridge, Eduardo Laborda, and Richard G Compton. Asymmetric marcusÃŘhush model of electron transfer kinetics: Application to the voltammetry of surface-bound redox systems. *J. Electroanal. Chem*, 674:90–96, 2012.

[94] Martin C. Henstridge, Eduardo Laborda, and Richard G. Compton. Asymmetric Marcus–Hush model of electron transfer kinetics: Application to the voltammetry of surface-bound redox systems. *Journal of Electroanalytical Chemistry*, 674:90–96, June 2012.

[95] Martin C Henstridge, Eduardo Laborda, Neil V Rees, and Richard G Compton. Marcus–Hush–Chidsey theory of electron transfer applied to voltammetry: A review. *Electrochimica Acta*, 84:12–20, 2012.

[96] Martin C Henstridge, Eduardo Laborda, Yijun Wang, Danu Suwatchara, Neil Rees, Ángela Molina, F Martínez-Ortiz, and Richard G Compton. Giving physical insight into the butler–volmer model of electrode kinetics: Application of asymmetric marcus–hush theory to the study of the electroreductions of 2-methyl-2-nitropropane, cyclooctatetraene and europium (iii) on mercury microelectrodes. *Journal of Electroanalytical Chemistry*, 672:45–52, 2012.

[97] Martin C. Henstridge, Eduardo Laborda, Yijun Wang, Danu Suwatchara, Neil Rees, Angela Molina, F. Mart inez-Ortiz, and Richard G. Compton. Giving physical insight into the butlerÃŘvolmer model of electrode kinetics: Application of asymmetric marcusÃŘhush theory to the study of the electroreductions of 2-methyl-2-nitropropane, cyclooctatetraene and europium(iii) on mercury microelectrodes. *J. Electroanal. Chem*, 672:45–52, 2012.

[98] Martin C. Henstridge, Neil V. Rees, and Richard G. Compton. A comparison of the butlerâĂŞvolmer and asymmetric marcusâĂŞhush models of electrode kinetics at the channel electrode. *Journal of Electroanalytical Chemistry*, 687(0):79 – 83, 2012.

[99] Tae Wook Heo, Long-Qing Chen, and Brandon C Wood. Phase-field modeling of diffusional phase behaviors of solid surfaces: A case study of phase-separating lixfepo 4 electrode particles. *Computational Materials Science*, 2015.

[100] A. Heyden, A. T. Bell, and F. J. Keil. Efficient methods for finding transition states in chemical reactions: Comparison of improved dimer method and partitioned rational function optimization method. *J. Chem. Phys.*, 123:224101–1–14, 2005.

[101] M. Hildebrand, M. Ipsen, A. S. Mikhailov, and G Ertl. Localized nonequilibrium nanostructures in surface chemical reactions. *New J. Phys.*, 5:61.1–61.28, 2003.

[102] M. Hildebrand, M. Kuperman, H. Wio, A. S. Mikhailov, and G. Ertl. Self-organized chemical nanoscale microreactors. *Phys. Rev. Lett.*, 83:1475–1478, 1999.

[103] R. A. Horn and C. R. Johnson. *Matrix Analysis.* Cambridge University Press, Cambridge, 1985.

[104] B. Horstmann, B. Gallant, R. Mitchell, W. G. Bessler, Y. Shao-Horn, and M. Z. Bazant. Rate-dependent morphology of li_2o_2 growth in $li–o_2$ batteries. *J. Phys. Chem. Lett.*, 4:4217–4222, 2013.

[105] H. Huang, S.C.Yin, and L.F. Nazar. Approaching theoretical capacity of $LiFePO_4$ at room temperature at high rates. *Electrochemical and Solid State Letters*, 4(10):A170–A172, 2001.

[106] N. S. Hush. Adiabatic Rate Processes at Electrodes. I. Energy-Charge Relationships. *The Journal of Chemical Physics*, 28(5):962, 1958.

[107] N. S. Hush. Electron transfer in retrospect and prospect 1: Adiabatic electrode processes. *Journal of Electroanalytical Chemistry*, 470(2):170–195, 1999.

[108] Yoon Seok Jung, Andrew S Cavanagh, Anne C Dillon, Markus D Groner, Steven M George, and Se-Hee Lee. Enhanced stability of licoo2 cathodes in lithium-ion batteries using surface modification by atomic layer deposition. *Journal of The Electrochemical Society*, 157(1):A75–A81, 2010.

[109] Byoungwoo Kang and Gerbrand Ceder. Battery materials for ultrafast charging and discharging. *Nature*, 458:190–193, 2009.

[110] Yu-Hua Kao, Ming Tang, Nonglak Meethong, Jianming Bai, W. Craig Carter, and Yet-Ming Chiang. Overpotential-dependent phase transformation pathways in lithium iron phosphate battery electrodes. *Chem. Mater.*, 22:5845–5855, 2010.

[111] Raymond Kapral and Kenneth Showalter, editors. *Chemical Waves and Patterns.* Springer, 1994.

[112] J. Kästner and P. Sherwood. Superlinearly converging dimer method for transition state search. *J. Chem. Phys.*, 128:014106–1–6, 2008.

[113] Junseok Kim, Kyungkeun Kang, and John Lowengrub. Conservative multigrid methods for cahn–hilliard fluids. *Journal of Computational Physics*, 193(2):511–543, 2004.

[114] B. W. Knight. Dynamics of encoding in a population of neurons. *Journal of General Physiology*, 59(6):734–766, 1972.

[115] J. Kuczynski and H. Wozniakowski. Estimating the largest eigenvalue by the power and lanczos algorithms with a random start. *SIAM J. Matrix Anal. A.*, 13(4):1094–1122, 1992.

[116] Y. Kuramoto. Collective synchronization of pulse-coupled oscillators and excitable units. *Physica D: Nonlinear Phenomena*, 50(1):15–30, 1991.

[117] A. M. Kuznetsov and J. Ulstrup. *Electron Transfer in Chemistry and Biology: An Introduction to the Theory.* Wiley, 1999.

[118] Eduardo Laborda, Martin C. Henstridge, Christopher Batchelor-McAuley, and Richard G. Compton. Asymmetric Marcus–Hush theory for voltammetry. *Chemical Society Reviews*, 42(12):4894, 2013.

[119] Eduardo Laborda, Martin C. Henstridge, and Richard G. Compton. Giving physical insight into the ButlerÃŘVolmer model of electrode kinetics: Part 2 ÃŘ Nonlinear solvation effects on the voltammetry of heterogeneous electron transfer processes. *J. Electroanal. Chem.*, 681:96–102, 2012.

[120] Eduardo Laborda, Danu Suwatchara, Neil V. Rees, Martin C. Henstridge, Angela Molina, and Richard G. Compton. Variable temperature study of electroreduction of 3-nitrophenolate via cyclic and square wave voltammetry: Molecular insights into electron transfer processes based on the asymmetric marcusâĂŞhush model. *Electrochimica Acta*, 110(0):772 – 779, 2013.

[121] L. Laffont, C. Delacourt, P. Gibot, M. Yue Wu, P. Kooyman, C. Masquelier, and J. Marie Tarascon. Study of the $LiFePO_4/FePO_4$ two-phase system by high-resolution electron energy loss spectroscopy. *Chem. Mater.*, 18:5520–5529, 2006.

[122] Jeffrey C. Lagarias and Yang Wang. The finiteness conjecture for the generalized spectral radius of a set of matrices. *Linear Algebra and its Applications*, 214(0):17 – 42, 1995.

[123] W. Lai and F. Ciucci. Thermodynamics and kinetics of phase transformation in intercalation battery electrodes - phenomenological modeling. *Electrochim. Acta*, 56:531–542, 2010.

[124] Wei Lai. Electrochemical modeling of single particle intercalation battery materials with different thermodynamics. *Journal of Power Sources*, 196:6534–6553, 2011.

[125] C. Lanczos. *An iteration method for the solution of the eigenvalue problem of linear differential and integral operators.* United States Governm. Press Office, 1950.

[126] J. Leng, W. Gao, C. Shang, and Z.-P. Liu. Efficient softest mode finding in transition states calculations. *J. Chem. Phys.*, 138:094110, 2013.

[127] C Li, HP Zhang, LJ Fu, H Liu, YP Wu, E Rahm, R Holze, and HQ Wu. Cathode materials modified by surface coating for lithium ion batteries. *Electrochimica Acta*, 51(19):3872–3883, 2006.

[128] D. Liberzon and A.S. Morse. Basic problems in stability and design of switched systems. *Control Systems, IEEE*, 19(5):59–70, 1999.

[129] Shengyi Liu. An analytical solution to li/li< sup>+</sup> insertion into a porous electrode. *Solid State Ionics*, 177(1):53–58, 2006.

[130] Z.-H. Liu and P.M. Hui. Collective signaling behavior in a networked-oscillator model. *Physica A: Statistical Mechanics and its Applications*, 383(2):714 – 724, 2007.

[131] Tanushree B Luke, E Barreto, and Paul So. Complete Classification of the Macroscopic Behavior of a Heterogeneous Network of Theta Neurons. *Neural computation*, 25(12):3207–3234, December 2013.

[132] R. Malek and N. Mousseau. Dynamics of Lennard-Jones clusters: A characterization of the activation-relaxation technique. *Phys. Rev. E*, 62:7723–7728, 2000.

[133] Rahul Malik, Damian Burch, Martin Bazant, and Gerbrand Ceder. Particle size dependence of the ionic diffusivity. *Nano Letters*, 10:4123–4127, 2010.

[134] R. A . Marcus. Chemical and electrochemical electron-transfer theory. *Ann. Rev. Phys. Chem.*, 15:155–196, 1964.

[135] R. A . Marcus. On the theory of electron-transfer reactions. vi. unified treatment for homogeneous and electrode reactions. *J. Chem .Phys.*, 43:679–701, 1965.

[136] R. A. Marcus. On the theory of oxidation-reduction reactions involving electron transfer. i. *J. Chem .Phys.*, 24:966–978, 1956.

[137] R. A. Marcus. Electron transfer reactions in chemistry. theory and experiment. *Rev. Mod. Phys.*, 65:599–610, 1993.

[138] R Al Marcus and Norman Sutin. Electron transfers in chemistry and biology. *Biochimica et Biophysica Acta (BBA)-Reviews on Bioenergetics*, 811(3):265–322, 1985.

[139] RA Marcus. On the theory of oxidation-reduction reactions involving electron transfer. ii. applications to data on the rates of isotopic exchange reactions. *The Journal of Chemical Physics*, 26(4):867–871, 1957.

[140] RA Marcus. On the theory of oxidation-reduction reactions involving electron transfer. iii. applications to data on the rates of organic redox reactions. *The Journal of Chemical Physics*, 26(4):872–877, 1957.

[141] RA Marcus. Chemical and electrochemical electron-transfer theory. *Annual Review of Physical Chemistry*, 15(1):155–196, 1964.

[142] Rotem Marom, S Francis Amalraj, Nicole Leifer, David Jacob, and Doron Aurbach. A review of advanced and practical lithium battery materials. *Journal of Materials Chemistry*, 21(27):9938–9954, 2011.

[143] D. V. Matyushov. Standard electrode potential, tafel equation, and the solvation thermodynamics. *J. Chem. Phys.*, 130:234704, 2009.

[144] N. Meethong, H. Y. S. Huang, S. A. Speakman, W. C. Carter, and Y. M. Chiang. Strain accommodation during phase transformations in olivine-based cathodes as a materials selection criterion for high-power rechargeable batteries. *Adv. Funct. Mater.*, 17:1115–1123, 2007.

[145] Nonglak Meethong, Hsiao-Ying Shadow Huang, W. Craig Carter, and Yet-Ming Chiang. Size-dependent lithium miscibility gap in nanoscale $li_{1-x}fepo_4$. *Electrochem. Solid-State Lett.*, 10:A134–A138, 2007.

[146] Nonglak Meethong, Yu-Hua Kao, Ming Tang, Hsiao-Ying Huang, W. Craig Carter, and Yet-Ming Chiang. Electrochemically induced phase transformation in nanoscale olivines $li_(1-x)$mpo4 (m = fe, mn). *Chem. Mater.*, 20:6189–6198, 2008.

[147] Agostino Migliore and Abraham Nitzan. Nonlinear charge transport in redox molecular junctions: a marcus perspective. *ACS Nano*, 5(8):6669–6685, 2011.

[148] Agostino Migliore and Abraham Nitzan. On the evaluation of the marcus–hush–chidsey integral. *Journal of Electroanalytical Chemistry*, 671:99–101, 2012.

[149] R. E. Mirollo and S. H. Strogatz. Synchronization of pulse-coupled biological oscillators. *SIAM J. Appl. Math.*, 50(6):1645–1662, 1990.

[150] D. Morgan, A. Van der Ven, and G. Ceder. Li conductivity in Li_xMPO_4 (m=mn,fe,co,ni) olivine materials. *Electrochemical and Solid State Letters*, 7(2):A30–A32, 2004.

[151] L. J. Munro and D. J. Wales. Defect migration in crystalline silicon. *Phys. Rev. B*, 59:3969, 1999.

[152] R. Muralidhar, T. Shaw, F. Chen, P. Oldiges, D. Edelstein, S. Cohen, R. Achanta, G. Bonilla, and M. Z. Bazant. TDDB at low voltages: An electrochemical perspective. *IEEE International Reliability Physics Symposium*, 2014.

[153] E. Bruce Nauman and D. Qiwei Heb. Nonlinear diffusion and phase separation. *Chemical Engineering Science*, 56:1999–2018, 2001.

[154] B Naundorf, T Prager, and L Schimansky-Geier. A novel approach to synchronization in coupled excitable systems. *arXiv.org*, November 2002.

[155] John Newman and Karen E. Thomas-Alyea. *Electrochemical Systems.* Prentice-Hall, Inc., Englewood Cliffs, NJ, third edition, 2004.

[156] John Newman and William Tiedemann. Porous-electrode theory with battery applications. *AIChE Journal*, 21(1):25–41, 1975.

[157] John Newman and Charles Tobias. Theoretical analysis of current distribution in porous electrodes. *Journal of The Electrochemical Society*, 109(12):1183–1191, 1962.

[158] J. Niu, A. Kushima, X. Qian, L. Qi, k. Xiang, Y.-M. Chiang, and J. Li. In situ observation of random solid solution zone in lifepo$_4$ electrode. *Nano Letters*, article ASAP, 2014.

[159] J. Nocedal. Updating quasi-Newton matrices with limited storage. *Math. Comput.*, 35:773–782, 1980.

[160] Tsutamu Ohzuku, Atsushi Ueda, and Norihiro Yamamota. Zero-strain insertion material of li[lil/3tis/3]o4 for rechargeable lithium cells. *J. Electrochem. Soc.*, 142:1431–1435, 1995.

[161] Keith B Oldham. The potential-dependence of electrochemical rate constants. *Journal of Electroanalytical Chemistry and Interfacial Electrochemistry*, 16(2):125–130, 1968.

[162] Keith B. Oldham and Jan C. Myland. On the evaluation and analysis of the Marcus–Hush–Chidsey integral. *Journal of Electroanalytical Chemistry*, 655(1):65–72, May 2011.

[163] R. A. Olsen, G. J. Kroes, G. Henkelman, A. Arnaldsson, and H. Jónsson. Comparison of methods for finding saddle points without knowledge of the final states. *J. Chem. Phys.*, 121:9776–9792, 2004.

[164] Gosuke Oyama, Yuki Yamada, Ryuichi Natsui, Shinichi Nishimura, and Atsuo Yamada. Kinetics of nucleation and growth in two-phase electrochemical reaction of $LiFePO_4$. *J. Phys. Chem. C*, 116:7306–7311, 2012.

[165] A.K. Padhi, K.S. Nanjundaswamy, and J.B. Goodenough. Phospho-olivines as positive-electrode materials for rechargeable lithium batteries. *Journal of the Electrochemical Society*, 144(4):1188–1194, 1997.

[166] Khashayar Pakdaman and Denis Mestivier. Noise induced synchronization in a neuronal oscillator. *Phys. D*, 192(1-2):123–137, 2004.

[167] V Palomares, A Goñi, I Gil de Muro, I De Meatza, M Bengoechea, I Cantero, and Teófilo Rojo. Influence of carbon content on lifepo4/c samples synthesized by freeze-drying process. *Journal of The Electrochemical Society*, 156(10):A817–A821, 2009.

[168] Kyu-Sung Park, Penghao Xiao, So-Yeon Kim, Anthony Dylla, Young-Min Choi, Graeme Henkelman, Keith J Stevenson, and John B Goodenough. Enhanced charge-transfer kinetics by anion surface modification of lifepo4. *Chemistry of Materials*, 24(16):3212–3218, 2012.

[169] C. S. Peskin. *Mathematical aspects of heart physiology.* Courant Institute of Mathematical Sciences New York University, New York, 1975. Notes based on a course given at New York University during the year 1973/74.

[170] A. Pikovsky, M. Rosenblum, and J. Kurths. *Synchronization: A Universal Concept in Nonlinear Sciences.* Cambridge University Press, 2003.

[171] Alexander Poddey and Peter E Blöchl. Dynamical dimer method for the determination of transition states with ab initio molecular dynamics. *The Journal of Chemical Physics*, 128:044107, 2008.

[172] T Prager, B Naundorf, and L Schimansky-Geier. Coupled three-state oscillators. *Physica A: Statistical Mechanics and its Applications*, 325(1-2):176–185, July 2003.

[173] T Prager and L Schimansky-Geier. Stochastic resonance in a non Markovian discrete state model for excitable systems. *arXiv.org*, October 2003.

[174] Venkatasailanathan Ramadesigan, Vijayasekaran Boovaragavan, J Carl Pirkle, and Venkat R Subramanian. Efficient reformulation of solid-phase diffusion in physics-based lithium-ion battery models. *Journal of The Electrochemical Society*, 157(7):A854–A860, 2010.

[175] N. Ravet, Y. Chouinard, J.F. Morgan, S. Besner, M. Gauthier, and M. Armand. Electroactivity of natural and synthetic triphylite. *Journal of Power Sources*, 97-98:503–507, 2001.

[176] Andrew Ritchie and Wilmont Howard. Recent developments and likely advances in lithium-ion batteries. *Journal of Power Sources*, 162(2):809–812, 2006.

[177] Y. Saad. On the rates of convergence of the lanczos and the block-lanczos methods. *SIAM J. Numer. Anal.*, 17(5):687–706, 1980.

[178] Y. Saad. *Numerical methods for large eigenvalue problems*, volume 158. SIAM, 1992.

[179] A. Samanta and W. E. Atomistic simulations of rare events using gentlest ascent dynamics. *J. Chem. Phys.*, 136:124104, 2012.

[180] W Schmickler. Current-potential curves in simple electrochemical redox reactions. *Electrochimica Acta*, 20(2):137–141, 1975.

[181] Bruno Scrosati and Jürgen Garche. Lithium batteries: Status, prospects and future. *Journal of Power Sources*, 195(9):2419–2430, 2010.

[182] Bruno Scrosati, Jusef Hassoun, and Yang-Kook Sun. Lithium-ion batteries. a look into the future. *Energy & Environmental Science*, 4(9):3287–3295, 2011.

[183] Mícheál Ó Searcóid. *Metric spaces.* Springer, 2006.

[184] K. Sekimoto. *Stochastic Energetics.* Springer, 2010.

[185] W. Senn and R. Urbanczik. Similar nonleaky integrate-and-fire neurons with instantaneous couplings always synchronize. *SIAM J. Appl. Math.*, 61(4):1143–1155 (electronic), 2000/01.

[186] W L Shew, H Yang, T Petermann, R Roy, and D Plenz. Neuronal Avalanches Imply Maximum Dynamic Range in Cortical Networks at Criticality. *Journal of Neuroscience*, 29(49):15595–15600, December 2009.

[187] Jaemin Shin, Darae Jeong, and Junseok Kim. A conservative numerical method for the cahn–hilliard equation in complex domains. *Journal of Computational Physics*, 230(19):7441–7455, 2011.

[188] Gogi Singh, Damian Burch, and Martin Z. Bazant. Intercalation dynamics in rechargeable battery materials: General theory and phase-transformation waves in $LiFePO_4$. *Electrochimica Acta*, 53:7599–7613, 2008. arXiv:0707.1858v1 [cond-mat.mtrl-sci] (2007).

[189] Kandler Smith and Chao-Yang Wang. Solid-state diffusion limitations on pulse operation of a lithium ion cell for hybrid electric vehicles. *Journal of Power Sources*, 161(1):628–639, 2006.

[190] J. Song and M. Z. Bazant. Effects of nanoparticle geometry and size distribution on diffusion impedance of battery electrodes. *J. Electrochem. Soc.*, 160:A15–A24, 2013.

[191] Venkat Srinivasan and John Newman. Discharge model for the lithium iron-phosphate electrode. *Journal of the Electrochemical Society*, 151(101):A1517–A1529, 2004.

[192] John C. Strikwerda. *Finite Difference Schemes and Partial Differential Equations.* SIAM, second edition edition, 2004.

[193] S. Strogatz. *Sync: The Emerging Science of Spontaneous Order.* Hyperion, 2003.

[194] Venkat R Subramanian, Vinten D Diwakar, and Deepak Tapriyal. Efficient macro-micro scale coupled modeling of batteries. *Journal of The Electrochemical Society*, 152(10):A2002–A2008, 2005.

[195] Norman Sutin. Theory of electron transfer reactions: insights and hindsights. *Prog. Inorg. Chem*, 30:441–498, 1983.

[196] D. Suwatchara, M. C. Henstridge, N. V. Rees, E. Laborda, and R. G. Compton. Comparative evaluation of the symmetric and asymmetric marcusÃŘhush formalisms of electrode kinetics ÃŘ the one-electron oxidation of tetraphenylethylene in dichloromethane on platinum microdisk electrodes. *J. Electroanal. Chem.*, pages 120–126, 2012.

[197] Danu Suwatchara, Martin C. Henstridge, Neil V. Rees, Eduardo Laborda, and Richard G. Compton. Comparative evaluation of the symmetric and asymmetric marcusâĂŞhush formalisms of electrode kinetics âĂŞ the one-electron oxidation of tetraphenylethylene in dichloromethane on platinum microdisk electrodes. *Journal of Electroanalytical Chemistry*, 677âĂŞ680(0):120 – 126, 2012.

[198] Danu Suwatchara, Neil V Rees, Martin C Henstridge, Eduardo Laborda, and Richard G Compton. Molecular insights into electron transfer processes via variable temperature cyclic voltammetry. application of the asymmetric marcus–hush model. *Journal of Electroanalytical Chemistry*, 685:53–62, 2012.

[199] Danu Suwatchara, Neil V. Rees, Martin C. Henstridge, Eduardo Laborda, and Richard G. Compton. Molecular insights into electron transfer processes via variable temperature cyclic voltammetry. application of the asymmetric marcusâĂŞhush model. *Journal of Electroanalytical Chemistry*, 685(0):53 – 62, 2012.

[200] Danu Suwatchara, Neil V. Rees, Martin C. Henstridge, Eduardo Laborda, and Richard G. Compton. Molecular insights into electron transfer processes via variable temperature cyclic voltammetry. Application of the asymmetric Marcus–Hush model. *J. Electroanal. Chem.*, 685:53–62, 2012.

[201] M. Tang, H.-Y. Huang, N. Meethong, Y.-H. Kao, W. C. Carter, and Y.-M. Chiang. Model for the particle size, overpotential, and strain dependence of phase transition pathways in storage electrodes: Application to nanoscale olivines. *Chem. Mater.*, 21:1557–1571, 2009.

[202] Ming Tang, James F. Belak, and Milo R. Dorr. Anisotropic phase boundary morphology in nanoscale olivine electrode particles. *The Journal of Physical Chemistry C*, 115:4922–4926, 2011.

[203] Ming Tang, W. Craig Carter, and Yet-Ming Chiang. Electrochemically driven phase transitions in insertion electrodes for lithium-ion batteries: Examples in lithium metal phosphate olivines. *Annual Review of Materials Research*, 40:501–529, 2010.

[204] J.M. Tarascon and M. Armand. Issues and challenges facing rechargeable lithium batteries. *Nature*, 414:359–367, 2001.

[205] D. Terman, N. Kopell, and A. Bose. Dynamics of two mutually coupled slow inhibitory neurons. *Phys. D*, 117(1-4):241–275, 1998.

[206] Michael M Thackeray, Christopher Wolverton, and Eric D Isaacs. Electrical energy storage for transportation: approaching the limits of, and going beyond, lithium-ion batteries. *Energy & Environmental Science*, 5(7):7854–7863, 2012.

[207] Karen Thomas, John Newman, and Robert Darling. Mathematical modeling of lithium batteries. *Advances in lithium-ion batteries*, pages 345–392, 2002.

[208] L. N. Trefethen and D. Bau III. *Numerical linear algebra.* Number 50. SIAM, 1997.

[209] M. Tsodyks, I. Mitkov, and H. Sompolinsky. Pattern of synchrony in inhomogeneous networks of oscillators with pulse interactions. *Physical Review Letters*, 71(8):1280–1283, August 1993.

[210] John J. Tyson, Christian I. Hong, C. Dennis Thron, and Bela Novak. A Simple Model of Circadian Rhythms Based on Dimerization and Proteolysis of PER and TIM. *Biophys. J.*, 77(5):2411–2417, 1999.

[211] John J. Tyson and James P. Keener. Singular perturbation theory of traveling waves in excitable media (a review). *Phys. D*, 32(3):327–361, 1988.

[212] A Van der Ven, K Garikipati, S Kim, and M Wagemaker. The role of coherency strains on phase stability in li x fepo4: Needle crystallites minimize coherency strain and overpotential. *Journal of the Electrochemical Society*, 156(11):A949–A957, 2009.

[213] Richard Van Noorden. The rechargeable revolution: A better battery. *Nature*, 507(7490):26–28, 2014.

[214] C. van Vreeswijk, L. Abbott, and G. Ermentrout. When inhibition not excitation synchronizes neural firing. *J. Comp. Neurosci.*, pages 313–322, 1994.

[215] C. van Vreeswijk and H. Sompolinsky. Chaotic balance state in a model of cortical circuits. *Neural Computation*, 10(6):1321–1372, August 15 1998.

[216] G. H. Vineyard. Frequency factors and isotope effects in solid state rate processes. *J. Chem. Phys. Solids*, 3:121–127, 1957.

[217] A. F. Voter. Hyperdynamics: Accelerated molecular dynamics of infrequent events. *Phys. Rev. Lett.*, 78:3908–3911, 1997.

[218] Marnix Wagemaker, Deepak P. Singh, Wouter J.H. Borghols, Ugo Lafont, Lucas Haverkate, Vanessa K. Peterson, and Fokko M. Mulder. Dynamic solubility limits in nanosized olivine $LiFePO_4$. *J. Am. Chem. Soc.*, 133:10222–10228, 2011.

[219] CY Wang, WB Gu, and BY Liaw. Micro-macroscopic coupled modeling of batteries and fuel cells i. model development. *Journal of The Electrochemical Society*, 145(10):3407–3417, 1998.

[220] Jiajun Wang and Xueliang Sun. Understanding and recent development of carbon coating on lifepo 4 cathode materials for lithium-ion batteries. *Energy & Environmental Science*, 5(1):5163–5185, 2012.

[221] Rainer Waser, Regina Dittmann, Georgi Staikov, and Kristof Szot. Redox-based resistive switching memories–nanoionic mechanisms, prospects, and challenges. *Advanced Materials*, 21(25-26):2632–2663, 2009.

[222] C Wert and C Zener. Interstitial atomic diffusion coefficients. *Phys. Rev.*, 76(8):1169, 1949.

[223] M Stanley Whittingham. Electrical energy storage and intercalation chemistry. *Science*, 192(4244):1126–1127, 1976.

[224] M. Stanley Whittingham. Lithium batteries and cathode materials. *Chem. Rev.*, 104:4271–4301, 2004.

[225] Arthur T. Winfree. *The geometry of biological time*, volume 12 of *Interdisciplinary Applied Mathematics*. Springer-Verlag, New York, second edition, 2001.

[226] Steven Wise, Junseok Kim, and John Lowengrub. Solving the regularized, strongly anisotropic cahn–hilliard equation by an adaptive nonlinear multigrid method. *Journal of Computational Physics*, 226(1):414–446, 2007.

[227] Olga Wodo and Baskar Ganapathysubramanian. Computationally efficient solution to the cahn–hilliard equation: Adaptive implicit time schemes, mesh sensitivity analysis and the 3d isoperimetric problem. *Journal of Computational Physics*, 230(15):6037–6060, 2011.

[228] Shao-Ling Wu, Wei Zhang, Xiangyun Song, Alpesh K Shukla, Gao Liu, Vincent Battaglia, and Venkat Srinivasan. High rate capability of li (ni1/3mn1/3co1/3) o2 electrode for li-ion batteries. *Journal of The Electrochemical Society*, 159(4):A438–A444, 2012.

[229] Xing-Long Wu, Ling-Yan Jiang, Fei-Fei Cao, Yu-Guo Guo, and Li-Jun Wan. Lifepo4 nanoparticles embedded in a nanoporous carbon matrix: Superior cathode material for electrochemical energy-storage devices. *Advanced materials*, 21(25-26):2710–2714, 2009.

[230] Yinhua Xia, Yan Xu, and Chi-Wang Shu. Local discontinuous galerkin methods for the cahn–hilliard type equations. *Journal of Computational Physics*, 227(1):472–491, 2007.

[231] Bo Xu, Danna Qian, Ziying Wang, and Ying Shirley Meng. Recent progress in cathode materials research for advanced lithium ion batteries. *Materials Science and Engineering: R: Reports*, 73(5):51–65, 2012.

[232] Atsuo Yamada, Hiroshi Koizumi, Noriyuki Sonoyama, and Ryoji Kanno. Phase change in Li_xFePO_4. *Electrochemical and Solid-State Letters*, 8(8):A409–A413, 2005.

[233] Shoufeng Yang, Yanning Song, Peter Y Zavalij, and M Stanley Whittingham. Reactivity, stability and electrochemical behavior of lithium iron phosphates. *Electrochemistry Communications*, 4(3):239–244, 2002.

[234] Zhenguo Yang, Daiwon Choi, Sebastien Kerisit, Kevin M. Rosso, DonghaiWang, Jason Zhang, Gordon Graff, and Jun Liu. Nanostructures and lithium electrochemical reactivity of lithium titanites and titanium oxides: A review. *J. Power Sources*, 192:588–598, 2009.

[235] Li-Xia Yuan, Zhao-Hui Wang, Wu-Xing Zhang, Xian-Luo Hu, Ji-Tao Chen, Yun-Hui Huang, and John B Goodenough. Development and challenges of lifepo 4 cathode material for lithium-ion batteries. *Energy & Environmental Science*, 4(2):269–284, 2011.

[236] Mats Zackrisson, Lars Avellán, and Jessica Orlenius. Life cycle assessment of lithium-ion batteries for plug-in hybrid electric vehicles–critical issues. *Journal of Cleaner Production*, 18(15):1519–1529, 2010.

[237] Y. Zeng and M. Bazant. Phase separation dynamics in isotropic ion-intercalation particles. *SIAM Journal on Applied Mathematics*, 74(4):980–1004, 2014.

[238] Y. Zeng and M. Z. Bazant. Cahn-hilliard reaction model for isotropic li-ion battery nanoparticles. *MRS Proceedings*, 1542, 2013.

[239] Yi Zeng, Paul Albertus, Reinhardt Klein, Nalin Chaturvedi, Aleksandar Kojic, Martin Z Bazant, and Jake Christensen. Efficient conservative numerical schemes for 1d nonlinear spherical diffusion equations with applications in battery modeling. *Journal of The Electrochemical Society*, 160(9):A1565–A1571, 2013.

[240] Yi Zeng, Peng Bai, Raymond Smith, and Martin Z Bazant. Simple formula for asymmetric marcus-hush kinetics. *Journal of Electroanalytical Chemistry*, 748:52 – 57, 2015.

[241] Yi Zeng, Raymond Smith, Peng Bai, and Martin Z Bazant. Simple formula for marcus-hush-chidsey kinetics. *Journal of Electroanalytical Chemistry*, 735:77 – 83, 2014.

[242] Yi Zeng, Penghao Xiao, and Graeme Henkelman. Unification of algorithms for minimum mode optimization. *The Journal of Chemical Physics*, 140(4):044115, 2014.

[243] Qi Zhang and Ralph E White. Comparison of approximate solution methods for the solid phase diffusion equation in a porous electrode model. *Journal of Power Sources*, 165(2):880–886, 2007.

[244] Shuo Zhang and Ming Wang. A nonconforming finite element method for the cahn–hilliard equation. *Journal of Computational Physics*, 229(19):7361–7372, 2010.

[245] Jianxin Zhu, Kevin Yoo, Ibrahim El-halees, and David Kisailus. Solution deposition of thin carbon coatings on lifepo4. *ACS applied materials & interfaces*, 6(23):21550–21557, 2014.